The Thesis Committee for Abhishek Bansal
Certifies that this is the approved version of the following thesis:

Improved Petrophysical Evaluation of Consolidated Calcareous Turbidite Sequences with Multi-Component Induction, NMR, Resistivity Images, and Core Measurements

APPROVED BY
SUPERVISING COMMITTEE:

Supervisor:

Carlos Torres-Verdín

Ronald J. Steel

Improved Petrophysical Evaluation of Consolidated Calcareous Turbidite Sequences with Multi-Component Induction, NMR, Resistivity Images, and Core Measurements

by

Abhishek Bansal, B.E.

Thesis

Presented to the Faculty of the Graduate School of

The University of Texas at Austin

in Partial Fulfillment

of the Requirements

for the Degree of

Master of Science in Engineering

The University of Texas at Austin

December 2012

Dedication

To my parents, Kamal and Virendra Bansal, and to my wife, Nishtha

Acknowledgements

First and foremost, I would like to express my deepest gratitude to my supervisor, Dr. Carlos Torres-Verdín, for his persistent guidance, support, and motivation throughout my research work. It was a true pleasure and honor to work with him. I am also thankful to Dr. Ronald J. Steel for being the reader of this thesis.

Furthermore, I acknowledge the support extended to me by the Petroleum and Geosystems Engineering faculty and staff, especially Reynaldo Casanova, Frankie Hart, and Roger Terzian.

I would also like to thank Elton Ferreria, Antoine Montaut, Siddharth Mishra, Zoya Heidari, Amir Frooqnia, Hyungjoo Lee, Chicheng Xu, Kanay Jerath, Olabode Ijasan, Ben Voss, Paul Sayar, Shaina Kelly, Paul Linden, and Haryanto Adiguna for their continued support during my stay at The University of Texas at Austin. I really enjoyed working with them.

A note of special gratitude goes to PEMEX Exploration and Production for providing the data used in the study, especially to MSc. Javier Méndez de León and Dr. Gabriel Camacho for their continued assistance and technical support, and for facilitating the transfer of the data to UT Austin.

The work reported in this thesis was funded by The University of Texas at Austin's Research Consortium on Formation Evaluation, jointly sponsored by Anadarko, Apache, Aramco, Baker-Hughes, BG, BHP Billiton, BP, Chevron, China Oilfield Services, Ltd., ConocoPhillips, ENI, ExxonMobil, Halliburton, Hess, Maersk, Marathon Oil Corporation, Mexican Institute for Petroleum, Nexen, ONGC, Petrobras, Repsol, RWE, Schlumberger, Shell, Statoil, Total, Weatherford, and Woodside Petroleum Limited.

Abstract

Improved Petrophysical Evaluation of Consolidated Calcareous Turbidite Sequences with Multi-Component Induction, NMR, Resistivity Images, and Core Measurements

Abhishek Bansal M.S.E.

The University of Texas at Austin, 2012

Supervisor: Carlos Torres-Verdín

We introduce a new quantitative approach to improve the petrophysical evaluation of thinly bedded sand-shale sequences that have undergone extensive diagenesis. Formations under analysis consist of carbonate-rich clastic sediments, with pore system heavily reworked by calcite and authigenic clay cementation, giving rise to rocks with high spatial heterogeneity, low porosity, and low permeability. Porosity varies from 2 to 20% and permeability varies from less than 0.001 mD to 200 mD. Diagenesis and thin laminations originate complex magnetic resonance (NMR) *T2* distributions exhibiting multimodal distributions. Furthermore, reservoir units produce highly viscous oil, which imposes additional challenges to formation evaluation.

Petrophysical evaluation of thinly bedded formations requires accurate estimation of laminar and dispersed shale concentration. We combined Thomas-Stieber's method, OBMI, and Rt-Scanner measurements to calculate laminar shale concentration. Results indicate that hydrocarbon reserves can be overestimated in the presence of high-resistivity streaks and graded beds, which give rise to electrical anisotropy. To account

for electrical anisotropy effects on petrophysical estimations, we classified reservoir rocks based on the cause of electrical anisotropy. Thereafter different interpretation methods were implemented to estimate petrophysical properties for each rock class.

We also appraised the advantages and limitations of the high-resolution method for evaluating thinly bedded formations with respect to other petrophysical interpretation methods. Numerical simulations were performed on populated earth-model properties after detecting bed boundaries from resistivity or core images. Earth-model properties were iteratively refined until field and numerically simulated logs reached an acceptable agreement. Results from the high-resolution method remained petrophysically consistent when beds were thicker than 0.25 ft.

Numerical simulations of NMR *T2* distributions were also performed to reproduce averaging effects of NMR responses in thinly bedded formations, which enabled us to improve the assessment of pore-size distributions, in-situ fluid type, and saturation. Permeability of sand units was estimated via Timur-Coates' equation by removing the effect of laminar shale on porosity and bulk irreducible volume water. Shoulder-bed corrected logs were input to the calculations.

Petrophysical properties obtained with the developed interpretation method honor all the available measurements including conventional well logs, NMR, resistivity images, multi-component induction, and core measurements. The developed interpretation method was successfully tested across four hydrocarbon-saturated intervals selected from multiple wells penetrating a deep turbidite system. Permeability values obtained with the new interpretation method improved the correlation with core measurements by 16% as compared to permeability calculations performed with conventional methods. In addition, on average the method yielded a 62% increase in hydrocarbon pore-thickness when compared to conventional petrophysical analysis.

Table of Contents

List of Tables x

\List of Figure xi

Chapter 1: Introduction 1

1.1 Background 1

1.2 Reservoir Description 5

1.3 Conventional Petrophysical Interpretation 8

1.4 Objectives 12

1.5 Outline of the Thesis 12

Chapter 2: Interpretation Methods 14

2.1 Identification of Thinly Bedded Formations 14

2.2 Calculations of Total Shale Concentration and Total Porosity 17

2.3 Quantification of Volumetric Laminar Shale Concentration 19

2.3.1 Volumetric Laminar Shale Concentration from OBMI Measurements 19

2.3.2 Volumetric Laminar Shale Concentration from Thomas-Stieber's Method 22

2.3.3 Volumetric Laminar Shale Concentration from Rt-Scanner Measurements 22

2.3.4 Comparison of Volumetric Laminar Shale Concentrations 23

2.4 Permeability Estimation 25

2.5 Shoulder-Bed Corrections of Well Logs 28

2.6 Sand Reservoir Quality 30

2.7 Numerical Simulations of NMR Measurements 32

2.7.1 Synthetic Cases 34

Chapter 3: Rock Classification and Corresponding Petrophysical Interpretation Methods 37

3.1 Laminated Beds with Isotropic Sand Units 37

3.1.1 Interpretation Method 38

3.2 Anisotropic Sands 43

3.3 High-Resistivity Streaks 45
3.3.1 High-Resolution Interpretation Method....45
3.3.2 Limitations of the High-Resolution Interpretation Method....47
Chapter 4: Field Cases 49
4.1 Quick-Look Analysis 49
4.2 Field Case No. 1: Well α 56
4.2.1 High-Resolution Interpretation Method, Well α 66
4.3 Field Case No. 2: Well β....75
4.4 Field Case No. 3: Well γ....83
4.5 Field Case No. 4: Well τ....91
4.6 Calculations of Hydrocarbon Pore-Thickness 99
4.7 Discussion....99
Chapter 5: Summary and Conclusions....101
5.1 Recommended Practices 101
5.2 Summary and Conclusions 106
5.3 Limitations 108
Appendix A: Thomas-Stieber's Method....110
A.1 Laminated Shale....110
A.2 Dispersed Shale....111
A.3 Mixed Formation....113
Nomenclature....118
Acronyms....124
References....125

List of Tables

Table 1.1: Summary of the parameters commonly used for conventional petrophysical analysis of well logs in the area of study.....9

Table 2.1: Summary of assumed petrophysical properties for the synthetic case. Figure 2.6 shows the corresponding results.....28

Table 2.2: Summary of some of the properties assumed in the numerical simulations of *T2* distributions for synthetic cases.....36

Table 4.1: Summary of well logs and core measurements available for petrophysical analysis in Wells α, β, γ, and τ.....50

Table 4.2: Summary of properties assumed for petrophysical analysis in Wells α, β, γ, and τ.....51

Table 4.3: Parameters assumed in the numerical simulation of NMR *T2* distributions at depth X172 m, Well α. Figure 4.10 shows the results obtained from numerical simulations.....74

Table 4.4: Parameters assumed in the numerical simulation of NMR *T2* distributions at depth X075 m, Well β. Figure 4.13 shows the corresponding numerical simulations.....82

Table 4.5: Parameters assumed in the numerical simulation of NMR *T2* distributions at depth X148 m, Well γ. Figure 4.17 shows the corresponding numerical simulation.....90

Table 4.6: Comparison of hydrocarbon pore-thickness (*HPT*) obtained from conventional and anisotropy analysis in different wells across the reservoir.....99

Table 5.1: Summary of wireline measurements used in the petrophysical evaluation of rock types encountered in the reservoir. 103

\

List of Figures

Figure 1.1: Classification of petrophysical beds based on bed thickness (Passey et al., 2006), corresponding well-log analysis methods, and typical vertical resolution of different wireline logs. 3

Figure 1.2: Outcrop from the studied reservoir emphasizing a stacked sequence of thinly bedded sand and shale deposits (photograph courtesy of M.Sc. Javier Méndez de León). 6

Figure 1.3: SEM image from the studied reservoir emphasizing complex topology of the pore space, together with presence of calcite and authigenic clay cementation. 7

Figure 1.4: Representative thin section of the studied reservoir, indicating poor sorting and angular grain-to-grain contact. 7

Figure 1.5: Conventional petrophysical interpretation of well logs acquired in the studied reservoir. Track 1: depth. Track 2: gamma ray. Track 3: apparent resistivity curves with different radial lengths of investigation. Track 4: horizontal resistivity and vertical resistivity. Track 5: bulk density and neutron porosity (limestone matrix) log. Track 6: NMR *T2* distributions and *T2* cutoff. Track 7: NMR total porosity and bound fluid. Track 8: total water saturation calculated with conventional petrophysical analysis and irreducible water saturation. Track 9: volumetric mineral concentration obtained with linear mineral inversion. 10

Figure 2.1: Identification of thinly bedded formations with Rt-Scanner, NMR, OBMI, and core images. Beds with thickness smaller than one foot are clearly visible on core photographs. Track 1: depth. Track 2: volumetric concentration of shale. Track 3: horizontal and vertical electrical resistivities. Track 4: NMR *T2* distributions. Track 5: OBMI image. Track 6: core photographs. 16

Figure 2.2: Comparison of volumetric concentrations of shale estimated with gamma ray and neutron-density logs. The scatter observed between the calculated shale concentrations with the two methods is attributed to the difference in vertical resolution of gamma-ray, density, and neutron logs (Figure 1.1). 18

Figure 2.3: Comparison of total porosity estimated with NMR measurements to porosity estimated with linear mineral inversion. The scatter observed between the two porosities is due to the difference in vertical resolution of NMR and bulk density logs (Figure 1.1). 19

Figure 2.4: Comparison of the volumetric laminar shale concentrations estimated with OBMI measurements and core images. OBMI measurements detected most of the lithofacies which were observed on the core photographs. OBMI measurements underestimate laminar shale concentration between the depth interval XX42 and XX44 m due to presence of beds with thickness below the vertical resolution of OBMI measurements. Track 1: depth. Track 2: core photographs and OBMI resistivity curve. Track 3: OBMI image. Track 4: volumetric laminar shale concentrations estimated with core images and OBMI measurements. 21

Figure 2.5: Comparison of volumetric laminar shale concentration estimated with different methods. Track 1: depth. Track 2: volumetric shale concentration. Track 3: vertical and horizontal electrical resistivities. Track 4: OBMI image. Track 5: NMR *T2* distributions. Track 6: volumetric laminar shale concentrations from Thomas-Stieber's method and OBMI measurements. Track 7: volumetric laminar shale concentrations from Thomas-Stieber's method and Rt-Scanner measurements. Track 8: volumetric laminar shale concentrations from Rt-Scanner and OBMI measurements. 24

Figure 2.6: Variations of permeability with volumetric laminar and dispersed shale concentration while keeping total shale concentration constant. Table 2.1 summarizes the parameters assumed for the calculations.....27

Figure 2.7: Comparison of well-log and shoulder-bed corrected permeability. On average, shoulder-bed corrected permeability exhibits 16% better agreement with core measurements (in terms of the correlation coefficient). 29

Figure 2.8: Rock classification using Leverett's Rock Quality Index (RQI) method. Representative thin sections are shown for each rock type. Rock petrophysical quality increases with an increase in both grain size and interconnected porosity and decreases with an increase in both calcite and authigenic clay cementation. 31

Figure 2.9: Clustered capillary pressure curves for each rock type (Rock Quality Index). Entry capillary pressure increases with a decrease in sand reservoir quality. 32

Figure 2.10: Flowchart describing the sequential steps adopted in this thesis to perform numerical simulations of NMR *T2* distributions. Input parameters were iteratively refined until field and numerically simulated NMR *T2* waveforms were in close agreement.....34

Figure 2.11: Sensitivity of the oil *T2* peak (green) to variations of *T2* bulk of oil; the *T2* peak of oil moves toward right with a decrease in oil viscosity. .35

Figure 2.12: Sensitivity of water and oil *T2* peaks to changes of fluid concentration; Sw_{irr} is irreducible water saturation, Sw_f is mobile water saturation, and *So* is oil saturation.....36

Figure 3.1: Description of rocks comprising alternating thin beds of isotropic sand and isotropic/anisotropic shale layers; R_{sh} is shale resistivity, R_h is horizontal resistivity, R_v is vertical resistivity, and R_{sd} is sand resistivity. 38

Figure 3.2: Workflow adopted in this study for the petrophysical evaluation of rocks composed of isotropic sands interbedded between isotropic/anisotropic shale layers. Input parameters are iteratively refined until obtaining petrophysically consistent properties. $C_{sh\text{-}lam}$: volumetric laminar shale concentration; $C_{sh\text{-}disp}$: dispersed shale concentration in the sand unit; Sw_t: total water saturation; ϕ_{sd}: sand porosity; R_{sd}: sand resistivity; Sw_{sd}: sand water saturation; *HPT*: Hydrocarbon pore-thickness; T-S: Thomas-Stieber's method (Thomas and Stieber, 1975).....39

Figure 3.3: Description of anisotropic sand and corresponding electrical resistivity profile. Electrical anisotropy originates from alternating beds of fine and coarse grains; R_{fg} is resistivity of fine grain, R_h is horizontal resistivity, R_v is vertical resistivity, and R_{cg} is resistivity of coarse grain.....43

Figure 3.4: Description of a rock with thin high-resistivity streaks. Electrical anisotropy is generated due to alternating beds of low-porosity, high-resistivity streaks and sand layers; R_{st} is resistivity of low-porosity, high-resistivity streaks, R_h is horizontal resistivity, R_v is vertical resistivity, and R_{sd} is sand resistivity. 45

Figure 3.5: Flowchart describing the high-resolution method for petrophysical evaluation of thinly bedded formations. This method yields detailed petrophysical properties for each individual bed. Petrophysical properties obtained are validated with core measurements and NMR numerical simulations. 47

Figure 4.1: Comparison of Thomas-Stieber's crossplots constructed for different depositional sequences encountered in different wells within the studied reservoir. These crossplots indicate that formations under study are affected by calcite and/or authigenic clay cementation. 53

Figure 4.2: Comparison of Klein's plot (Minh et al., 2007) for different wells within the studied reservoir. All data points lie in the upper wing of the butterfly chart, thereby indicating that horizontal resistivity is higher than shale-base resistivity. This behavior further suggests absence of fully water-bearing formations. 55

Figure 4.3: Core photographs acquired in the depth intervals X137.8-X138.8 m and X143.3-X144.3 m, Well α. (a) Core photographs evidencing a thinly bedded sand-shale sequence. Bed thickness ranges from a few inches to a few feet. (b) Core photographs evidencing heterogeneous formation with bed thickness smaller than one foot. 59

Figure 4.4: Comparison of horizontal, vertical, and OBMI resistivities. Track 1: depth. Track 2: volumetric shale concentration and formation dip. Track 3: OBMI image. Track 4: horizontal resistivity, vertical resistivity, and OBMI R_{xo} curve. Track 5: NMR *T2* distributions and *T2* cutoff. 60

Figure 4.5: Results obtained from anisotropy analysis in Well α. Track 1: depth. Track 2: volumetric shale concentration and formation dip. Track 3: OBMI image. Track 4: bulk density and neutron (limestone matrix) log. Track 5: sand, horizontal, and vertical resistivity. Track 6: NMR *T2* distributions. Track 7: NMR total porosity and bound fluid. Track 8: volumetric laminar shale concentrations from Rt-Scanner measurements and Thomas-Stieber's method. Track 9: volumetric dispersed shale concentration in sand units and volumetric shale concentration estimated from core measurements. Track 10: shoulder-bed corrected sand porosity, sand irreducible bulk volume, and core porosity. Track 11: sand and core permeability. Track 12: sand reservoir quality. 62

Figure 4.6: Results obtained from anisotropy analysis in Well α. Track 1: depth. Track 2: volumetric shale concentration and formation dip. Track 3: apparent resistivity curves with different radial lengths of investigation. Track 4: bulk density and neutron (limestone matrix) log. Track 5: sand, horizontal, and vertical resistivity. Track 6: NMR *T2* distributions. Track 7: NMR total porosity and bound-fluid. Track 8: total water saturation calculated with conventional petrophysical analysis and irreducible water saturation. Track 9: total water saturation calculated with anisotropy analysis and irreducible water saturation. Track 10: non-shale water saturation calculated with anisotropy analysis and conventional petrophysical analysis. 64

Figure 4.7**:** Thomas-Stieber total shale concentration versus total porosity crossplot, emphasizing the distribution of (a) total water saturation, (b) hydrocarbon pore thickness, (c) permeability, and (d) sand reservoir quality index (RQI), in Well α, depth interval X070-X175 m. 65

Figure 4.8: Results obtained with the high-resolution interpretation method for the petrophysical evaluation of thinly bedded formations. Dashed curves identify numerically simulated logs while solid curves indicate field logs. Track 1: depth. Track 2: numerically simulated gamma-ray, field gamma-ray, shoulder-bed corrected shale concentration, and volumetric dispersed shale concentration. Track 3: deep resistivity, numerically simulated deep resistivity, and true bed resistivity. Track 4: numerically simulated density log, field bulk density log, core porosity, field neutron (limestone matrix) porosity log, shoulder-bed corrected porosity, and numerically simulated neutron (limestone matrix) porosity log. Track 5: vertical, horizontal, sand, and true bed resistivity. Track 6: true bed resistivity and OBMI R_{xo} curve. Track 7: core image and OBMI R_{xo} curve. Track 8: NMR *T2* distributions. Track 9: shoulder-bed corrected water saturation. 70

Figure 4.9: Results obtained with the high-resolution interpretation method for the petrophysical evaluation of thinly bedded formations. Dashed curves identify numerically simulated logs while solid curves indicate field logs. Track 1: depth. Track 2: numerically simulated gamma-ray, field gamma-ray, shoulder-bed corrected shale concentration, and volumetric dispersed shale concentration. Track 3: deep resistivity, numerically simulated deep resistivity, and true bed resistivity. Track 4: numerically simulated density log, field bulk density log, core porosity, field neutron (limestone matrix) porosity log, shoulder-bed corrected porosity, and numerically simulated neutron (limestone matrix) porosity log. Track 5: vertical, horizontal, sand, and true bed resistivity. Track 6: NMR *T2* distributions. Track 7: water saturation estimated with conventional petrophysical analysis and the high-resolution interpretation method. Track 8: water saturation estimated with conventional petrophysical analysis and electrical anisotropy analysis. Track 9: water saturation estimated with the high-resolution interpretation method and electrical anisotropy analysis. 72

Figure 4.10: Results obtained from the numerical simulations of NMR *T2* distributions at depth X172 m, Well α. An excellent agreement is achieved between field and numerically simulated *T2* distributions. Table 4.3 describes the parameters assumed in the simulations. 74

Figure 4.11: Results obtained from anisotropy analysis in Well β. Track 1: depth. Track 2: volumetric shale concentration and formation dip. Track 3: apparent resistivity curves with different radial lengths of investigation. Track 4: bulk density and neutron (limestone matrix) log. Track 5: sand, horizontal, and vertical resistivity. Track 6: NMR *T2* distributions. Track 7: NMR total porosity and bound fluid. Track 8: volumetric laminar shale concentrations estimated with Rt-Scanner measurements and Thomas-Stieber's method. Track 9: volumetric dispersed shale concentration in the sand layers. Track 10: shoulder-bed corrected sand porosity, sand irreducible bulk volume, and core porosity. Track 11: sand and core permeability. Track 12: sand reservoir quality. 78

Figure 4.12: Results obtained from anisotropy analysis in Well β. Track 1: depth. Track 2: volumetric shale concentration and formation dip. Track 3: apparent resistivity curves with different radial lengths of investigation. Track 4: bulk density and neutron (limestone matrix) log. Track 5: sand, horizontal, and vertical resistivity. Track 6: NMR *T2* distributions. Track 7: NMR total porosity and bound fluid. Track 8: total water saturation from conventional petrophysical analysis and irreducible water saturation. Track 9: total water saturation from anisotropy analysis and irreducible water saturation. Track 10: non-shale water saturation from anisotropy analysis and conventional petrophysical analysis. 80

Figure 4.13: Results obtained from numerical simulations of NMR *T2* distributions at depth X075 m, Well β. An excellent agreement is achieved between field and numerically simulated *T2* distributions; NMR numerical simulations indicate good sand reservoir units interbedded between shale layers. Table 4.4 summarizes the parameters assumed in the simulations. 82

Figure 4.14: Idealized depositional units (Bouma sequence) of a classic turbidite sequence (Mollison et al., 2001). 83

Figure 4.15: Results obtained from the anisotropy analysis in Well γ. Track 1: depth. Track 2: volumetric shale concentration and formation dip. Track 3: apparent resistivity curves with different radial lengths of investigation. Track 4: bulk density and neutron (limestone matrix) log. Track 5: sand, horizontal, and vertical resistivity. Track 6: NMR *T2* distributions. Track 7: NMR total porosity and bound fluid. Track 8: volumetric laminar shale concentrations estimated with Rt-Scanner measurements and Thomas-Stieber's method. Track 9: volumetric dispersed shale concentration in the sand layers. Track 10: shoulder-bed corrected sand porosity and sand irreducible bulk volume. Track 11: sand permeability. Track 12: sand reservoir quality. 87

Figure 4.16: Results obtained from the anisotropy analysis in Well γ. Track 1: depth. Track 2: volumetric shale concentration and formation dip. Track 3: apparent resistivity curves with different radial lengths of investigation. Track 4: bulk density and neutron (limestone matrix) log. Track 5: sand, horizontal, and vertical resistivity. Track 6: NMR *T2* distributions. Track 7: NMR total porosity and bound fluid. Track 8: total water saturation estimated with conventional petrophysical analysis and anisotropy analysis assuming isotropic sands. Track 9: total water saturation estimated with conventional petrophysical analysis and anisotropy analysis assuming anisotropic sands. Track 10: total water saturation estimated with anisotropy analysis assuming isotropic and anisotropic sands.....89

Figure 4.17: Results obtained from numerical simulations of NMR *T2* distribution at depth X148 m, Well γ. An excellent agreement is obtained between field and numerically simulated *T2* distribution. Table 4.5 summarizes the parameters assumed in the numerical simulations.....90

Figure 4.18: Core photographs from the depth interval X212-X213 m, in Well τ, indicating absence of laminar shale concentration. 93

Figure 4.19: Core photographs from the depth interval X122.7-X123.7 m, Well τ, indicating presence of ripples and bioturbated formations. 94

Figure 4.20: Results obtained from anisotropy analysis in Well τ. Track 1: depth. Track 2: volumetric shale concentration and formation dip. Track 3: apparent resistivity curves with different radial lengths of investigation. Track 4: bulk density and neutron (limestone matrix) log. Track 5: sand, horizontal, and vertical resistivity. Track 6: NMR *T2* distributions. Track 7: NMR total porosity and bound fluid. Track 8: volumetric laminar shale concentrations estimated with Rt-Scanner measurements and Thomas-Stieber's method. Track 9: volumetric dispersed shale concentration in the sand layers. Track 10: shoulder-bed corrected sand porosity, sand irreducible bulk volume, and core porosity. Track 11: sand and core permeability. Track 12: sand reservoir quality. 96

Figure 4.21: Results obtained from anisotropy analysis in Well τ. Track 1: depth. Track 2: volumetric shale concentration and formation dip. Track 3: OBMI image. Track 4: bulk density and neutron (limestone matrix) log. Track 5: sand, horizontal, and vertical resistivity. Track 6: NMR *T2* distributions. Track 7: NMR total porosity and bound fluid. Track 8: total water saturation from conventional petrophysical analysis and irreducible water saturation. Track 9: total water saturation from anisotropy analysis and irreducible water saturation. Track 10: non-shale water saturation from anisotropy analysis and conventional petrophysical analysis. Track 11: results obtained from linear mineral inversion.....98

Figure 5.1: Interpretation algorithm describing our recommended best practices for petrophysical evaluation of thinly bedded rock formations.....105

Figure 5.2: Distribution of hydrocarbon pore-thickness (*HPT*) with increasing laminar shale concentration in the four wells considered in this thesis. 108

Figure A.1: Description of laminated shaly-sand model. This model comprises an alternating sequence of pure sand and pure shale layers. Shale is not present in the pore space of sand layers. 110

Figure A.2: Description of dispersed shaly-sand model. In this system, shale is present only in the pore space of the rock. 111

Figure A.3: Graphical representation of the Thomas-Stieber model exhibiting locus of laminar and dispersed shale concentrations. 113

Figure A.4: Description of laminated with dispersed shale model. Shale is present in layers as well as in the pore space of sand units. 113

Figure A.5: Thomas-Stieber crossplot exhibiting graphical representation of laminar shale concentration, dispersed shale concentration, and sand porosity calculations. 117

Chapter 1: Introduction

Thinly bedded formations are known to comprise large hydrocarbon reserves worldwide, but their exploitation remains challenging. Most of the complications arising in the petrophysical interpretation of thinly bedded formations are due to intermixing of adjacent bed responses on borehole measurements. This phenomenon is often referred to as shoulder-bed effect on well logs.

1.1 BACKGROUND

Due to shoulder-bed effects on well logs, horizontal resistivity can be biased toward lower values than actual sand resistivity in thinly bedded, hydrocarbon-bearing sand-shale sequences. This behavior is attributed to the relatively high electrical conductivity of laminar shale. Several interpretation models have been proposed to compensate for the effect of shale concentration on horizontal resistivity, but the majority of the published studies have focused on dispersed shaly-sand models (dual-water, Waxman-Smits, etc.) Dispersed shaly-sand models fail to account for the high electrical conductivity effect of laminar shale, which results in an underestimation of hydrocarbon reserves. To circumvent this problem, Poupon et al. (1954) proposed a parallel-circuit relationship between sand and shale conductivities. Their interpretation model invokes alternating beds of sand and shale layers in which beds are considered parallel to each other and perpendicular to the borehole. The equation proposed was

$$\sigma_t = \sigma_{sh} C_{sh} + \sigma_{sd} (1 - C_{sh}), \tag{1.1}$$

where σ_t is measured electrical conductivity, σ_{sh} is shale electrical conductivity, C_{sh} is volumetric concentration of shale, and σ_{sd} is sand electrical conductivity. Equation (1.1)

is used to calculate sand electrical conductivity, which is thereafter used to estimate hydrocarbon saturation in sand layers. However, equation (1.1) does not take into account the effects of relative formation dip on horizontal electrical conductivity, which limits the applicability of the interpretation method.

Shoulder-bed effects are prominent when beds are thinner than the vertical resolution of the measurements involved in the calculations. Figure 1.1 shows the typical vertical resolution of different wireline measurements together with the bed classification system suggested by Passey et al. (2006). Beds were classified petrophysically into three categories: thick beds, thin beds, and very thin beds or laminations. The choice of bed thickness cutoffs was based on the ability of wireline measurements to resolve true bed petrophysical properties. For thin beds, 2 ft was selected as a cutoff because that is the vertical resolution of resistivity measurements. Similarly, for very thin beds or laminations, 1 inch was selected as a cutoff because that is the vertical resolution of core plugs and resistivity images.

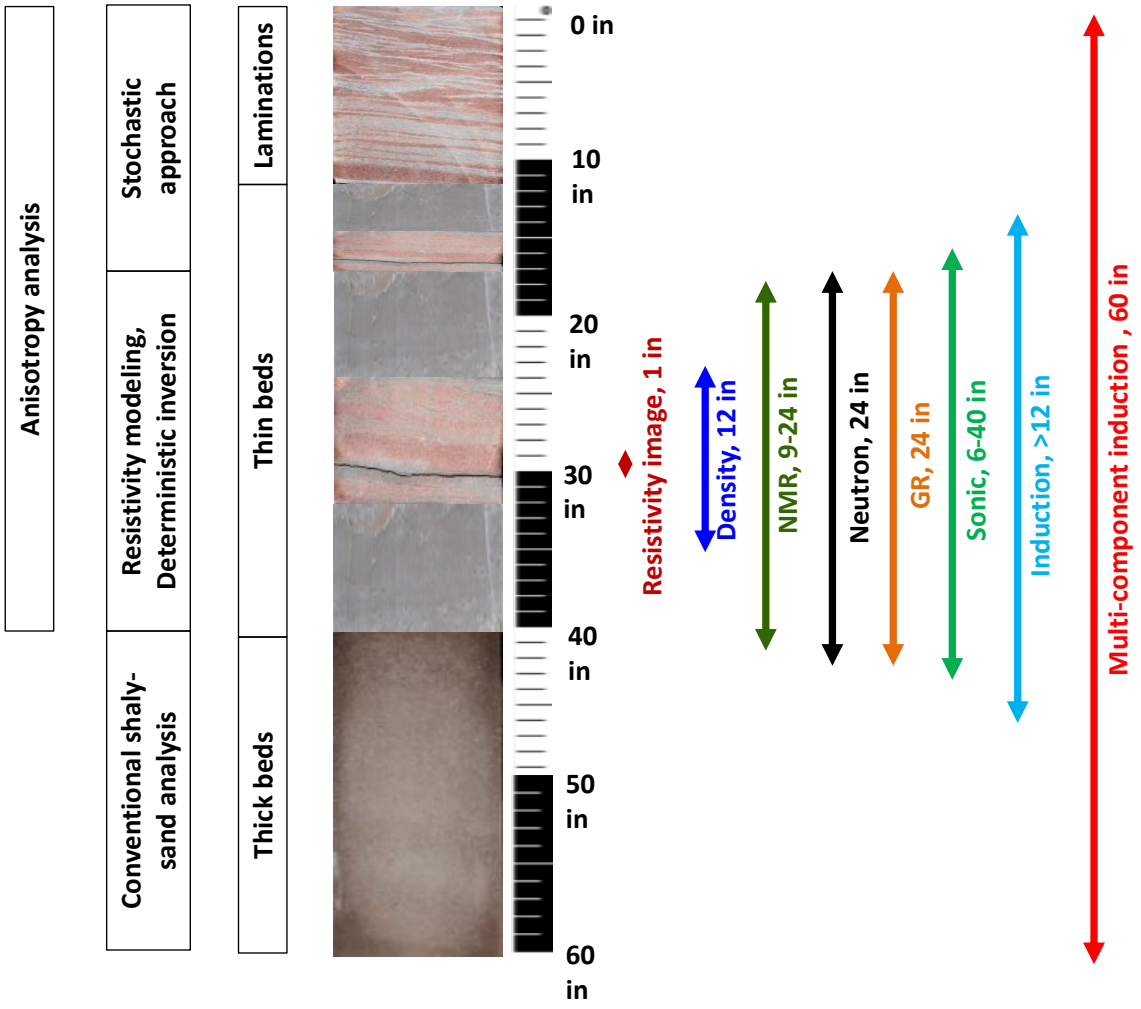

Figure 1.1: Classification of petrophysical beds based on bed thickness (Passey et al., 2006), corresponding well-log analysis methods, and typical vertical resolution of different wireline logs.

For thick beds, conventional petrophysical interpretation of well logs yields reliable results because the vertical resolution of wireline measurements is shorter than petrophysical bed thickness. However, for thin beds and laminations, conventional petrophysical interpretation yields inconsistent results because of shoulder-bed effects.

In rock formations with thin beds thicker than 0.7 ft, deterministic inversion yields consistent results by taking shoulder-bed effects into account in the inversion. However, when beds are thinner than 0.7 ft, the petrophysical model is insufficiently constrained and thus non-uniqueness limits the ability of deterministic inversion to deliver petrophysically consistent properties (Sánchez-Ramirez et al., 2009).

Stochastic inversion yields petrophysically consistent properties in rock formations comprising thin beds and laminations. The method outputs global statistical petrophysical properties instead of detailed values for individual beds (Passey et al., 2006).

Electrical anisotropy analysis is based on the tensor resistivity model proposed by Klein et al. (1995, 1997) and Hagiwara (1997). In this model, the formation is represented by a stacked sequence of sand and shale layers. The method attempts to remove the effects of laminar shale on porosity and resistivity. Sand porosity is obtained from Thomas-Stieber's method (Thomas and Stieber, 1975) whereas sand resistivity is derived from the tensor resistivity model. Dispersed shaly-sand equations, such as dual-water or Waxman-Smits, are then implemented to estimate water saturation in sand units (Fanini et al., 2001; Mollison et al., 2001).

In this thesis, I document the application of an integrated interpretation approach for petrophysical evaluation of thinly bedded and highly heterogeneous rock formations. This approach makes use of advanced wireline measurements such as NMR, multi-component induction, resistivity images, and core measurements. In the following section, I introduce the geological and petrophysical background of the studied reservoir. Additionally, I discuss the problems associated with conventional petrophysical methods of well-log interpretation.

1.2 RESERVOIR DESCRIPTION

Formations under study originate from a system of submarine fan and turbidite sediments from Paleocene to Eocene age. Starting from the Paleocene through the Eocene, these formations were actively reworked by uplifting, thrusting, and subsidence. Overturned folds and reverse faults are also observed in the formations. Rocks consist of thinly bedded sand-shale sequences, in which bed thickness ranges from less than an inch to a few feet. Figure 1.2 shows an outcrop from the studied reservoir, emphasizing the presence of thinly bedded sand-shale sequences. Rocks have been subject to extensive diagenesis that caused the development of complex pore structure as is evident from SEM thin sections and NMR *T2* distributions. Calcite, dolomite, and authigenic clay cementation drastically decreased the initial values of porosity and permeability. Predominant porosity ranges from 2 to 15%, while permeability ranges from less than 0.001 mD to 200 mD.

Petrographical analysis of the formation under study indicates a complex mineralogy composed of quartz and calcite as dominant minerals (60-80 wt%). Other minerals include dolomite (0-15 wt%), feldspar (4-5 wt%), ankerite (0-2 wt%), and pyrite (0-0.5 wt%). Petrographical analysis also indicates that the shale fraction mainly consists of laminar and dispersed shale with a negligible amount of structural shale. Presence of pore-filling kaolinite, smectite, and mixed-layer illite-smectite occludes the inter-granular porosity (Figure 1.3). In addition, chlorite-smectite was observed as pore-lining cement. Secondary porosity was developed due to partial dissolution of calcite cementation. The formation is a carbonate-rich, clastic sandstone, and is texturally and compositionally immature, which is evident from the interstitial clay matrix, poor sorting, and angular grain-to-grain contact (Figure 1.4). Formations under study comprise high-viscosity oil.

Several publications have documented the geological background of the studied reservoir, including Méndez de León and Sanguinetti (2006), and Estrada et al. (2010).

Figure 1.2: Outcrop from the studied reservoir emphasizing a stacked sequence of thinly bedded sand and shale deposits (photograph courtesy of M.Sc. Javier Méndez de León).

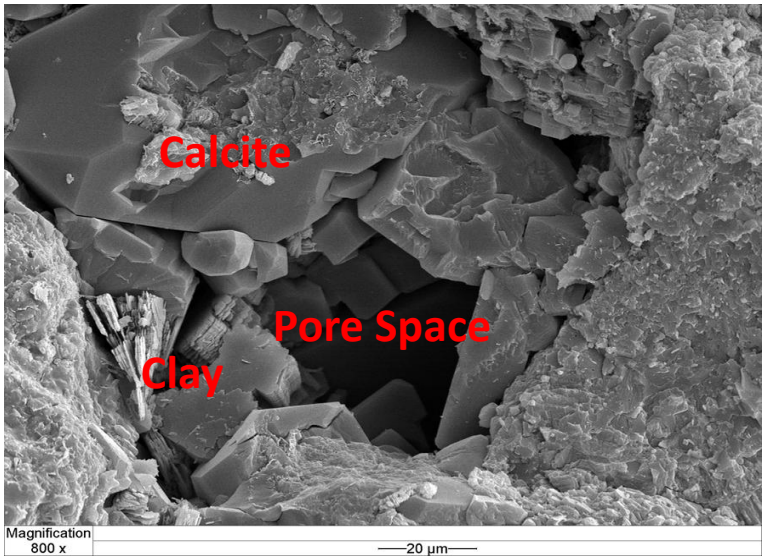

Figure 1.3: SEM image from the studied reservoir emphasizing complex topology of the pore space, together with presence of calcite and authigenic clay cementation.

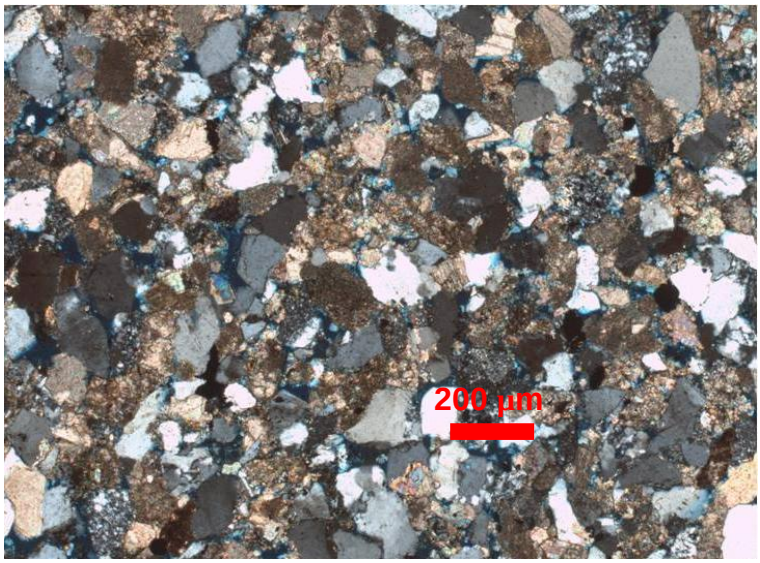

Figure 1.4: Representative thin section of the studied reservoir, indicating poor sorting and angular grain-to-grain contact.

The studied reservoir covers an area of over 3,300 km^2 and is estimated to contain 100 billion barrels of oil and 40 trillion cubic feet of gas-in-place. However, only 140 millions barrels of oil equivalent have been historically produced. Moreover, the recovery factor of the studied reservoir is very low and most wells are fracture-stimulated to increase flow rate to economic levels (Cheatwood and Guzmán, 2002).

1.3 CONVENTIONAL PETROPHYSICAL INTERPRETATION

Figure 1.5 shows the well-logs acquired in one of the wells within the studied reservoir. This well was drilled vertically with oil-base mud (OBM). Apparent resistivity curves with different radial lengths of investigation stack over each other, indicating absence of mobile water pore volume; NMR measurements exhibit bimodal distributions, with a majority of *T2* peaks lower than 33 ms, indicating presence of microporosity.

Figure 1.5, track 8 compares total water saturation calculated with conventional petrophysical analysis to irreducible water saturation. Irreducible water saturation was estimated with NMR measurements by applying a constant *T2* cutoff. In clean sands, conventional petrophysical interpretation of well logs yields water saturation that is in close agreement with irreducible water saturation. However, in shaly-sands, conventional petrophysical analysis yields water saturation values higher than irreducible water saturation, thereby indicating presence of mobile water pore volume, which is in contradiction with production data for this well. Production data indicate negligible water efflux, which confirms absence of any significant mobile water pore volume. Moreover, petrophysical properties obtained with conventional well log analysis and numerical simulations of NMR *T2* distributions are inconsistent with each other. This anomalous petrophysical interpretation of well logs is attributed to the effect of high electrical conductivity of shale laminations on apparent resistivity measurements, which

conventional petrophysical analysis does not account for. At the time of this study, core laboratory water saturation measurements were not available to verify the water saturation calculated with conventional well log analysis. Table 1.1 summarizes some of the parameters used in conventional petrophysical analysis of well logs.

Variable	Value	Units
Archie's Winsauer factor, a	1	[-]
Archie's porosity exponent, m	2.1	[-]
Archie's saturation exponent, n	2	[-]
Formation water salinity	35,000	[ppm NaCl]
Shale porosity, ϕ_{sh}	0.12	[Fraction]

Table 1.1: Summary of the parameters commonly used for conventional petrophysical analysis of well logs in the area of study.

Herrick and Kennedy (1996) reported that thinly bedded rocks are non-Archie's rocks and that conventional shaly-sand analysis (dispersed shale-sand models) tends to overestimate water saturation in such formations. They suggested decreasing Archie's saturation exponent, n, to account for the high electrical conductivity effect of thin laminations on apparent resistivity measurements. In this study, we explore alternative methods for petrophysical evaluation of thinly bedded sand-shale sequences that quantitatively address the volume of investigation of the measurements included in the evaluation.

Figure 1.5, track 9 shows minerals and their volumetric concentrations estimated with linear mineral inversion, indicating presence of a relatively large volume of calcite

in the formation. Results derived from linear mineral inversion are consistent with XRD measurements.

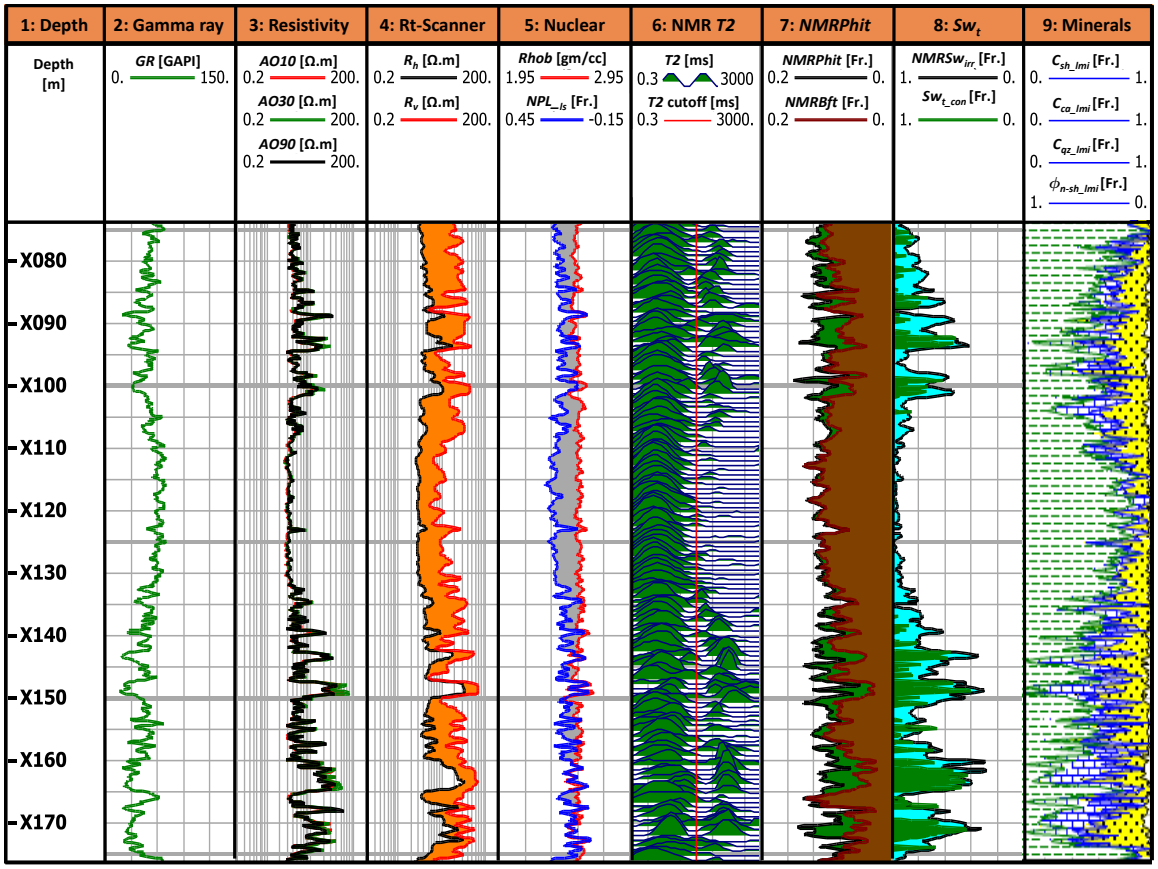

Figure 1.5: Conventional petrophysical interpretation of well logs acquired in the studied reservoir. Track 1: depth. Track 2: gamma ray. Track 3: apparent resistivity curves with different radial lengths of investigation. Track 4: horizontal resistivity and vertical resistivity. Track 5: bulk density and neutron porosity (limestone matrix) log. Track 6: NMR *T2* distributions and *T2* cutoff. Track 7: NMR total porosity and bound fluid. Track 8: total water saturation calculated with conventional petrophysical analysis and irreducible water saturation. Track 9: volumetric mineral concentration obtained with linear mineral inversion.

Conventional interpretation methods tend to underestimate permeability in thinly bedded sand-shale sequences. Through well logs, permeability is often estimated using empirical equations, such as Timur-Coates (Coates et al., 1991), Timur-Tixier (Timur, 1969), etc., which enforce relationships among permeability, porosity, and irreducible water saturation, with the underlying assumption that irreducible water saturation correlates with grain-size distribution. For example, rocks with smaller predominant grain size will exhibit higher irreducible water saturation and lower permeability. However, due to shoulder-bed effects on borehole measurements acquired in thinly bedded formations, well logs cannot resolve true bed petrophysical properties, such as porosity, shale concentration, etc., which can lead to erroneous estimation of permeability.

Additionally, in conventional well log analysis, net-to-gross, *N/G*, calculations are performed by enforcing a cutoff to well logs or their associated properties, such as shale concentration, porosity, and/or water saturation. This approach yields consistent results in thick sands because well logs resolve true bed petrophysical properties. However, in thin beds and laminations, well logs respond to average properties across adjacent beds, thereby leading to erroneous estimates of *N/G*. In turn, errors in *N/G* calculations lead to incorrect estimates of hydrocarbon-in-place.

Formations under study have been subject to extensive diagenesis. Thin laminations and diagenesis have caused the development of highly heterogeneous formations. Several authors, such as Clavaud et al. (2005) and Rabinovich et al. (2007), emphasize that electrical anisotropy analysis yields consistent petrophysical properties in thinly bedded sand-shale sequences. This behavior prompted us to perform electrical anisotropy analysis for petrophysical evaluation of thinly bedded and highly heterogeneous formations. However, electrical anisotropy measured with multi-component induction measurements could be simultaneously affected by several factors,

such as presence of laminar shale, high-resistivity streaks, anisotropic sands, etc. No single interpretation method provides petrophysically consistent results across all the rock types encountered in the studied reservoir. Rock classification is required to take all these factors into account. Different petrophysical interpretation methods are then implemented for each rock class.

1.4 OBJECTIVES

The primary objective of this thesis is to develop a consistent petrophysical workflow to estimate porosity, permeability, and hydrocarbon reserves in thinly bedded formations using advanced wireline measurements such as NMR, resistivity images, multi-component induction, and core measurements. This study also explores different interpretation methods to diagnose rock types encountered in the studied reservoir. Additionally, the study considers the estimation of pore-size distributions and in-situ fluid properties by performing numerical simulations of NMR *T2* distributions.

I applied the developed interpretation method to four unique field cases of thinly bedded sand-shale sequences. Based on these field cases, I make recommendations for improved petrophysical evaluation of the various rock types encountered in the studied reservoir.

1.5 OUTLINE OF THE THESIS

Chapter 2 describes the methods used to identify thinly bedded formations. It also documents the approach used to calculate porosity, laminar shale concentration, and permeability. Further, it describes the method adopted to perform numerical simulations of NMR *T2* distributions. Chapter 3 discusses the method used in the study to perform

rock classification. Subsequently, in Chapter 4, I report the results obtained when applying the developed workflow to four field cases. Finally, Chapter 5 summarizes the recommended best practices and conclusions stemming from the study.

Chapter 2: Interpretation Methods

This chapter describes the approach used to identify thinly bedded rock formations. It also discusses methods used to estimate volumetric shale concentration, volumetric laminar shale concentration, porosity, permeability, and sand reservoir quality. Finally, it describes the algorithm adopted in the study to perform shoulder-bed corrections and numerical simulations of NMR *T2* distributions.

2.1 Identification of Thinly Bedded Formations

In conventional petrophysical interpretation of well logs, apparent resistivity curves (AIT[1]) are the primary basis for identification of hydrocarbon-bearing formations due to the difference in electrical resistivity between hydrocarbon- and water-bearing zones. However, in thinly bedded formations where bed thickness is shorter than the vertical resolution of resistivity measurements, the response of highly resistive oil-bearing zones can be masked between low resistive shale layers, which resistivity measurements are not able to resolve. This phenomenon restricts the identification of thinly bedded, hydrocarbon-bearing formations with resistivity measurements alone. Advanced wireline measurements, such as multi-component induction, resistivity images, NMR, and core images can facilitate the identification of thin beds (Passey et al., 2006).

For identification of thinly bedded formations, core images serve as ground truth. In addition, digital processing of core images provides an effective means to estimate volumetric sand concentration. Resistivity images are only second to core images in their ability to diagnose thin beds. Resistivity images, with their high vertical resolution

[1] Mark of Schlumberger

(Figure 1.1), measure variations in electrical resistivity of sand and shale sequences, thereby allowing the identification of thin beds.

Multi-component induction measurements are also capable of recognizing thin beds or laminations. Horizontal resistivity is biased toward values lower than actual sand resistivity due to the relatively high electrical conductivity of laminar shale. By contrast, vertical resistivity is affected by hydrocarbon present in sand layers, which results in larger values than those of horizontal resistivity. This phenomenon causes a difference between horizontal and vertical resistivities which facilitates the diagnosis and approval of thinly bedded hydrocarbon-bearing formations.

In addition, NMR measurements provide strong evidence of thin beds when exhibiting bimodal *T2* distributions. In thinly bedded formations, NMR measurements produce an average response of adjacent beds due to their relatively large volume of investigation (Figure 1.1). NMR measurements exhibit smaller *T2* values for bound water present in shale beds and larger *T2* values for the mobile pore volume present in sand units. This property facilitates the identification of thinly bedded formations.

Figure 2.1 shows the well logs used in this study to identify thin beds. Core photographs and resistivity images clearly diagnose presence of beds with thickness lower than one foot. At the same depth interval, Rt-Scanner[2] measurements show a significant separation between horizontal and vertical resistivities, whereas NMR measurements exhibit bimodal *T2* distributions.

[2] Mark of Schlumberger

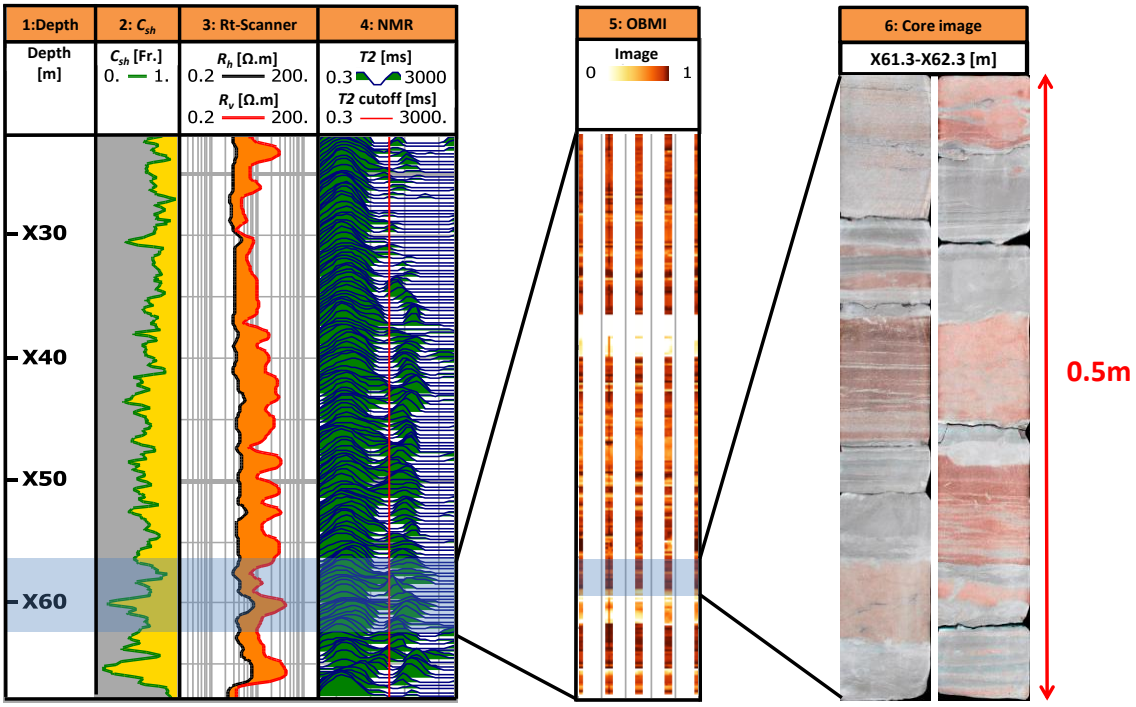

Figure 2.1: Identification of thinly bedded formations with Rt-Scanner, NMR, OBMI[3], and core images. Beds with thickness smaller than one foot are clearly visible on core photographs. Track 1: depth. Track 2: volumetric concentration of shale. Track 3: horizontal and vertical electrical resistivities. Track 4: NMR *T2* distributions. Track 5: OBMI image. Track 6: core photographs.

[3] Mark of Schlumberger

2.2 Calculations of Total Shale Concentration and Total Porosity

Estimation of volumetric concentration of shale is often associated with uncertainties. Reducing those uncertainties requires the comparison of estimated shale concentrations with at least two shale indicators and verification of results with core data. In this study, shale concentration was independently calculated with gamma ray and density-neutron logs and compared to each other for validation (Figure 2.2). Because formations under study are comprised of laminated sands, volumetric shale concentration, C_{sh}, from gamma ray was calculated using a linear function. The equation used was

$$C_{sh} = \frac{GR - GR_{sd}}{GR_{sh} - GR_{sd}}, \tag{2.1}$$

where GR_{sd} is gamma-ray reading in a pure sand interval, GR_{sh} is gamma-ray reading in a pure shale interval, and GR is gamma-ray log reading. In the studied reservoir, presence of clean sand was ambiguous. For shale concentration calculations, the gamma-ray value in a pure sand interval, GR_{sd}, was first assumed to be known and subsequently iteratively refined to obtain petrophysically consistent results.

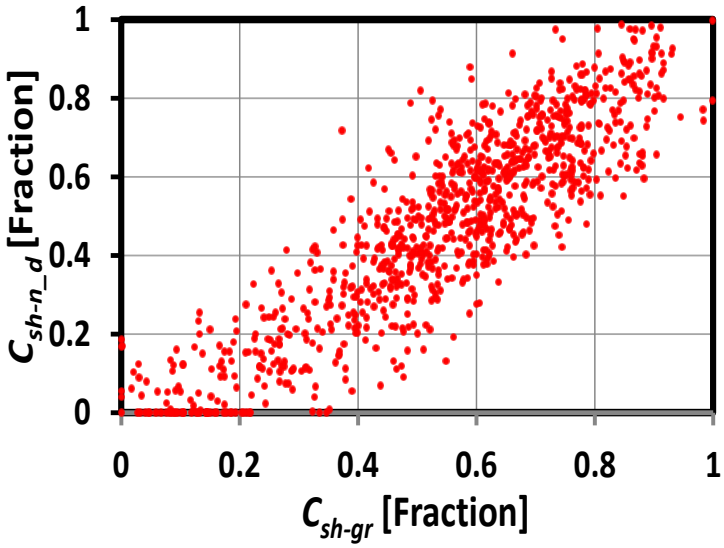

Figure 2.2: Comparison of volumetric concentrations of shale estimated with gamma ray and neutron-density logs. The scatter observed between the calculated shale concentrations with the two methods is attributed to the difference in vertical resolution of gamma-ray, density, and neutron logs (Figure 1.1).

Porosity was estimated with linear mineral inversion when conventional well logs were available. Figure 2.3 compares the porosity calculated with linear mineral inversion to NMR total porosity. Both porosities are in good agreement. The scatter observed between the two porosities is attributed to the difference in vertical resolution of the measurements involved in the calculations **(**Figure 1.1).

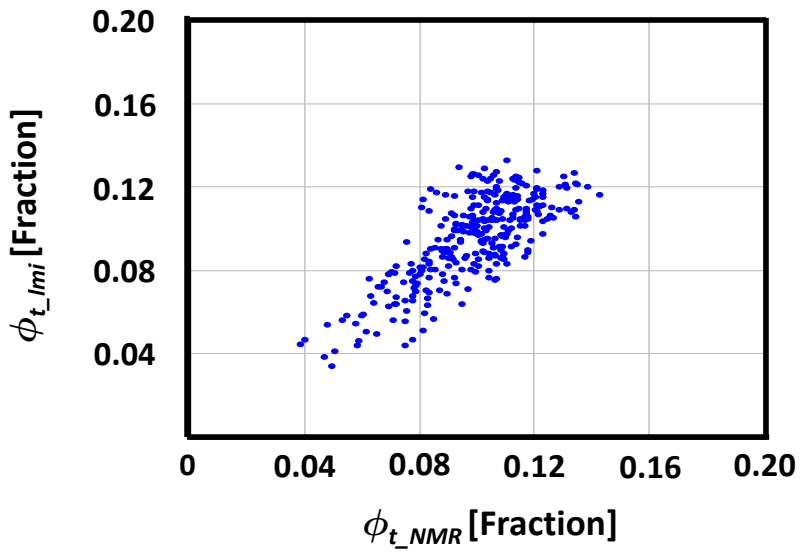

Figure 2.3: Comparison of total porosity estimated with NMR measurements to porosity estimated with linear mineral inversion. The scatter observed between the two porosities is due to the difference in vertical resolution of NMR and bulk density logs (Figure 1.1).

2.3 Quantification of Volumetric Laminar Shale Concentration

Accurate estimation of laminar shale concentration is of prime importance in the evaluation of hydrocarbon-in-place. Errors in laminar shale concentration propagate to the estimation of hydrocarbon-in-place. We combined the laminar shale concentration estimated with Thomas-Stieber's method, Rt-Scanner, and OBMI measurements to reduce uncertainty in the estimation of volumetric laminar shale concentration.

2.3.1 Volumetric Laminar Shale Concentration from OBMI Measurements

A threshold was selected on the OBMI R_{xo} curve to calculate laminar shale concentration from OBMI measurements. Values below the threshold were considered

representative of shale whereas values above the threshold were considered representative of sand. The threshold was iteratively refined until laminar shale concentrations estimated with OBMI measurements and core images were in acceptable agreement (Passey et al., 2006). The same threshold was then used to estimate laminar shale concentration in uncored depth intervals. To compare results, laminar shale concentration determined from OBMI measurements was spatially smoothed by applying an averaging filter of length equal to the vertical resolution of other wireline measurements (2 ft).

This method provided consistent results when OBMI measurements accurately detected all bed boundaries. Laminar shale concentration calculated can be over- or under-estimated depending upon the adjacent bed resistivities when bed thicknesses are lower than the vertical resolution of OBMI measurements,. Moreover, variations in formation fluid and grain size affect OBMI measurements, which in turn can lead to erroneous estimations of laminar shale concentration.

Figure 2.4, track 2 compares the OBMI R_{xo} curve and a core image. It can be observed that the OBMI R_{xo} curve broadly identifies variations in lithofacies that are visible on the core image. Additionally, shale laminations with thicknesses of a few millimeters are identified in the core images between the depth interval XX42-XX44 m. OBMI measurements cannot detect these shale laminations due to their limited vertical resolution (1.5 inches), thereby leading to underestimation of laminar shale concentration.

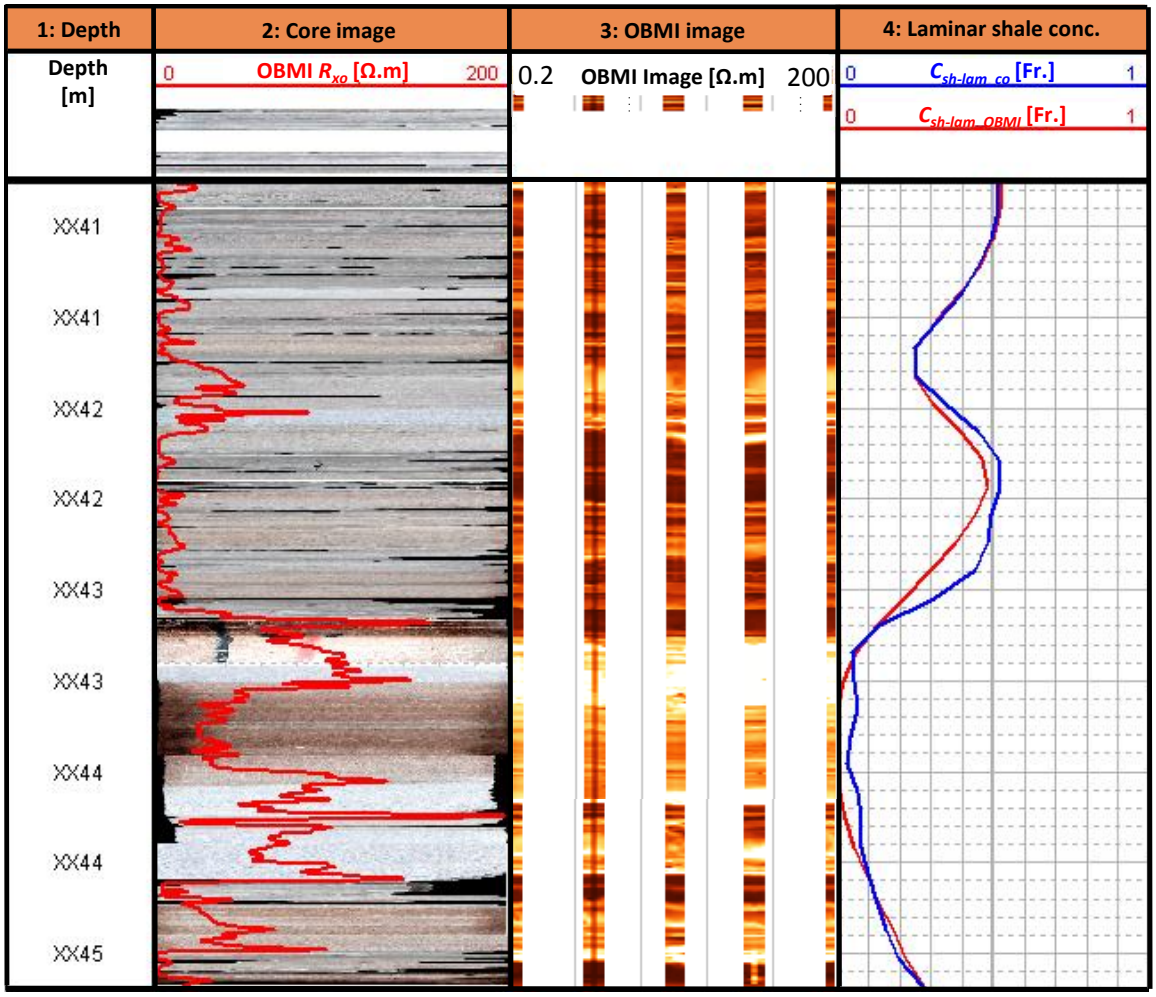

Figure 2.4: Comparison of the volumetric laminar shale concentrations estimated with OBMI measurements and core images. OBMI measurements detected most of the lithofacies which were observed on the core photographs. OBMI measurements underestimate laminar shale concentration between the depth interval XX42 and XX44 m due to presence of beds with thickness below the vertical resolution of OBMI measurements. Track 1: depth. Track 2: core photographs and OBMI resistivity curve. Track 3: OBMI image. Track 4: volumetric laminar shale concentrations estimated with core images and OBMI measurements.

2.3.2 Volumetric Laminar Shale Concentration from Thomas-Stieber's Method

Total shale concentration, C_{sh}, and total porosity, ϕ_t, are input to the Thomas-Stieber's model (T-S). This method is used to estimate volumetric laminar shale concentration, $C_{sh\text{-}lam}$, volumetric dispersed shale concentration, $C_{sh\text{-}disp}$, and sand porosity, ϕ_{sd}. In the present study, the T-S model was restricted to laminar and dispersed shale concentrations due to absence of structural shale. The primary assumption in the T-S model is that porosity end points, maximum sand porosity, $\phi_{sd\text{-}max}$, and shale porosity, ϕ_{sh}, remain constant in the analyzed depth section of the reservoir. However, when the formation has been reworked by diagenesis, porosity end points vary with depth. As emphasized earlier (Section 1.2), the studied formation is affected by diagenesis (calcite cementation, dissolution, etc.,) which causes porosity end points to vary, leading to errors in the estimation of volumetric laminar shale concentration. The equation used to estimate volumetric laminar shale concentration with the T-S model is given by

$$C_{sh-lam} = \frac{\phi_t - \phi_{sd-max} + C_{sh}(1-\phi_{sh})}{(1-\phi_{sd-max})}, \tag{2.2}$$

where $C_{sh\text{-}lam}$ is volumetric laminar shale concentration, ϕ_t is total porosity, $\phi_{sd\text{-}max}$ maximum sand porosity, C_{sh} is total volumetric shale concentration, and ϕ_{sh} is shale porosity.

2.3.3 Volumetric Laminar Shale Concentration from Rt-Scanner Measurements

Electrical anisotropy measured with multi-component induction measurements is affected by high-resistivity streaks, anisotropic sands, laminar shale, bioturbation, etc. In the case of isotropic sands interbedded between shale layers, laminar shale concentration values calculated with Rt-Scanner measurements and other methods are in good

agreement; however in other cases (anisotropic sands, high-resistivity streaks, bioturbation, etc.), laminar shale concentration derived from Rt-Scanner measurements is often over- or under-estimated when compared to laminar shale concentration obtained with other methods. Also, Rt-Scanner measurements have a relatively low vertical resolution (5 ft). Because of the above reasons, laminar shale concentration calculated with Rt-Scanner measurements is used only for comparison purposes.

2.3.4 Comparison of Volumetric Laminar Shale Concentrations

For calculations of laminar shale concentration from Thomas-Stieber's method, porosity end points, maximum sand porosity, $\phi_{sd\text{-}max}$, shale porosity, ϕ_{sh}, and total shale concentration, C_{sh}, were iteratively refined to obtain consistent results with the laminar shale concentrations obtained from Rt-scanner and OBMI measurements. The procedure used for estimation took into account the shortcomings of OBMI and Rt-Scanner measurements to deliver accurate values of laminar shale concentrations. These limitations were discussed in previous sections (sections 2.3.1, 2.3.2, and 2.3.3). Subsequently, laminar shale concentration obtained from Thomas-Stieber's method was used for calculations of hydrocarbon reserves.

Figure 2.5 compares laminar shale concentrations estimated with Thomas-Stieber's method, Rt-Scanner, and OBMI measurements. Laminar shale concentrations calculated with all three methods were in close agreement with each other within most of the depth intervals, except at X162-X165 m and X168-X173 m. At these depth intervals, OBMI measurements underestimated laminar shale concentration due to presence of shale beds with thicknesses lower than the vertical resolution of OBMI measurements. OBMI measurements are unable to resolve these shale laminations, which are visible on core images. Larger variations in laminar shale concentration estimated from OBMI

measurements and Thomas-Stieber's method were observed in comparison to laminar shale concentration calculated from Rt-Scanner measurements. This behavior is attributed to the lower vertical resolution of Rt-Scanner measurements (1.5 m) compared to the vertical resolution of gamma ray, bulk density, and OBMI measurements (Figure 1.1).

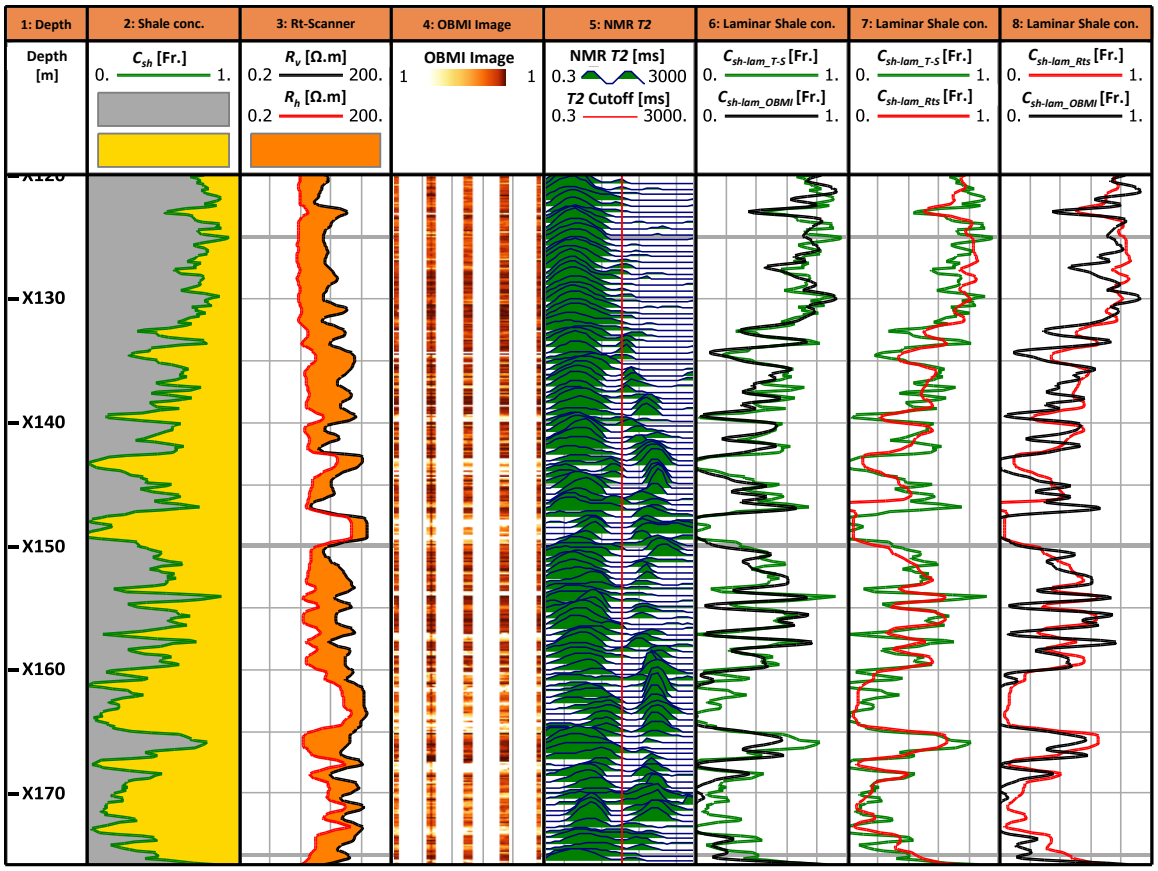

Figure 2.5: Comparison of volumetric laminar shale concentration estimated with different methods. Track 1: depth. Track 2: volumetric shale concentration. Track 3: vertical and horizontal electrical resistivities. Track 4: OBMI image. Track 5: NMR *T2* distributions. Track 6: volumetric laminar shale concentrations from Thomas-Stieber's method and OBMI measurements. Track 7: volumetric laminar shale concentrations from Thomas-Stieber's method and Rt-Scanner measurements. Track 8: volumetric laminar shale concentrations from Rt-Scanner and OBMI measurements.

2.4 PERMEABILITY ESTIMATION

Ostroff et al. (1999) reported that conventional methods based on NMR measurements tend to underestimate permeability in thinly bedded sand-shale sequences. In their study, they suggested to estimate permeability of sand units by removing the effect of laminar shale from NMR total porosity and bulk irreducible volume. This thesis extends Ostroff et al.'s (1999) permeability estimation method by using shoulder-bed corrected porosity and shale concentration logs in the calculations.

Permeability is estimated for sand units using Timur-Coates' equation. Shoulder-bed corrected total porosity, ϕ_{t_UT}, shoulder-bed corrected shale concentration, C_{sh_UT}, and total irreducible bulk volume, BVI_t, are used for the calculations. Total irreducible bulk volume is estimated from NMR measurements by selecting an appropriate *T2* cutoff. The best way to estimate *T2* cutoffs is through laboratory measurements of core samples. However, core laboratory samples were not available at the time of this study. Hence, a constant *T2* cutoff value equals to 35 ms was assumed in the calculations. Shoulder-bed corrected sand porosity, ϕ_{sd_UT}, sand irreducible bulk volume, BVI_{sd}, and sand permeability, K_{sd}, are calculated using the following equations:

$$BVI_{sd} = \frac{BVI_t - C_{sh-lam\_UT} BVI_{sh}}{(1 - C_{sh-lam\_UT})}, \tag{2.3}$$

$$\phi_{sd\_UT} = \frac{\phi_{t\_UT} - C_{sh-lam\_UT} \phi_{sh}}{(1 - C_{sh-lam\_UT})}, \tag{2.4}$$

and

$$K_{sd} = A(\phi_{sd\_UT})^B \left(\frac{BVFF_{sd}}{BVI_{sd}}\right)^C, \tag{2.5}$$

respectively, where BVI_{sd} is bulk irreducible volume in sand unit, BVI_t is total bulk irreducible volume of the rock, $C_{sh\text{-}lam\_UT}$ is shoulder-bed corrected volumetric laminar shale concentration, BVI_{sh} is shale bulk irreducible volume, ϕ_{sd_UT} is shoulder-bed corrected sand porosity, ϕ_{t_UT} is shoulder-bed corrected total porosity, ϕ_{sh} is shale porosity, $BVFF_{sd}$ is mobile bulk volume in sand unit, K_{sd} is sand permeability, and *A*, *B*, and *C* are constants.

It is important to emphasize that permeability is an anisotropic property in thinly bedded sand-shale sequences. This behavior originates from the fact that shale laminations restrict flow perpendicular to shale beds whereas flow parallel to shale beds is not affected (Minh and Sundararaman, 2011). Horizontal and vertical permeability of thinly bedded rock formations are calculated with the equations

$$K_h = K_{sd}(1 - C_{sh-lam}) + K_{sh}C_{sh-lam}, \tag{2.6}$$

and

$$K_v = \frac{1}{(\frac{1 - C_{sh-lam}}{K_{sd}}) + (\frac{C_{sh-lam}}{K_{sh}})}, \tag{2.7}$$

respectively, where $C_{sh\text{-}lam}$ is volumetric laminar shale concentration, K_h is rock horizontal permeability, K_v is rock vertical permeability, K_{sd} is sand permeability, and K_{sh} is shale permeability. Shale permeability is assumed negligible in the calculations and sand permeability, K_{sd}, is calculated using equation (2.5).

Figure 2.6 shows the results obtained from a synthetic case to emphasize the sensitivity of horizontal rock permeability to varying laminar and dispersed shale concentration, while keeping total shale concentration constant. Table 2.1 summarizes the parameters used in the calculations. Permeability is calculated using equations (2.5) and

(2.6). Results indicate that rock permeability increases with increasing laminar shale concentration, while keeping the total shale concentration constant. Conventional methods for estimating permeability assume that shale is dispersed in the pore space of the rock. This assumption leads to underestimation of permeability in laminated rocks. Results from this synthetic case suggest that accurate calculations of laminar and dispersed shale concentrations are essential for obtaining reliable estimations of permeability.

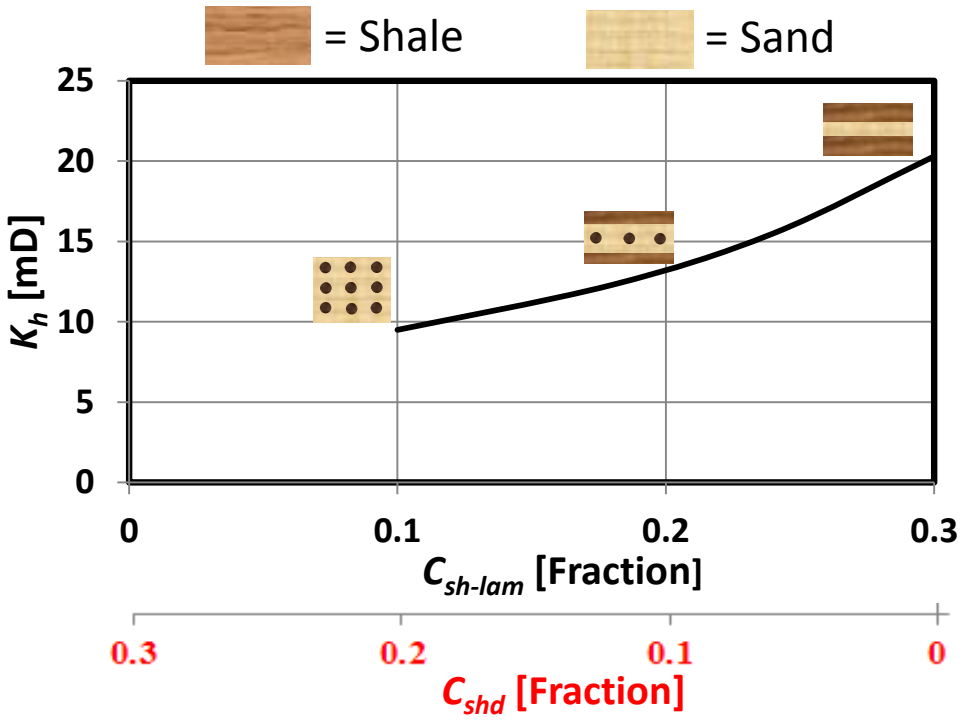

Figure 2.6: Variations of permeability with volumetric laminar and dispersed shale concentration while keeping total shale concentration constant. Table 2.1 summarizes the parameters assumed for the calculations.

Petrophysical Property	Value	Units
NMRPhit	0.25	[Fraction]
NMRBft	0.1	[Fraction]
C_{sh}	0.3	[Fraction]
A	100	[mD]
B	2	[-]
C	2	[-]

Table 2.1: Summary of assumed petrophysical properties for the synthetic case. Figure 2.6 shows the corresponding results.

2.5 SHOULDER-BED CORRECTIONS OF WELL LOGS

Borehole measurements yield average responses in thinly bedded sand-shale sequences, which may lead to incorrect assessments of petrophysical properties. In this study, we corrected total porosity and total shale concentration for shoulder-bed effects by implementing the concept of Common Stratigraphic Framework (CSF) introduced by Voss et al. (2009). Shoulder-bed corrected logs were used to estimate permeability and sand reservoir quality. In the studied reservoir, core samples were mainly acquired from rock sand units. Sand porosity calculated with shoulder-bed corrected logs was compared to core measured porosities. Figure 2.7 compares shoulder-bed corrected and core petrophysical properties. On average, shoulder-bed corrected logs yield 16% better agreement with core measurements in terms of correlation coefficient. However, we were unable to achieve a better correlation between shoulder-bed corrected porosity and core porosity due to differences in the volume of rock investigated by core plugs and wireline measurements.

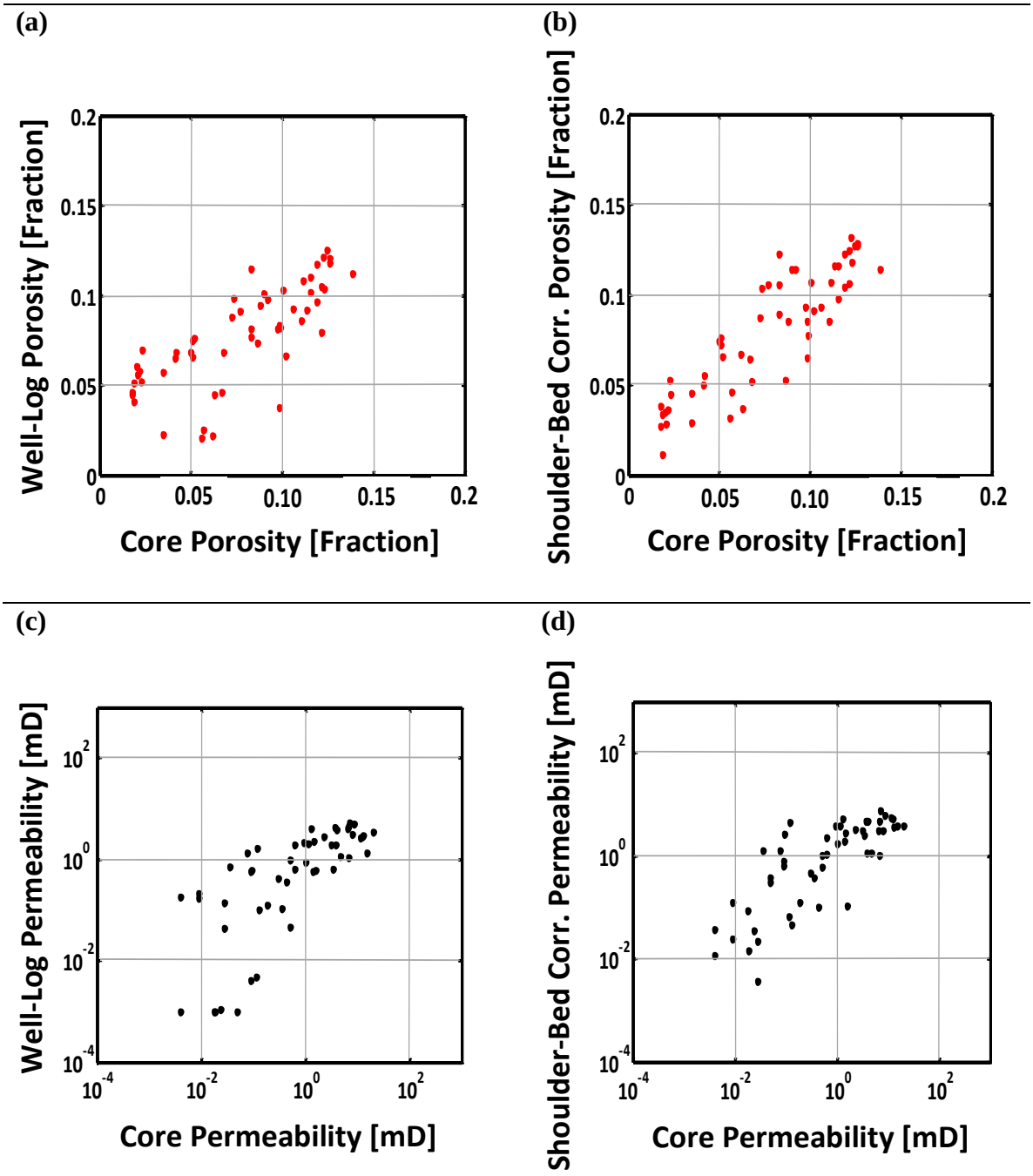

Figure 2.7: Comparison of well-log and shoulder-bed corrected permeability. On average, shoulder-bed corrected permeability exhibits 16% better agreement with core measurements (in terms of the correlation coefficient).

2.6 SAND RESERVOIR QUALITY

Hydraulic rock classification diagnoses storage and flow capacity of reservoir rocks. Several hydraulic rock classification methods have been developed in the past, including Winland's *R35* (Pittman, 1992), flow zone index (FZI) (Amaefule et al., 1993), and Leverett's reservoir quality index, $\mathrm{RQI} = \sqrt{k/\phi}$ (Leverett, 1941).

In this study, we implemented a hydraulic rock classification approach, i.e. Leverett's reservoir quality index, $\mathrm{RQI} = \sqrt{k/\phi}$, to quantify sand reservoir quality. Porosity and permeability were estimated with shoulder-bed corrected logs. Rocks were categorized into three petrofacies according to their corresponding RQI values: Rock type 1, with RQI values lower than 1.5, exhibits negligible reservoir quality, while Rock Type 3, with RQI values greater than 5, exhibits the best reservoir quality.

For each rock type, thin-sections, SEM images, and capillary pressure curves were analyzed across the reservoir. Figure 2.8 describes the corresponding RQI ranges and thin section images for each rock type. The study showed that sand reservoir quality increased as grain size and interconnected porosity increased, and decreased with an increase of calcite and authigenic clay cementation. Capillary pressure showed a similar trend for each rock type; entry capillary pressure increased with a decrease in sand reservoir quality (Figure 2.9).

Rock Types	$\sqrt{\frac{K\ [mD]}{\phi\ [Fr.]}}$	Thin Sections
RT 1	< 1.5	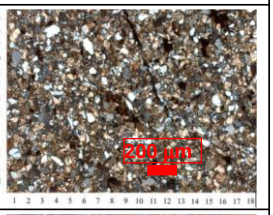
RT 2	$\geq 1.5,$ < 5	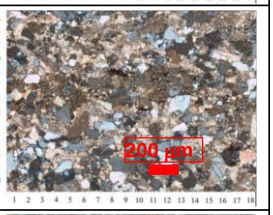
RT 3	≥ 5	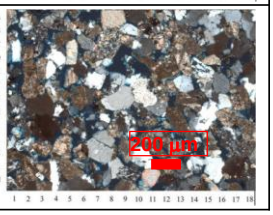

Figure 2.8: Rock classification using Leverett's Rock Quality Index (RQI) method. Representative thin sections are shown for each rock type. Rock petrophysical quality increases with an increase in both grain size and interconnected porosity and decreases with an increase in both calcite and authigenic clay cementation.

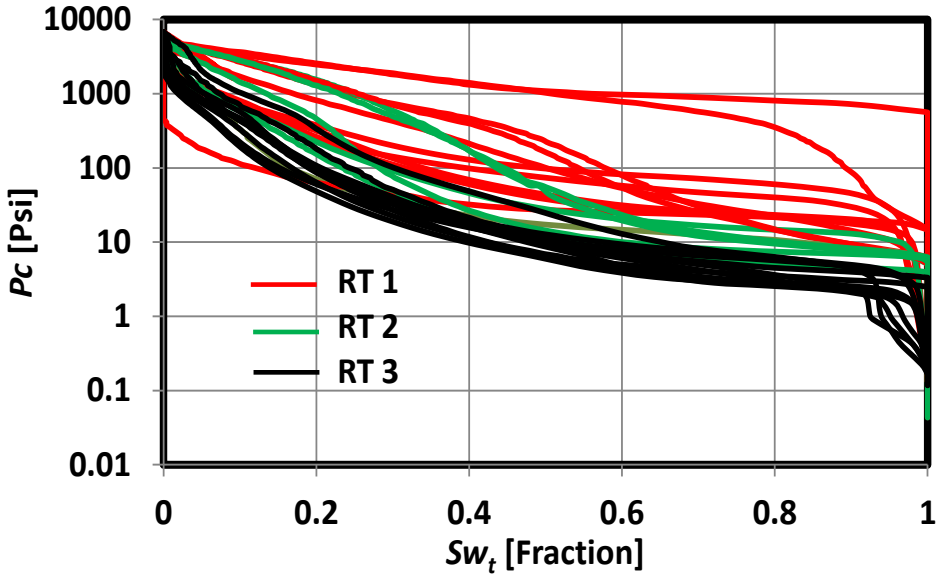

Figure 2.9: Clustered capillary pressure curves for each rock type (Rock Quality Index). Entry capillary pressure increases with a decrease in sand reservoir quality.

2.7 Numerical Simulations of NMR Measurements

We performed numerical simulations of NMR *T2* distributions at selected depth intervals to validate petrophysical properties determined from anisotropy analysis. Across thinly bedded formations, NMR measurements provide an averaged response of adjacent beds due to their relatively large volume of investigation. To reproduce this averaging effect, we intermixed *T2* distributions of sand and shale layers.

Figure 2.10 shows the sequential steps followed by the numerical simulations of NMR *T2* distributions. Numerical simulations were performed to generate *T2* distributions for sand and shale layers, assuming random pore-size distributions, and specific volumes of in-situ fluid concentration, in-situ fluid properties, and mineral compositions. The *T2* distributions obtained for individual beds were then converted into time decay sequences. The equation used was

$$\psi(t) = \sum_{i=1}^{i=m} \phi_i e^{-[t/T2_i]}, \tag{2.8}$$

where m is number of bins, ϕ_i is partial porosity of each bin, ψ is time decay sequence, and *T2* is transverse relaxation time. Decay sequences obtained for individual beds were averaged using the equation

$$\psi_{av} = C_{sh-lam}\psi_{sh} + (1 - C_{sh-lam})\psi_{sd}, \tag{2.9}$$

where ψ_{sh} is time decay sequence for the shale layer, ψ_{sd} is time decay sequence for the sand layer, $C_{sh\text{-}lam}$ is volumetric laminar shale concentration, and ψ_{av} is the decay sequence for the total bulk volume of the rock. Finally, the averaged time decay sequence was inverted into a *T2* distribution. Petrophysical properties (pore-size distribution, fluid concentration, etc.) assumed in the numerical simulations were iteratively refined until an acceptable agreement was achieved between field and numerically simulated NMR *T2* distributions.

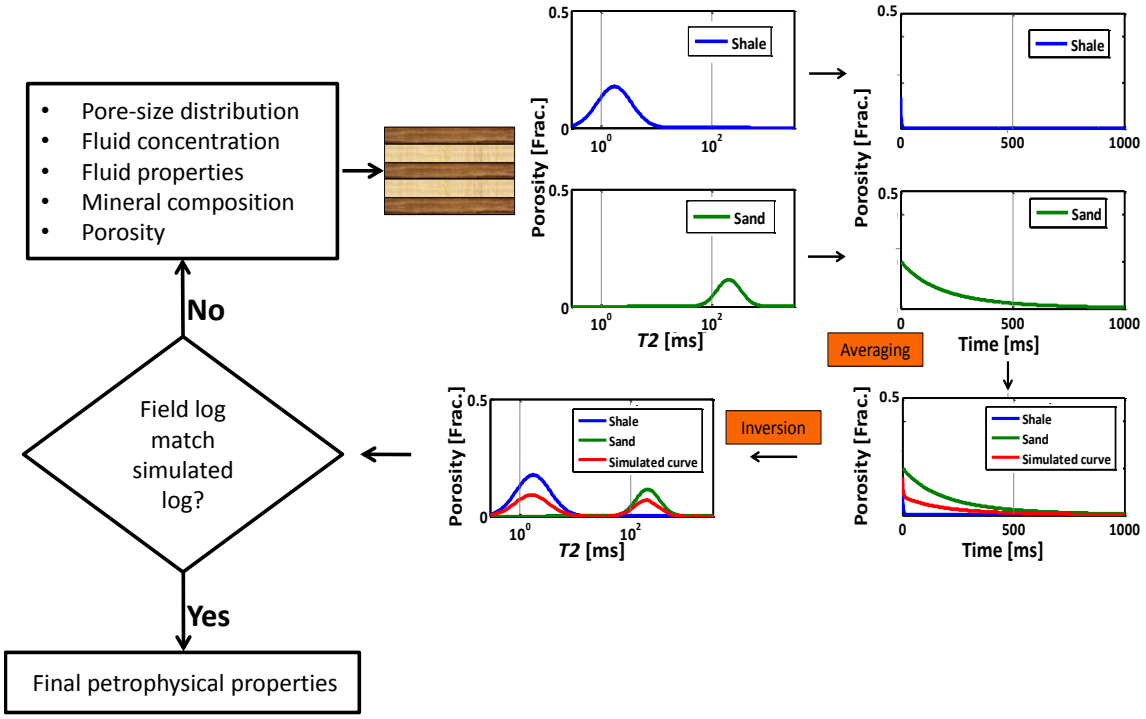

Figure 2.10: Flowchart describing the sequential steps adopted in this thesis to perform numerical simulations of NMR *T2* distributions. Input parameters were iteratively refined until field and numerically simulated NMR *T2* waveforms were in close agreement.

2.7.1 Synthetic Cases

Two synthetic cases are considered to appraise the sensitivity of fluid peak locations and amplitude to changes in *T2* bulk of oil and fluid concentrations. Numerical simulations of NMR *T2* distributions were performed assuming specific values of pore-size distribution, fluid concentration, mineral composition, surface relaxivities, and bulk fluid *T2*. Table 2.2 summarizes the parameters used in the numerical simulations.

Figure 2.11 shows the sensitivity of the oil *T2* peak to increasing values of *T2* bulk. The oil *T2* peak (identified with green) moves toward the right with increasing

values of *T2* bulk of oil. A larger value of *T2* bulk of oil corresponds to low-viscosity oil, and vice versa.

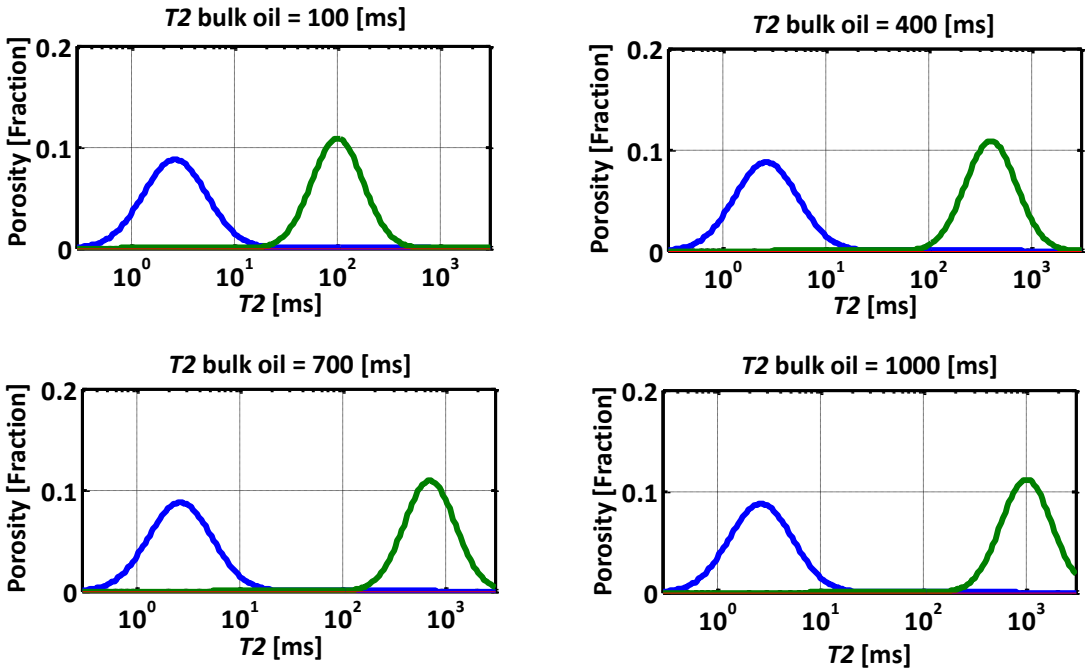

Figure 2.11: Sensitivity of the oil *T2* peak (green) to variations of *T2* bulk of oil; the *T2* peak of oil moves toward right with a decrease in oil viscosity.

Figure 2.12 describes results obtained from a synthetic case emphasizing the change in partial porosity of mobile water and oil *T2* peaks due to changes in fluid saturations. It can be observed that partial porosity values associated with oil decrease with a decrease in oil saturation. Similarly, partial porosity values associated with mobile water increase with an increase in water saturation.

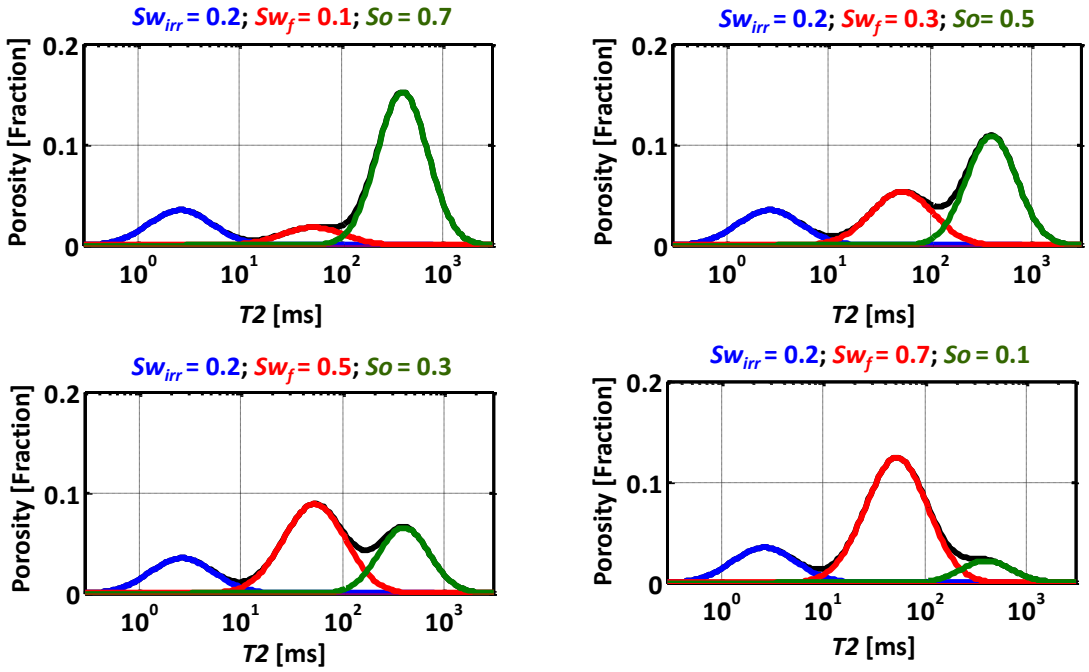

Figure 2.12: Sensitivity of water and oil *T2* peaks to changes of fluid concentration; Sw_{irr} is irreducible water saturation, Sw_f is mobile water saturation, and *So* is oil saturation.

Variable	Value	Units
Transverse surface relaxivity of quartz, ρ_{qz}	30	[µm/s]
Transverse surface relaxivity of calcite, ρ_{ca}	1.5	[µm/s]
Transverse surface relaxivity of clay, ρ_{cl}	5	[µm/s]
Transverse bulk relaxation time of water, $T2_{bulk\_wr}$	2000	[ms]
Transverse bulk relaxation time of oil, $T2_{bulk\_oil}$	400	[ms]
Porosity, ϕ_t	0.15	[Fraction]

Table 2.2: Summary of some of the properties assumed in the numerical simulations of *T2* distributions for synthetic cases.

Chapter 3: Rock Classification and Corresponding Petrophysical Interpretation Methods

This chapter describes the method used to classify rocks. It also discusses the interpretation method adopted in the study for each rock type.

Factors such as laminar shale, bioturbation, high-resistivity streaks, and anisotropic sands can affect the electrical anisotropy yielded by multi-component induction measurements. No single interpretation method provides petrophysically consistent properties for all the rock types encountered in the reservoir. Accordingly, rocks were classified based on the source of electrical anisotropy. Different interpretation methods were then applied for each rock type.

Rocks were classified into three categories:

(1) Laminated beds with isotropic sand units,

(2) Anisotropic sands, and

(3) Low-porosity, high-resistivity streaks.

3.1 Laminated Beds with Isotropic Sand Units

Sediments are composed of thinly bedded sequences of isotropic sand and isotropic/anisotropic shale layers (turbidite, deltaic, etc.). Figure 3.1 describes the resistivity response for this rock type. Electrical anisotropy is generated by the contrasting difference between resistivity values of hydrocarbon-bearing isotropic sands and shale layers. Horizontal resistivity is biased toward low resistivity values due to the relatively high electrical conductivity of shale layers. By contrast, vertical resistivity is more affected by hydrocarbon-bearing sand units (Fanini et al., 2001; Mollison et al., 2001).

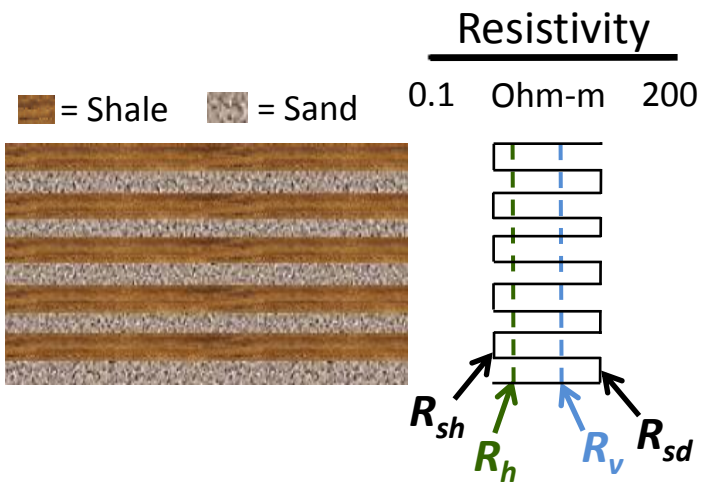

Figure 3.1: Description of rocks comprising alternating thin beds of isotropic sand and isotropic/anisotropic shale layers; R_{sh} is shale resistivity, R_h is horizontal resistivity, R_v is vertical resistivity, and R_{sd} is sand resistivity.

3.1.1 Interpretation Method

Figure 3.2 describes the workflow adopted in this study for petrophysical interpretation of rocks composed of isotropic sands interbedded between isotropic/anisotropic shale layers. The method removes the effect of laminar shale on resistivity and porosity. Sand porosity is estimated with Thomas-Stieber's method whereas sand resistivity is obtained with the tensor resistivity model. Further, the dual-water equation or its equivalent is used to estimate hydrocarbon reserves in sand layers. Estimated petrophysical properties were then cross-validated with core measurements and by performing numerical simulations of NMR *T2* distributions. Input parameters (total shale concentration, laminar shale concentration, dispersed shale concentration, porosity, etc.), were iteratively refined to secure a petrophysically consistent model.

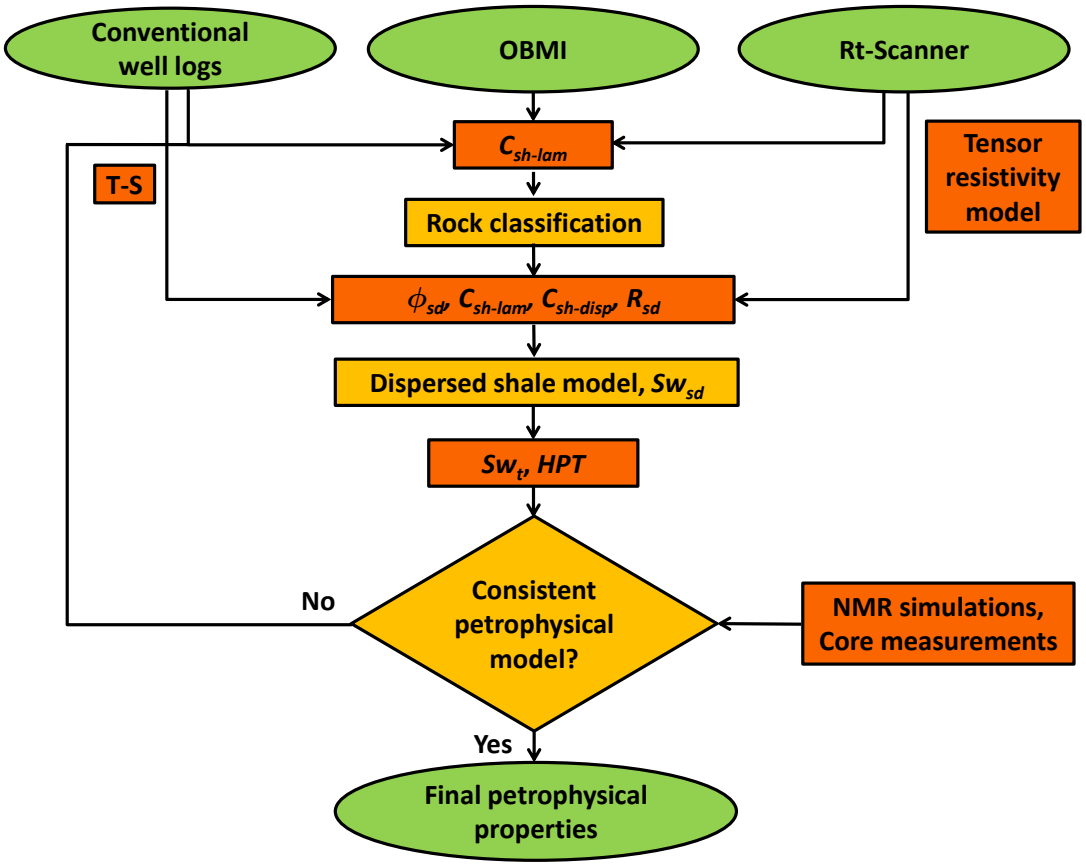

Figure 3.2: Workflow adopted in this study for the petrophysical evaluation of rocks composed of isotropic sands interbedded between isotropic/anisotropic shale layers. Input parameters are iteratively refined until obtaining petrophysically consistent properties. $C_{sh\text{-}lam}$: volumetric laminar shale concentration; $C_{sh\text{-}disp}$: dispersed shale concentration in the sand unit; Sw_t: total water saturation; ϕ_{sd}: sand porosity; R_{sd}: sand resistivity; Sw_{sd}: sand water saturation; HPT: Hydrocarbon pore-thickness; T-S: Thomas-Stieber's method (Thomas and Stieber, 1975).

The following are the sequential steps and equations used for the petrophysical evaluation of rocks composed of isotropic sands interbedded between shale layers:

(1) Shale concentration is calculated with gamma ray using a linear function. The shale concentration thus obtained is compared to shale concentration derived with neutron-density logs.

(2) Porosity is estimated with linear mineral inversion. Porosity thus calculated is compared to NMR total porosity.

(3) Laminar shale concentration is estimated via different approaches such as Thomas-Stieber's method (Thomas and Stieber, 1975), Rt-Scanner, and OBMI measurements.

(4) Dispersed shale concentration is calculated by subtracting laminar shale concentration from total shale concentration and then normalizing it with sand fraction. The equation used was

$$C_{sh-disp} = \frac{C_{sh} - C_{sh-lam}}{1 - C_{sh-lam}}, \tag{3.1}$$

where $C_{sh\text{-}disp}$ is dispersed shale concentration in sand units, C_{sh} is total volumetric shale concentration, and $C_{sh\text{-}lam}$ is volumetric laminar shale concentration.

(5) Sand porosity was estimated using the equation

$$\phi_{sd} = \frac{\phi_t - C_{sh-lam}\phi_{sh}}{1 - C_{sh-lam}}, \tag{3.2}$$

where $C_{sh\text{-}lam}$ is volumetric laminar shale concentration, ϕ_t is total porosity, ϕ_{sh} is shale porosity, and ϕ_{sd} is sand porosity.

(6) Tensor resistivity equations were used to calculate laminar shale concentration and sand resistivity, while horizontal and vertical shale resistivities were provided as input. Horizontal and vertical shale resistivities were identified from representative shale intervals. The equations used for that purpose were

$$\frac{1}{R_h} = \frac{C_{sh-lam}}{R_{shh}} + \frac{1-C_{sh-lam}}{R_{sd}}, \tag{3.3}$$

and

$$R_v = C_{sh-lam}R_{shv} + (1-C_{sh-lam})R_{sd}, \tag{3.4}$$

where $C_{sh\text{-}lam}$ is volumetric laminar shale concentration, R_{shh} is horizontal shale resistivity, R_{shv} is vertical shale resistivity, R_{sd} is sand resistivity, R_h is horizontal resistivity, and R_v is vertical resistivity.

(7) The dispersed shale water saturation model was then used to estimate water saturation in sand units. In this study, the dual-water saturation equation was used for calculations of water saturation. The equations used were

$$\frac{1}{R_{sd}} = \frac{\phi_{sd}^m Sw_{sd}^n}{a}\left[\frac{1}{R_w} + \frac{Sw_b}{Sw_{sd}}\left(\frac{1}{R_{wb}} - \frac{1}{R_w}\right)\right], \tag{3.5}$$

$$Sw_b = \frac{C_{sh-disp}\phi_{sh}}{\phi_{sd}}, \tag{3.6}$$

and

$$R_{wb} = \frac{\phi_{sh}^{m} R_{sh}}{a}, \tag{3.7}$$

where R_{sd} is sand resistivity, ϕ_{sd} is sand porosity, Sw_b is bound-water saturation in the sand unit, Sw_{sd} is total water saturation in the sand unit, R_w is electrical resistivity of connate water, R_{wb} is bound-water resistivity, $C_{sh\text{-}disp}$ is dispersed shale concentration in sand units, ϕ_{sh} is shale porosity, R_{sh} is shale resistivity, a is Archie's Winsauer factor, m is Archie's porosity exponent, and n is Archie's saturation exponent. NMR porosity of the representative shale segment was assumed equal to shale porosity.

(8) Water saturation in the sand unit was then converted to total rock water saturation. The equation used was

$$Sw_t = \frac{Sw_{sd}\phi_{sd}(1 - C_{sh-lam}) + (C_{sh-lam}\phi_{sh})}{\phi_t}, \tag{3.8}$$

where Sw_t is total water saturation, Sw_{sd} is sand water saturation, ϕ_{sd} is sand porosity, $C_{sh\text{-}lam}$ is volumetric laminar shale concentration, ϕ_{sh} is shale porosity, and ϕ_t is total porosity. Petrophysical properties thus determined were validated with numerical simulations of NMR *T2* distributions and core measurements.

(9) Finally, *HPT* was estimated using the formula

$$HPT = \phi_{sd}(1 - Sw_{sd})(1 - C_{sh-lam}), \tag{3.9}$$

where *HPT* is hydrocarbon pore-thickness, ϕ_{sd} is sand porosity, Sw_{sd} is water saturation in sand units, and $C_{sh\text{-}lam}$ is volumetric laminar shale concentration.

3.2 ANISOTROPIC SANDS

Sediments are composed of alternating layers of fine grains and coarse grains. Such rocks are commonly encountered in aeolian sands and T_a facies of Bouma turbidite sequences. Figure 3.3 describes electrical resistivity response for this rock type. Fine grain layers have higher capillary-bound water when compared to capillary-bound water in coarse grains. In the case of hydrocarbon-saturated formations, differences in capillary-bound water saturation in fine and coarse grains cause differences in resistivity, which give rise to electrical anisotropy.

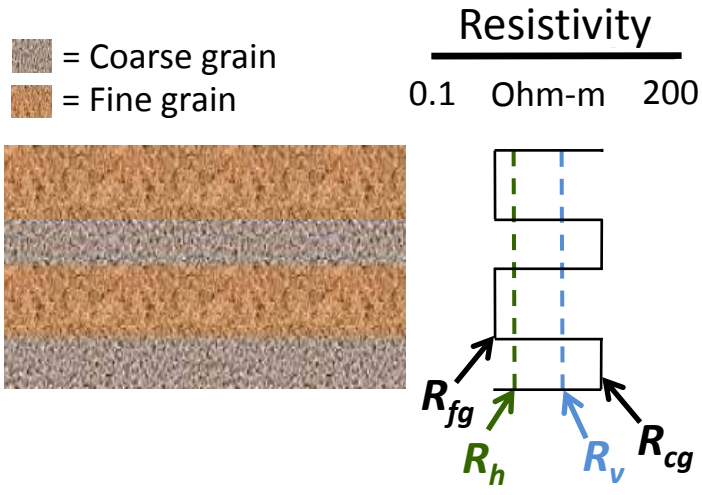

Figure 3.3: Description of anisotropic sand and corresponding electrical resistivity profile. Electrical anisotropy originates from alternating beds of fine and coarse grains; R_{fg} is resistivity of fine grain, R_h is horizontal resistivity, R_v is vertical resistivity, and R_{cg} is resistivity of coarse grain.

Tensor resistivity equations are implemented for individual bed resistivities, while fine- and coarse-grain concentrations are obtained from external sources, such as NMR measurements. Subsequently, water saturation was estimated in fine- and coarse-grained layers using Archie's or shaly-sand models (dual-water, Waxman-Smits, etc.). The equations used were

$$\frac{1}{R_h} = \frac{C_{fg}}{R_{fg}} + \frac{C_{cg}}{R_{cg}}, \tag{3.10}$$

$$R_v = C_{fg} R_{fg} + C_{cg} R_{cg}, \tag{3.11}$$

and

$$C_{fg} + C_{cg} = 1, \tag{3.12}$$

where C_{fg} is volumetric concentration of fine grain, C_{cg} is volumetric concentration of coarse grain, R_{fg} is resistivity of fine grain, R_{cg} is resistivity of coarse grain, R_h is horizontal resistivity, and R_v is vertical resistivity. Further, water saturation was calculated for individual beds by implementing the dispersed shaly-sand equations. This interpretation method has been documented in several publications, including those of Shray and Borbas (2001), and Schöen et al. (1999).

3.3 HIGH-RESISTIVITY STREAKS

Reservoir rocks are composed of alternating beds of low-porosity, high-resistivity streaks and sand layers. Figure 3.4 describes the electrical resistivity response for this rock type. Low-porosity streaks can originate from a high degree of calcite cementation. We implemented the high-resolution method in the petrophysical evaluation of this rock type.

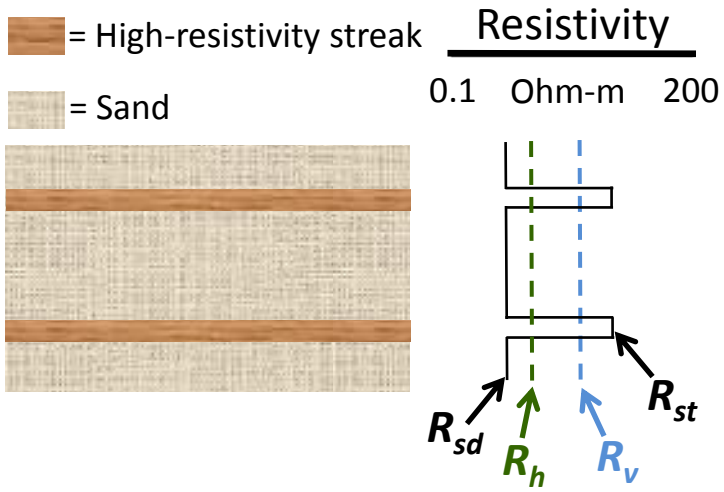

Figure 3.4: Description of a rock with thin high-resistivity streaks. Electrical anisotropy is generated due to alternating beds of low-porosity, high-resistivity streaks and sand layers; R_{st} is resistivity of low-porosity, high-resistivity streaks, R_h is horizontal resistivity, R_v is vertical resistivity, and R_{sd} is sand resistivity.

3.3.1 High-Resolution Interpretation Method

The high-resolution approach is an effective way to evaluate thinly bedded formations in which high-resolution measurements, such as OBMI, are integrated with the petrophysical interpretation procedure. An advantage of the high-resolution approach over conventional petrophysical analysis is that the former yields detailed petrophysical

properties of each individual bed. On the other hand, conventional petrophysical analysis yields only average petrophysical properties across thinly bedded formations due to the limited vertical resolution of wireline measurements. Thus, in thinly bedded formations the high-resolution approach delivers a more accurate estimate of hydrocarbon reserves when compared to conventional petrophysical analysis (Passey et al., 2006, Bastia et al., 2007).

In order to implement the high-resolution approach, we utilized the concept of Common Stratigraphic Framework (CSF) (Voss et al., 2009). Figure 3.5 shows the sequential steps followed by the high-resolution method to evaluate thinly bedded formations. Petrophysical beds are constructed by detecting bed boundaries from the OBMI R_{xo} curve and/or core images. For each petrophysical bed, earth-model properties are populated and numerical simulations of well logs are performed from the populated earth-model properties. Earth-model properties are iteratively refined until field and numerically simulated logs are in agreement. The dispersed shaly-sand equation (dual-water saturation model) was implemented to estimate water saturation in sand layers. Calculated petrophysical properties were subsequently validated with core measurements.

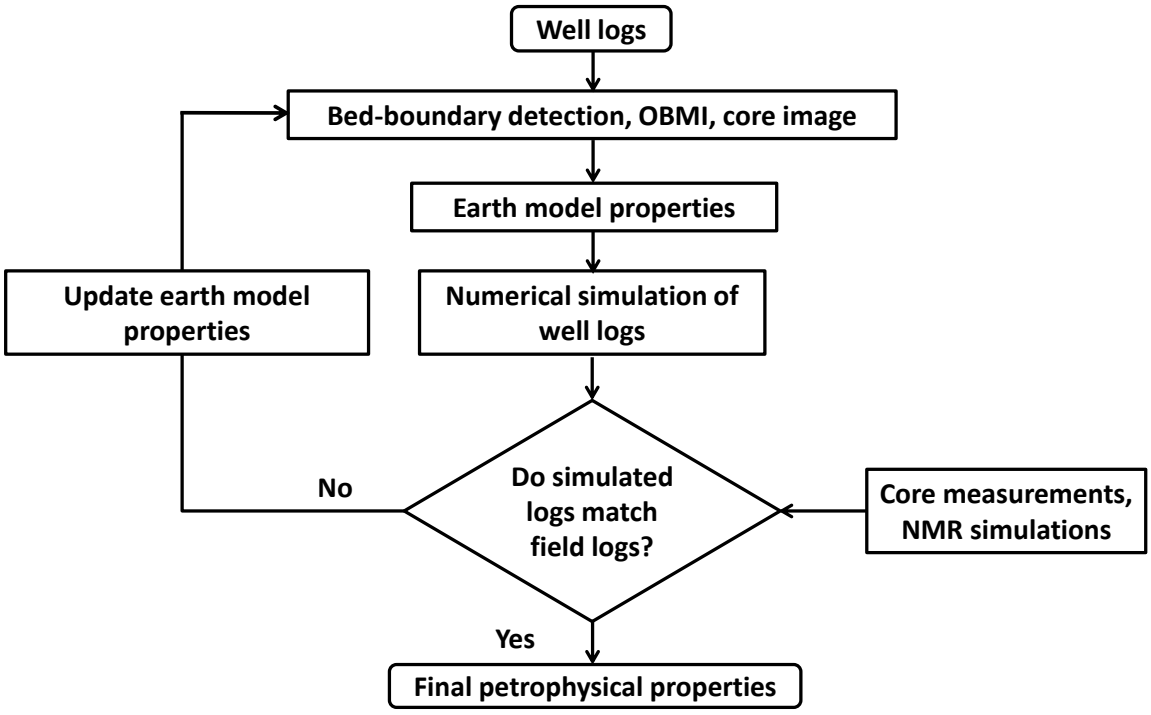

Figure 3.5: Flowchart describing the high-resolution method for petrophysical evaluation of thinly bedded formations. This method yields detailed petrophysical properties for each individual bed. Petrophysical properties obtained are validated with core measurements and NMR numerical simulations.

3.3.2 Limitations of the High-Resolution Interpretation Method

The accuracy and reliability of the high-resolution method of interpretation depend on the accurate detection of bed boundaries. Petrophysical analysis with the high-resolution method yields incorrect and non-unique solutions when bed thicknesses are lower than the vertical resolution of OBMI measurements (1.5 inches). However, consistent petrophysical properties were determined when beds were thicker than 3 inches. Other methods for petrophysical evaluation of thinly bedded formations, such as

the stochastic approach or anisotropy analysis, tend to yield petrophysically consistent results when beds are thinner than 3 inches.

Chapter 4: Field Cases

This chapter documents the application of the developed interpretation workflow in thinly bedded sand-shale sequences encountered in four wells within the studied reservoir.

All wells under study are vertical and were drilled with an 8.5 inch bit and oil-base mud. Measurements include a complete suite of standard logs and advanced logs such as multi-component induction and NMR measurements. Resistivity images, core images, and core laboratory measurements were also available in a few wells. Table 4.1 summarizes the well logs and core measurements available for petrophysical analysis in wells within the studied reservoir.

4.1 Quick-Look Analysis

In general, well logs exhibited good quality. Likewise, caliper logs indicated good borehole conditions. However, we observed a few inconsistencies in the PEF log along a few depth intervals due to presence of barite in the drilling mud.

In this study, neutron porosity is plotted in limestone porosity units. Due to presence of dispersed shale, the dual-water equation was used to estimate water saturation in sand units. Table 4.2 summarizes the petrophysical parameters used for well-log interpretation.

Data	Well: α	Well: β	Well: γ	Well: τ	Units
Gamma ray	✓	✓	✓	✓	[GAPI]
Apparent resistivity	✓	✓	✓	✓	[Ohm-m]
Density	✓	✓	✓	✓	[gm/cc]
Neutron	✓	✓	✓	✓	[Fraction]
PEF	✓	✓	✓	✓	[b/e]
Rt-Scanner	✓	✓	✓	✓	[Ohm-m]
OBMI	✓	×	×	✓	[Ohm-m]
NMR	✓	✓	✓	✓	[ms]
Core laboratory meas.	✓	✓	×	✓	[-]
Core photographs	✓	×	×	✓	[-]

Table 4.1: Summary of well logs and core measurements available for petrophysical analysis in Wells α, β, γ, and τ.

Petrophysical Property	Well: α	Well: β	Well: γ	Well: τ	Units
GR_{sh}	20	23	19	19	[GAPI]
GR_{sd}	72	84	72	87	[GAPI]
a	1	1	1	1	[-]
m	2.1	2.1	2.1	2.1	[-]
n	2	2	2	2	[-]
R_{sh}	2.45	2	2.5	2	[Ohm-m]
R_{shh}	2.45	2	2.5	2	[Ohm-m]
R_{shv}	3.5	2.5	3	3.8	[Ohm-m]
ϕ_{sh}	0.13	0.135	0.15	0.12	[Fraction]
A	12,000	50	50	40	[mD]
B	0.3	2	2	2	[-]
C	3.8	2	2	2	[-]
Salt concentration	35,000	35,000	35,000	35,000	[ppm NaCl]

Table 4.2: Summary of properties assumed for petrophysical analysis in Wells α, β, γ, and τ.

Thomas-Stieber's (T-S) crossplot facilitates the identification and quantification of laminar, dispersed, and structural shale concentration. Figure 4.1 compares the T-S crossplots constructed for interpreted depth intervals in different wells within the studied reservoir. Crossplots for different wells indicate that the formation is affected by calcite and/or authigenic clay cementation. They also indicate presence of a highly heterogeneous formation. Maximum sand porosity, $\phi_{sd\text{-}max}$, varies between 14 and 20%, whereas shale porosity, ϕ_{sh}, ranges between 12 and 15%.

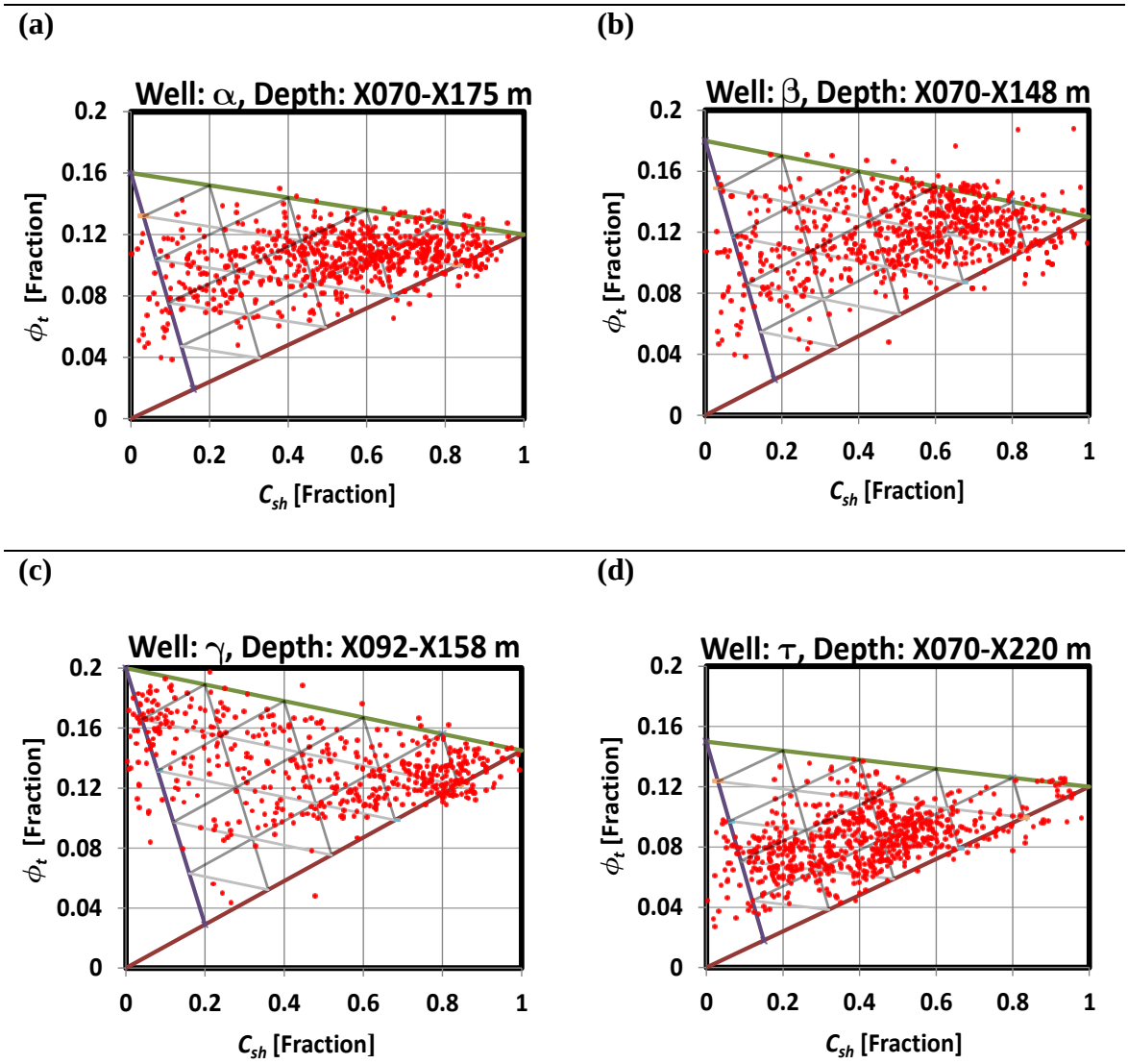

Figure 4.1: Comparison of Thomas-Stieber's crossplots constructed for different depositional sequences encountered in different wells within the studied reservoir. These crossplots indicate that formations under study are affected by calcite and/or authigenic clay cementation.

Klein's plot (Minh et al., 2007) permits a quick-look interpretation analysis to estimate shale anisotropy, volumetric laminar shale concentration, sand resistivity, presence of water-bearing zone, etc. Figure 4.2 compares Klein's plots constructed for interpreted depth intervals in different wells; they indicate that shale anisotropy values range between 1.5 and 2 in the studied reservoir. In all plots, data points fall in the upper wing of the butterfly chart, thereby indicating that horizontal resistivity is higher than shale resistivity. This behavior further suggests absence of complete water-bearing formations. A maximum sand resistivity of 150 ohm-m was observed in Well γ, whereas in the remaining wells, maximum sand resistivity was approximately 60 ohm-m.

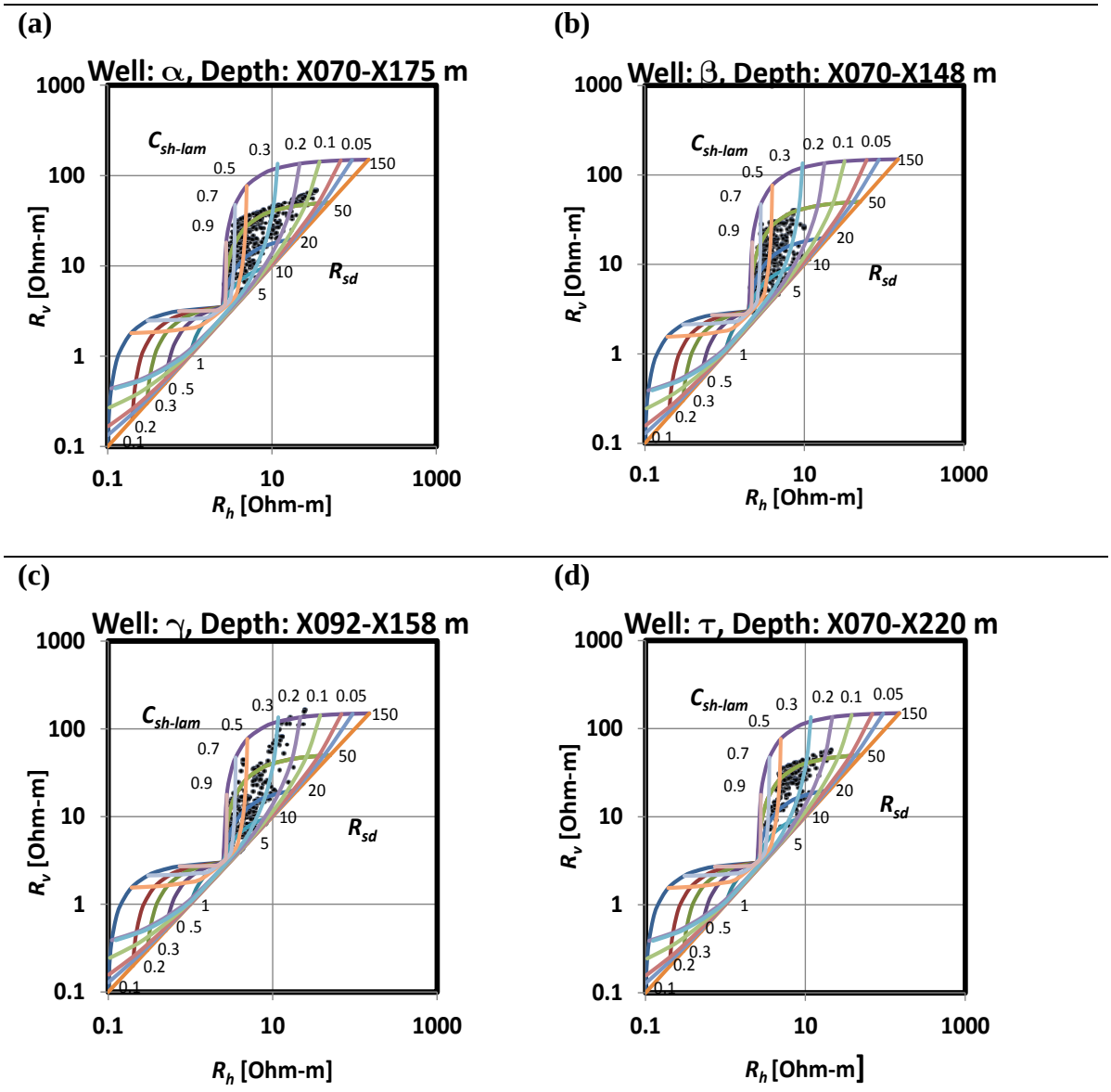

Figure 4.2: Comparison of Klein's plot (Minh et al., 2007) for different wells within the studied reservoir. All data points lie in the upper wing of the butterfly chart, thereby indicating that horizontal resistivity is higher than shale-base resistivity. This behavior further suggests absence of fully water-bearing formations.

4.2 FIELD CASE NO. 1: WELL α

This field case examines thinly bedded sand-shale sequences encountered in Well α. Figure 4.4 shows some of the well logs acquired in this well. Formation dip derived from Rt-Scanner measurements indicates values lower than 10 degrees. Negligible invasion effect was observed in apparent resistivity curves with different radial lengths of investigation, which indicates absence of mobile water pore volume in the formation. Shale is intrinsically anisotropic, and horizontal and vertical shale resistivities were identified from a representative shale interval where shale anisotropy equals 1.42.

The formation comprises thinly bedded sand-shale sequences, which is confirmed by the relatively large separation between horizontal and vertical resistivities, bimodal behavior of NMR *T2* distributions, resistivity image, and core photographs. Figure 4.3 shows photographs of core samples acquired from the depth intervals X137.8-X138.8 m and X143.3-X144.3 m, which confirm presence of an alternating sequence of sand and shale layers. In the laminated sections, X080-X090 m and X130-X140 m, electrical anisotropy ranges between 5 and 8, indicating presence of hydrocarbon-bearing, thinly bedded formations (Figure 4.5, track 5).

We applied electrical anisotropy analysis to estimate hydrocarbon reserves in the thinly bedded sand-shale sequence by assuming that isotropic sands are interbedded between shale layers. In addition, we observe low-porosity, high-resistivity streaks at a few depth intervals, which prompted us to invoke the high-resolution method for petrophysical evaluation of thin beds. Subsequently, results obtained with conventional petrophysical analysis, electrical anisotropy analysis, and high-resolution interpretation were compared with each other for validation.

Figure 4.5, track 5 compares horizontal, vertical, and sand resistivities. In non-laminated sands (depth interval X168-X172 m), sand resistivity equals vertical resistivity,

while in laminated sands (depth interval X130-X138 m), sand resistivity increases when compared to vertical resistivity. Such an increase in sand resistivity causes a decrease in the estimated water saturation in sand units.

Figure 4.5, track 8 compares laminar shale concentrations estimated with Thomas-Stieber's method and Rt-Scanner measurements. The two estimations are consistent with each other. Figure 4.5, track 9 shows the estimated dispersed shale concentration in sand units. Dispersed shale concentration ranges between 0 and 10% along most of the depth intervals, which is in good agreement with shale concentration estimated with XRD measurements.

Figure 4.5, track 10 describes the shoulder-bed corrected sand porosity and sand irreducible bulk volume. Shoulder-bed corrected porosity and permeability are in good agreement with core measurements. Figure 4.5, track 12 describes the sand petrophysical quality, indicating that sand units interbedded between shale layers (X078-X088 m) have good reservoir quality, comparable to that of clean thick sands.

Figure 4.6, track 10 compares non-shale water saturation calculated with conventional petrophysical analysis (dispersed shaly-sand equations) and anisotropy analysis. We observe that conventional petrophysical analysis underestimates hydrocarbon reserves in laminated sands when compared to those calculated with electrical anisotropy analysis. Also, water saturation estimated with anisotropy analysis is in close agreement with irreducible water saturation, indicating negligible mobile water pore volume (Figure 4.6, track 9). By contrast, conventional petrophysical analysis yields significant mobile water pore volume (Figure 4.6, track 8).

Figure 4.7 shows the distribution of total water saturation, Sw_t, hydrocarbon pore-thickness, *HPT*, sand permeability, K_{sd}, and sand reservoir quality, RQI, over the Thomas-Stieber crossplot. Figure 4.7-(a) shows that depth intervals with shale

concentration greater than 60% include total water saturation greater than 70%. It also shows that depth intervals with the lowest shale concentration and highest porosity exhibit the lowest water saturation. In Figure 4.7-(c) and (d), high permeability and good rock quality are observed along depth intervals with high sand porosity.

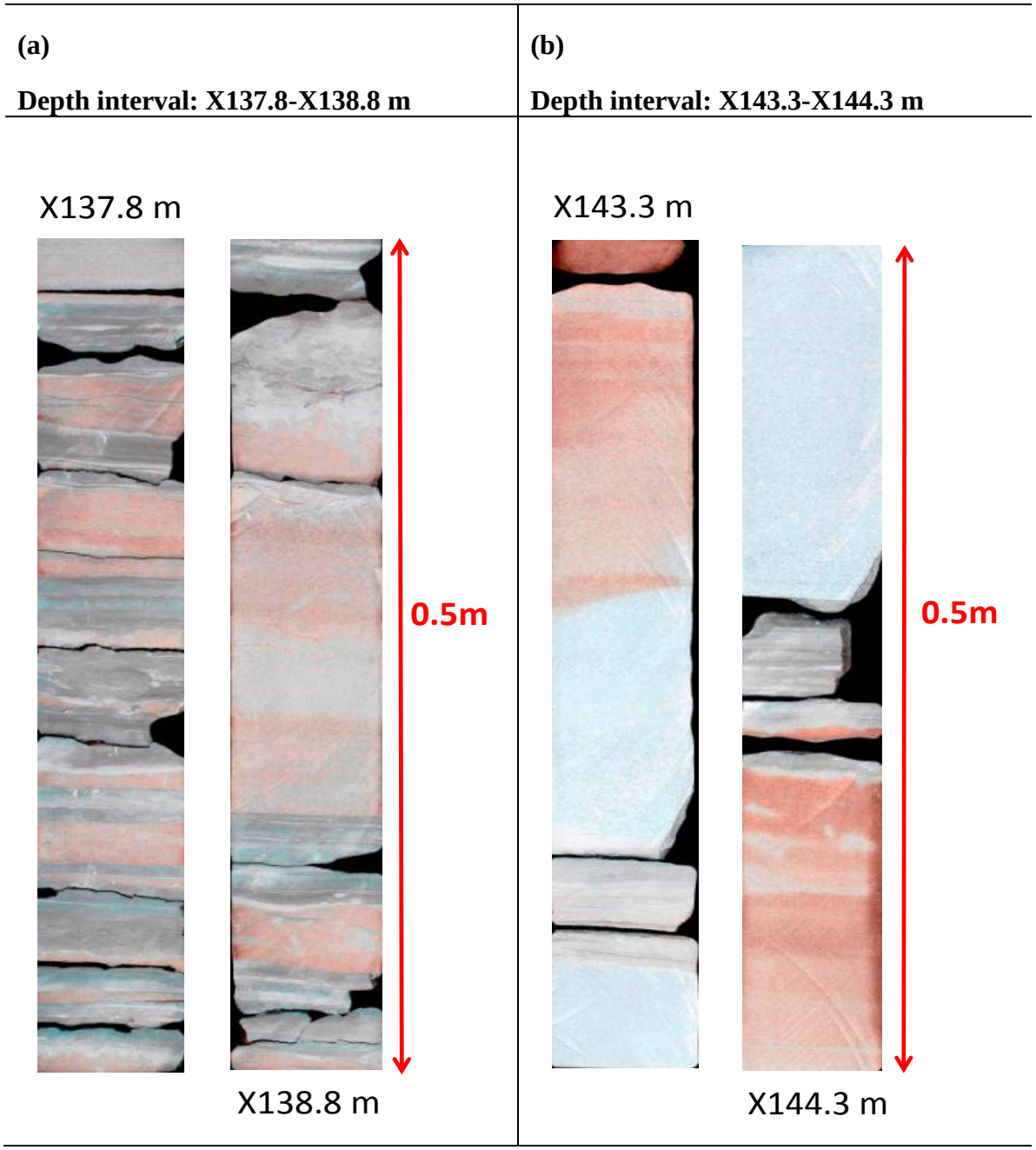

Figure 4.3: Core photographs acquired in the depth intervals X137.8-X138.8 m and X143.3-X144.3 m, Well α. (a) Core photographs evidencing a thinly bedded sand-shale sequence. Bed thickness ranges from a few inches to a few feet. (b) Core photographs evidencing heterogeneous formation with bed thickness smaller than one foot.

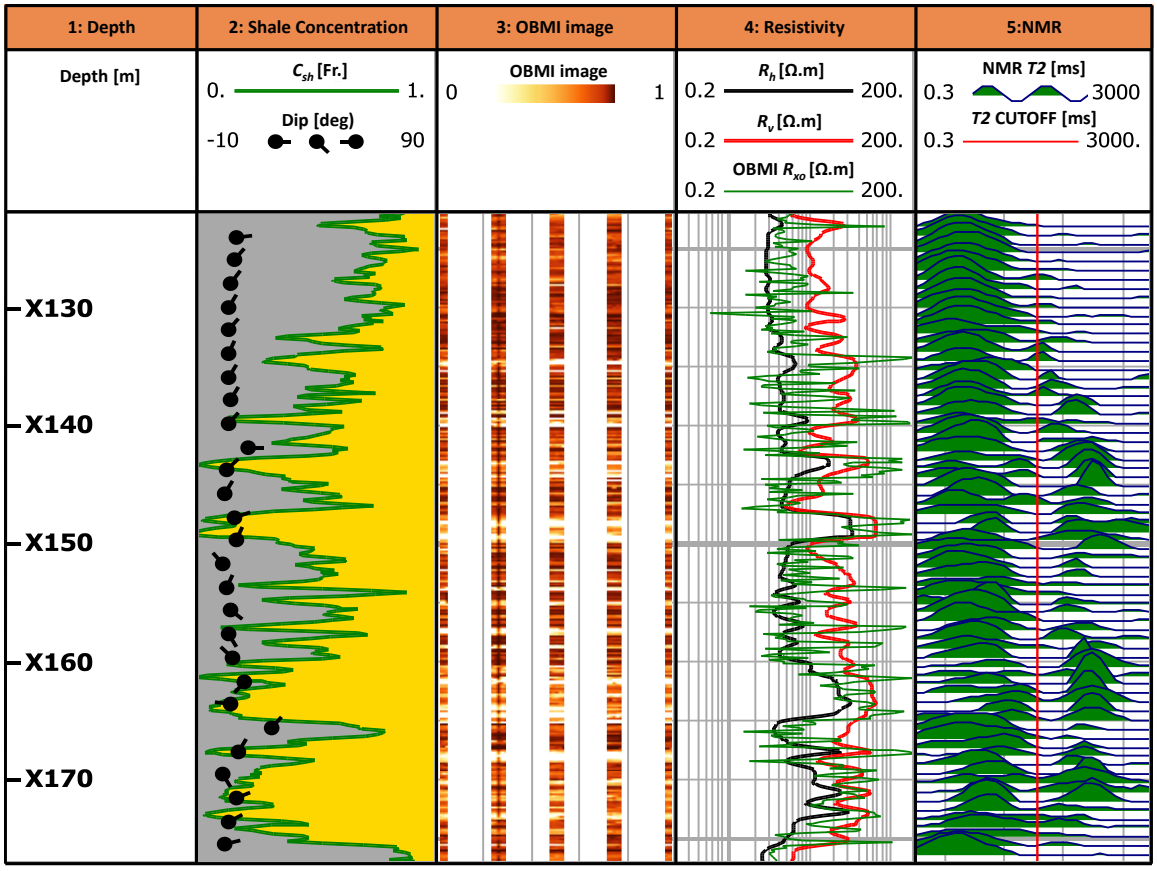

Figure 4.4: Comparison of horizontal, vertical, and OBMI resistivities. Track 1: depth. Track 2: volumetric shale concentration and formation dip. Track 3: OBMI image. Track 4: horizontal resistivity, vertical resistivity, and OBMI R_{xo} curve. Track 5: NMR *T2* distributions and *T2* cutoff.

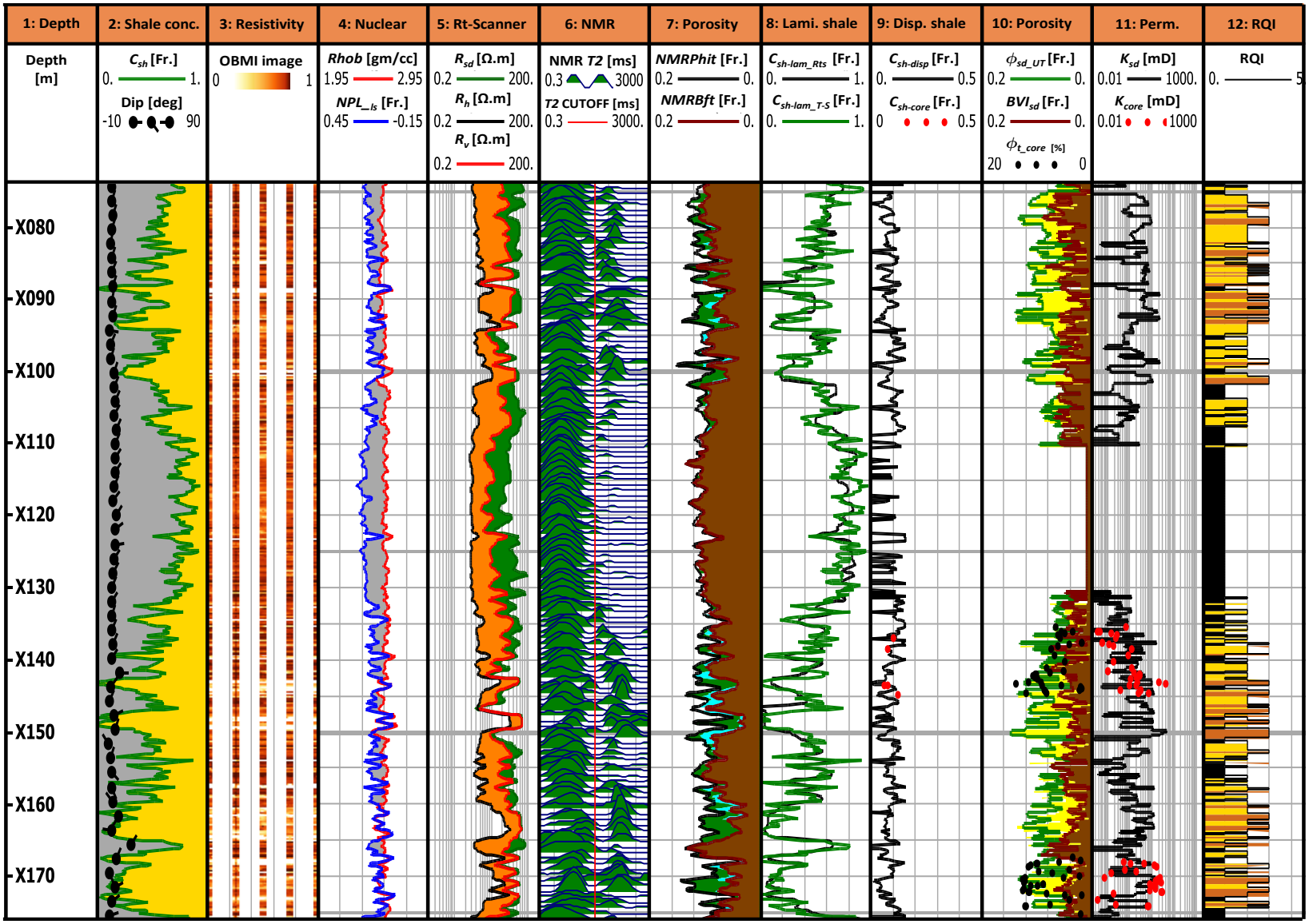
1: Depth
2: Shale conc.
3: Resistivity
4: Nuclear
5: Rt-Scanner
6: NMR
7: Porosity
8: Lami. shale
9: Disp. shale
10: Porosity
11: Perm.
12: RQI
Depth [m]
C_{sh} [Fr.]
0. 1.
Dip [deg]
-10 90
OBMI image
0 1
Rhob [gm/cc]
1.95 2.95
NPL_ls [Fr.]
0.45 -0.15
R_{sd} [Ω.m]
0.2 200.
R_h [Ω.m]
0.2 200.
R_v [Ω.m]
0.2 200.
NMR *T2* [ms]
0.3 3000
T2 CUTOFF [ms]
0.3 3000.
NMRPhit [Fr.]
0.2 0.
NMRBft [Fr.]
0.2 0.
$C_{sh\text{-}lam\_Rts}$ [Fr.]
0. 1.
$C_{sh\text{-}lam\_T\text{-}S}$ [Fr.]
0. 1.
$C_{sh\text{-}disp}$ [Fr.]
0. 0.5
$C_{sh\text{-}core}$ [Fr.]
0 0.5
ϕ_{sd_UT} [Fr.]
0.2 0.
BVI$_{sd}$ [Fr.]
0.2 0.
ϕ_{t_core} [%]
20 0
K_{sd} [mD]
0.01 1000.
K_{core} [mD]
0.01 1000
RQI
0. 5
X080
X090
X100
X110
X120
X130
X140
X150
X160
X170

Figure 4.5: Results obtained from anisotropy analysis in Well α. Track 1: depth. Track 2: volumetric shale concentration and formation dip. Track 3: OBMI image. Track 4: bulk density and neutron (limestone matrix) log. Track 5: sand, horizontal, and vertical resistivity. Track 6: NMR *T2* distributions. Track 7: NMR total porosity and bound fluid. Track 8: volumetric laminar shale concentrations from Rt-Scanner measurements and Thomas-Stieber's method. Track 9: volumetric dispersed shale concentration in sand units and volumetric shale concentration estimated from core measurements. Track 10: shoulder-bed corrected sand porosity, sand irreducible bulk volume, and core porosity. Track 11: sand and core permeability. Track 12: sand reservoir quality.

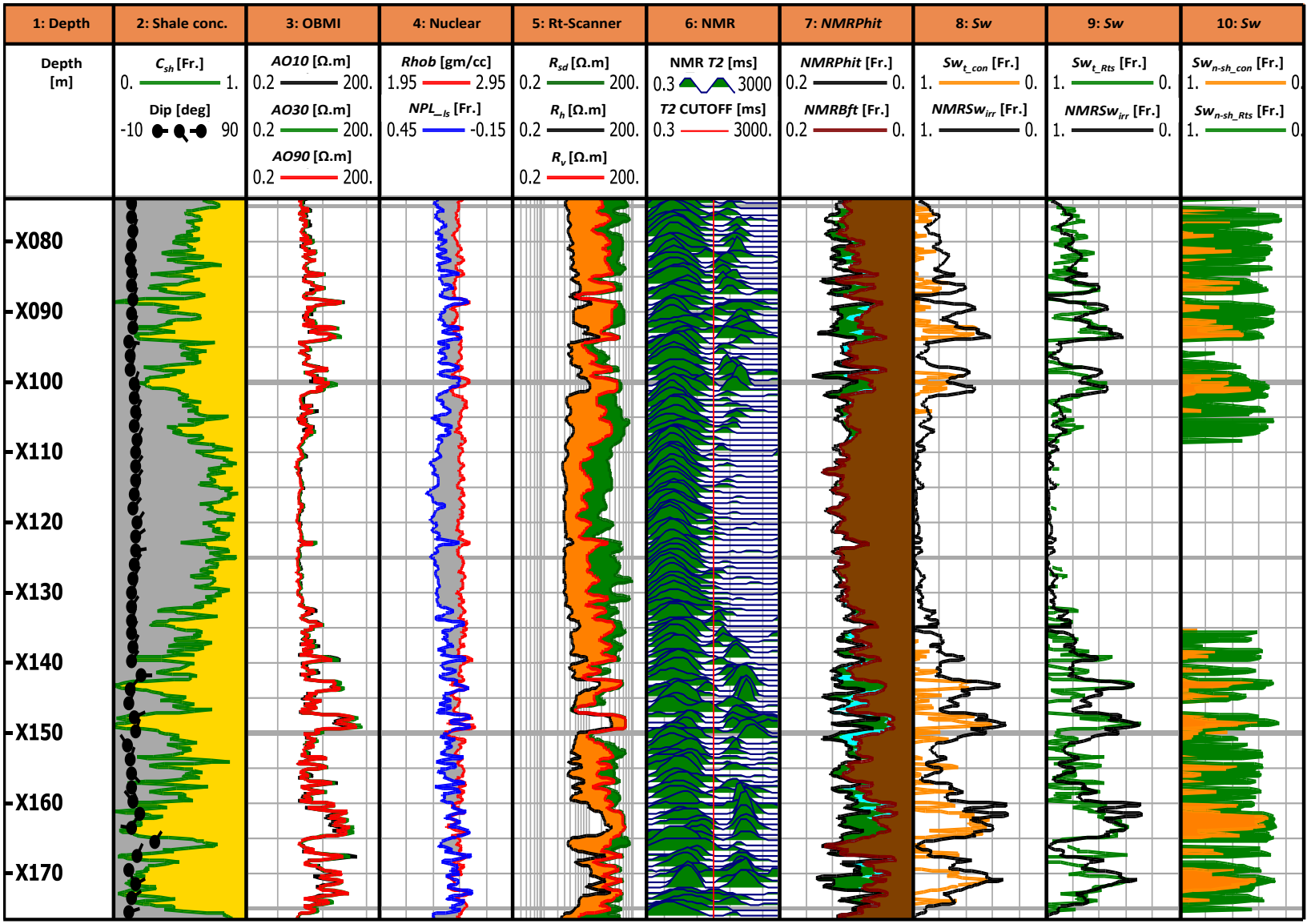
1: Depth
2: Shale conc.
3: OBMI
4: Nuclear
5: Rt-Scanner
6: NMR
7: NMRPhit
8: Sw
9: Sw
10: Sw
Depth [m]
Csh [Fr.] 0. 1.
Dip [deg] -10 90
AO10 [Ω.m] 0.2 200.
AO30 [Ω.m] 0.2 200.
AO90 [Ω.m] 0.2 200.
Rhob [gm/cc] 1.95 2.95
NPL_ls [Fr.] 0.45 -0.15
Rsd [Ω.m] 0.2 200.
Rh [Ω.m] 0.2 200.
Rv [Ω.m] 0.2 200.
NMR T2 [ms] 0.3 3000
T2 CUTOFF [ms] 0.3 3000.
NMRPhit [Fr.] 0.2 0.
NMRBft [Fr.] 0.2 0.
Swt_con [Fr.] 1. 0.
NMRSwirr [Fr.] 1. 0.
Swt_Rts [Fr.] 1. 0.
NMRSwirr [Fr.] 1. 0.
Swn-sh_con [Fr.] 1. 0.
Swn-sh_Rts [Fr.] 1. 0.
X080
X090
X100
X110
X120
X130
X140
X150
X160
X170

Figure 4.6: Results obtained from anisotropy analysis in Well α. Track 1: depth. Track 2: volumetric shale concentration and formation dip. Track 3: apparent resistivity curves with different radial lengths of investigation. Track 4: bulk density and neutron (limestone matrix) log. Track 5: sand, horizontal, and vertical resistivity. Track 6: NMR *T2* distributions. Track 7: NMR total porosity and bound-fluid. Track 8: total water saturation calculated with conventional petrophysical analysis and irreducible water saturation. Track 9: total water saturation calculated with anisotropy analysis and irreducible water saturation. Track 10: non-shale water saturation calculated with anisotropy analysis and conventional petrophysical analysis.

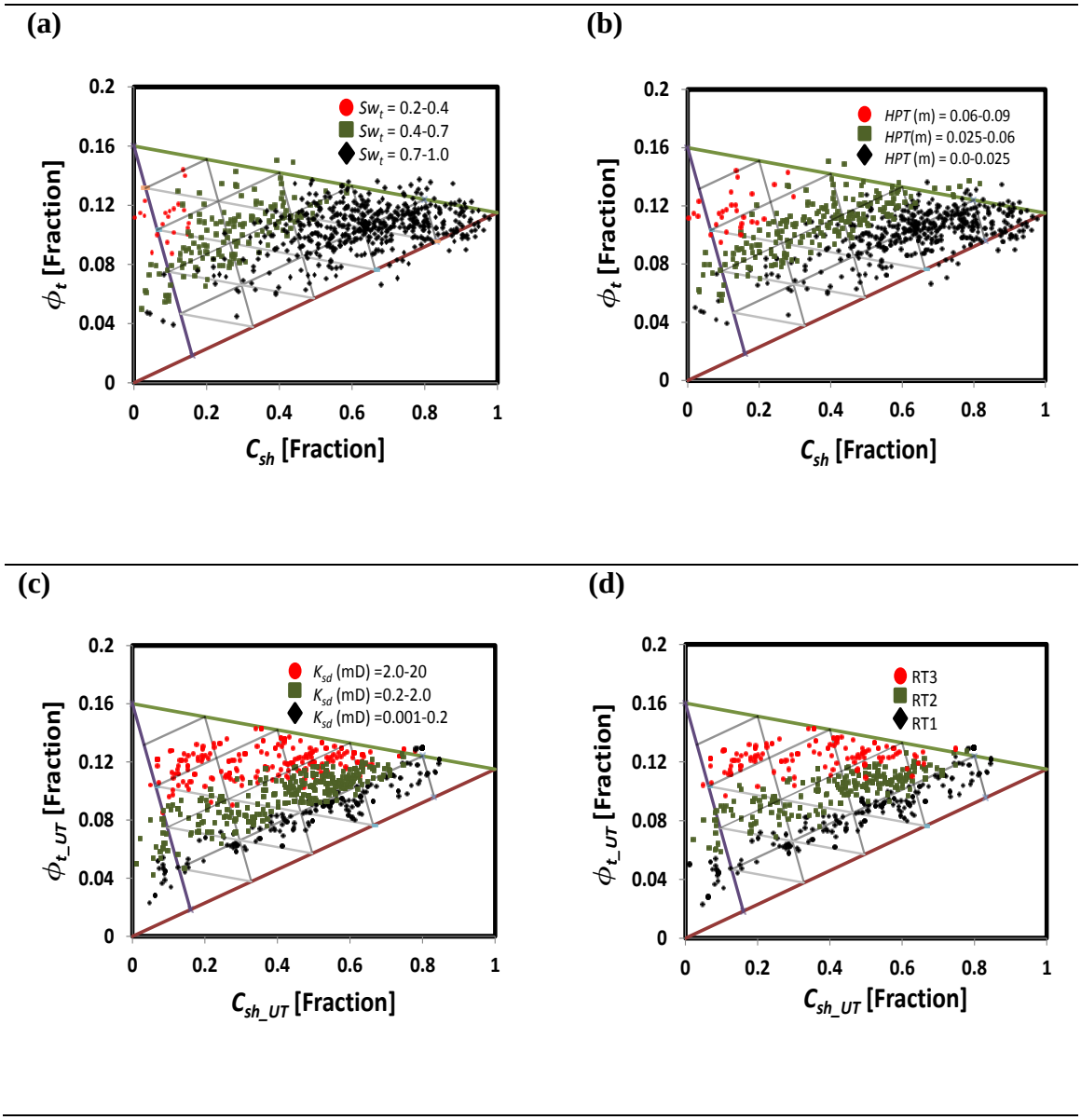

Figure 4.7**:** Thomas-Stieber total shale concentration versus total porosity crossplot, emphasizing the distribution of (a) total water saturation, (b) hydrocarbon pore thickness, (c) permeability, and (d) sand reservoir quality index (RQI), in Well α, depth interval X070-X175 m.

\

4.2.1 High-Resolution Interpretation Method, Well α

The high-resolution interpretation method was implemented in wells where resistivity images and/or core images were available. Figure 4.8 shows some of the acquired well logs in Well α together with the results obtained with the high-resolution method. The assumed model included a stacked sequence of sand and shale layers, where sand layers can comprise dispersed shale (Figure 4.8, track 2). Bed boundaries were detected at inflection points of the OBMI R_{xo} curve (Figure 4.8, track 6). Table 4.2, Well α summarizes the parameters assumed in the numerical simulations.

Figure 4.8, track 7 compares the OBMI R_{xo} curve to core image data. OBMI measurements responded to most of the lithofacies visible on core images yielded averaged responses of adjacent beds when beds are thinner than their vertical resolution. In many such cases, beds are left unidentified by OBMI measurements, which still remain visible on core images. In order to compensate for beds unrecognized by OBMI measurements, a few additional beds were added into the model (for example, at depth XX43.2 m).

Figure 4.8**,** tracks 2, 3, and 4 compare field and numerically simulated well logs. An excellent agreement is reached between field and numerically simulated logs. The averaging effect of alternating thin beds of sand and shale layers is clearly observed on resistivity and nuclear logs. In thinly bedded formations (for example, depth interval XX38-XX39 m), horizontal resistivity is only 1-3 ohm-m higher than shale base resistivity. This behavior is due to the high electrical conductivity effect of laminar shale on horizontal resistivity.

Total porosity determined with the high-resolution interpretation method was consistent with core measurements **(**Figure 4.8**,** track 4**)**. Also, on average, sand layers included 8-10% shale concentration, which was consistent with shale concentration

estimated with XRD measurements, thereby validating the distribution of shale concentration.

Figure 4.8, track 9 describes water saturation calculated with the high-resolution interpretation method. At the depth intervals XX38-XX39 m and XX41.8-XX42 m, sand units interbedded between shale layers exhibit relatively low water saturation, in the range of 30-50%. At the same depth interval, NMR measurements exhibit bimodal *T2* distributions. These observations indicate presence of good sand reservoir quality beds interbedded with shale layers.

Figure 4.9, track 7 compares water saturation estimated with conventional petrophysical analysis (dispersed shaly-sand models) and the high-resolution interpretation method. In non-laminated sands, water saturations estimated with both methods are in good agreement; however, in laminated sands conventional petrophysical analysis overestimates water saturation when compared to water saturation estimated with the high-resolution interpretation method. In order to properly compare results, water saturation calculated with the high-resolution interpretation method was smoothed with an averaging filter of length equal to 2 ft.

Figure 4.9, track 5 compares sand resistivity obtained with Rt-Scanner measurements to that calculated with the high-resolution interpretation method. Along the depth intervals XX36-XX37.2 m, XX38-XX39.2 m, XX40-XX41.2 m, and XX41.5 – XX42.6 m, sand resistivity values determined with the high-resolution interpretation method and Rt-Scanner measurements are in good agreement.

At the depth intervals XX39.2-XX39.8 m and XX43.3-XX43.6 m, sand resistivity estimated with electrical anisotropy analysis exhibits larger values than those obtained with the high-resolution interpretation method. Consequently, at these depth intervals, electrical anisotropy analysis gives rise to lower values of water saturation compared to

water saturation obtained with the high-resolution interpretation method (Figure 4.9, track 9). We observe alternate sequences of low-porosity, high-resistivity rocks and high-porosity hydrocarbon-bearing formations (Figure 4.3-b) at these depth intervals. Electrical anisotropy estimated with Rt-Scanner measurements is suspected to partially originate from alternating beds of low-porosity, high-resistivity rocks and high-porosity hydrocarbon-bearing formations, which gives rise to overestimation of hydrocarbon reserves.

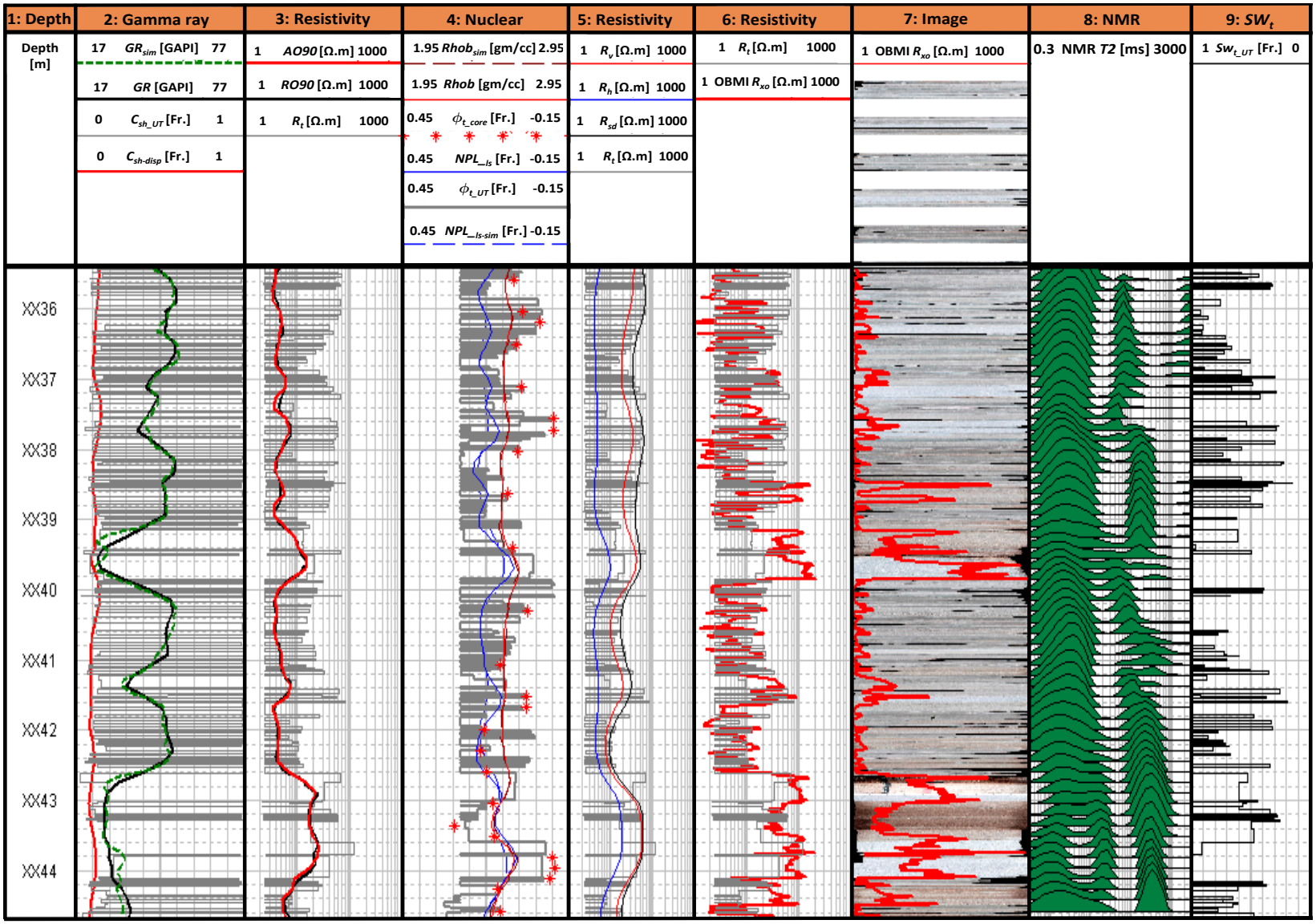
1: Depth
2: Gamma ray
3: Resistivity
4: Nuclear
5: Resistivity
6: Resistivity
7: Image
8: NMR
9: SW_t
Depth [m]
17 GR_{sim} [GAPI] 77
17 GR [GAPI] 77
0 C_{sh_UT} [Fr.] 1
0 $C_{sh\text{-}disp}$ [Fr.] 1
1 $AO90$ [Ω.m] 1000
1 $RO90$ [Ω.m] 1000
1 R_t [Ω.m] 1000
1.95 $Rhob_{sim}$ [gm/cc] 2.95
1.95 $Rhob$ [gm/cc] 2.95
0.45 ϕ_{t_core} [Fr.] -0.15
0.45 NPL_{ls} [Fr.] -0.15
0.45 ϕ_{t_UT} [Fr.] -0.15
0.45 $NPL\_{ls\text{-}sim}$ [Fr.] -0.15
1 R_v [Ω.m] 1000
1 R_h [Ω.m] 1000
1 R_{sd} [Ω.m] 1000
1 R_t [Ω.m] 1000
1 R_t [Ω.m] 1000
1 OBMI R_{xo} [Ω.m] 1000
1 OBMI R_{xo} [Ω.m] 1000
0.3 NMR $T2$ [ms] 3000
1 Sw_{t_UT} [Fr.] 0
XX36
XX37
XX38
XX39
XX40
XX41
XX42
XX43
XX44

Figure 4.8: Results obtained with the high-resolution interpretation method for the petrophysical evaluation of thinly bedded formations. Dashed curves identify numerically simulated logs while solid curves indicate field logs. Track 1: depth. Track 2: numerically simulated gamma-ray, field gamma-ray, shoulder-bed corrected shale concentration, and volumetric dispersed shale concentration. Track 3: deep resistivity, numerically simulated deep resistivity, and true bed resistivity. Track 4: numerically simulated density log, field bulk density log, core porosity, field neutron (limestone matrix) porosity log, shoulder-bed corrected porosity, and numerically simulated neutron (limestone matrix) porosity log. Track 5: vertical, horizontal, sand, and true bed resistivity. Track 6: true bed resistivity and OBMI R_{xo} curve. Track 7: core image and OBMI R_{xo} curve. Track 8: NMR *T2* distributions. Track 9: shoulder-bed corrected water saturation.

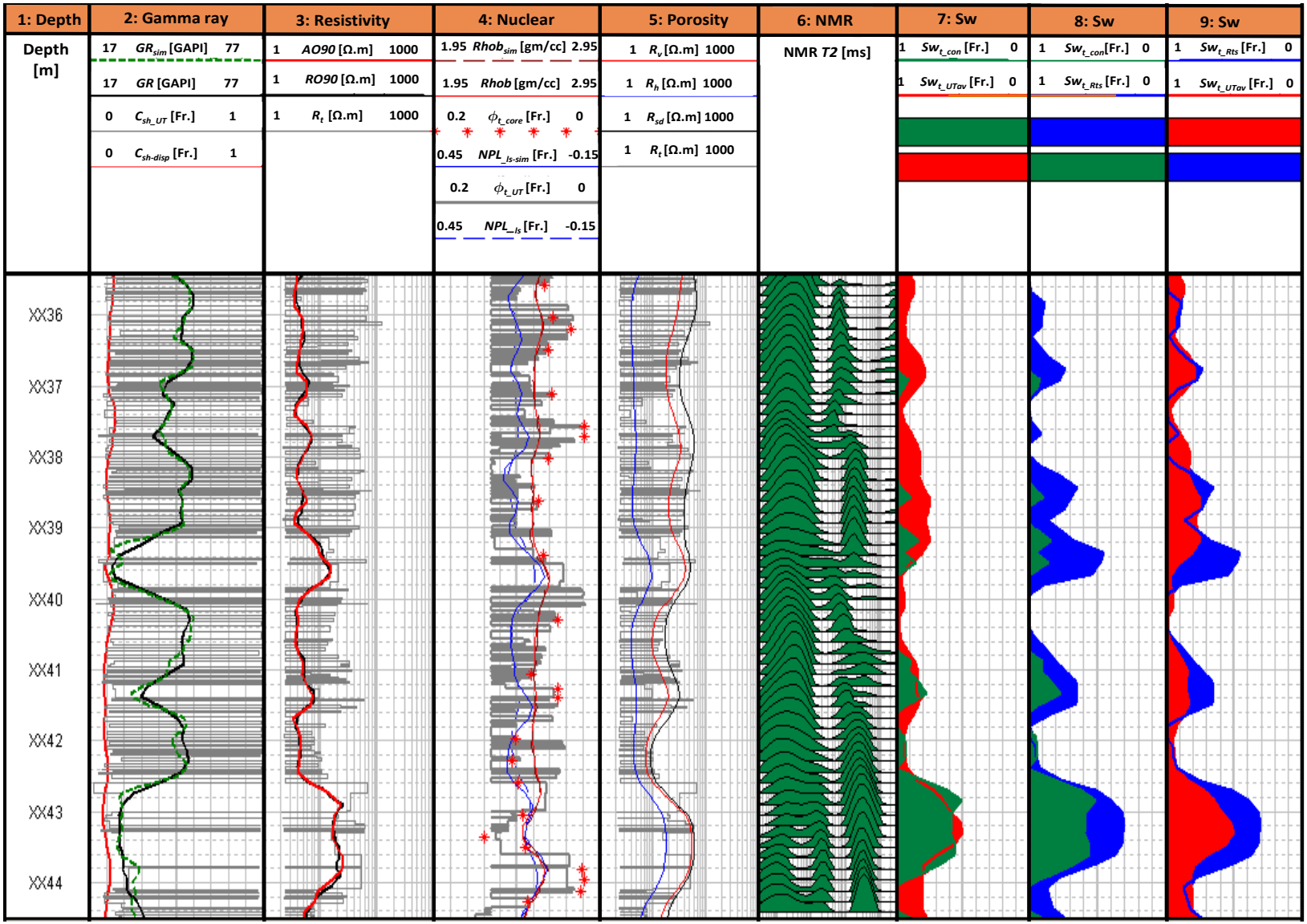
1: Depth
2: Gamma ray
3: Resistivity
4: Nuclear
5: Porosity
6: NMR
7: Sw
8: Sw
9: Sw
Depth [m]
17 GR_sim [GAPI] 77
17 GR [GAPI] 77
0 C_sh_UT [Fr.] 1
0 C_sh-disp [Fr.] 1
1 AO90 [Ω.m] 1000
1 RO90 [Ω.m] 1000
1 R_t [Ω.m] 1000
1.95 Rhob_sim [gm/cc] 2.95
1.95 Rhob [gm/cc] 2.95
0.2 φ_t_core [Fr.] 0
0.45 NPL_ls-sim [Fr.] -0.15
0.2 φ_t_UT [Fr.] 0
0.45 NPL_ls [Fr.] -0.15
1 R_v [Ω.m] 1000
1 R_h [Ω.m] 1000
1 R_sd [Ω.m] 1000
1 R_t [Ω.m] 1000
NMR T2 [ms]
1 Sw_t_con [Fr.] 0
1 Sw_t_UTav [Fr.] 0
1 Sw_t_con [Fr.] 0
1 Sw_t_Rts [Fr.] 0
1 Sw_t_Rts [Fr.] 0
1 Sw_t_UTav [Fr.] 0
XX36
XX37
XX38
XX39
XX40
XX41
XX42
XX43
XX44

Figure 4.9: Results obtained with the high-resolution interpretation method for the petrophysical evaluation of thinly bedded formations. Dashed curves identify numerically simulated logs while solid curves indicate field logs. Track 1: depth. Track 2: numerically simulated gamma-ray, field gamma-ray, shoulder-bed corrected shale concentration, and volumetric dispersed shale concentration. Track 3: deep resistivity, numerically simulated deep resistivity, and true bed resistivity. Track 4: numerically simulated density log, field bulk density log, core porosity, field neutron (limestone matrix) porosity log, shoulder-bed corrected porosity, and numerically simulated neutron (limestone matrix) porosity log. Track 5: vertical, horizontal, sand, and true bed resistivity. Track 6: NMR *T2* distributions. Track 7: water saturation estimated with conventional petrophysical analysis and the high-resolution interpretation method. Track 8: water saturation estimated with conventional petrophysical analysis and electrical anisotropy analysis. Track 9: water saturation estimated with the high-resolution interpretation method and electrical anisotropy analysis.

Petrophysical properties determined with anisotropy analysis were validated by performing numerical simulations of NMR *T2* distributions at depth X172 m. Figure 4.10 describes sand, shale, averaged, and field NMR *T2* distributions. Field and numerically simulated NMR *T2* distributions are in good agreement. A tri-modal *T2* distribution was obtained due to amalgamation of sand and shale layers. Table 4.3 summarizes the input parameters necessary to obtain a good agreement between field and numerically simulated logs. Numerical simulations indicate values of irreducible water saturation and oil saturation of 40% and 60%, respectively, in sand units. In addition, numerical simulations confirmed that NMR *T2* peaks at 200 ms, 15 ms, and 2 ms were due to oil, capillary-bound water, and clay-bound water, respectively. Petrophysical properties determined with NMR numerical simulations and anisotropy analysis were in good agreement. Moreover, the *T2* bulk of oil used in the simulations was 300 ms, indicating presence of high-viscosity oil in the formation.

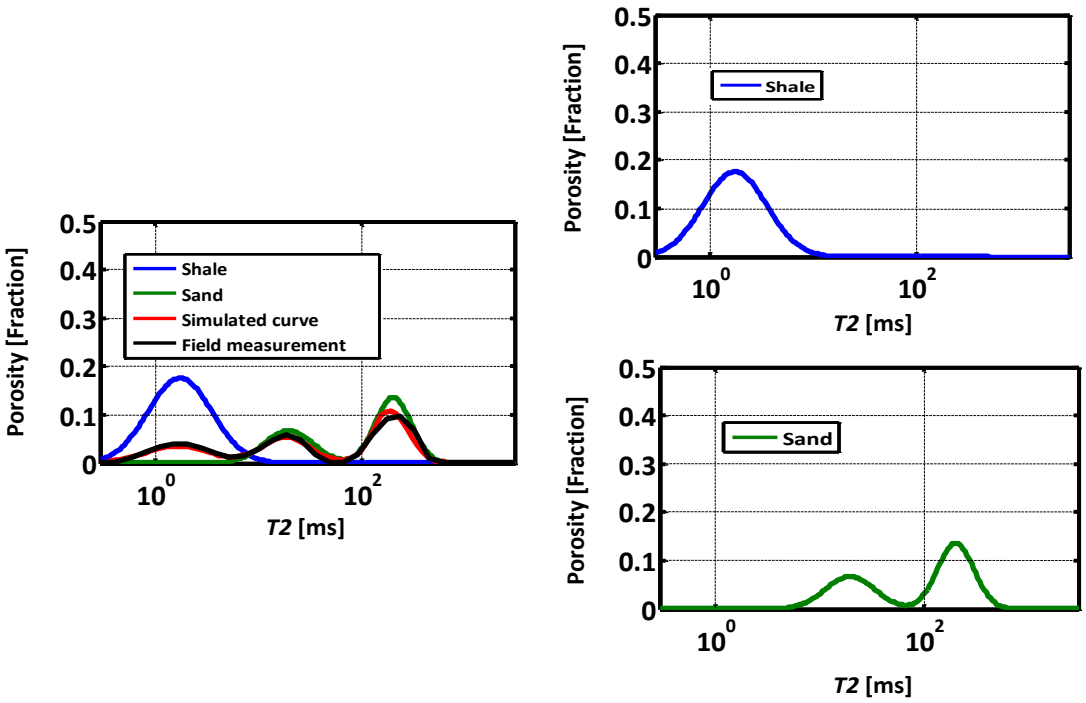

Figure 4.10: Results obtained from the numerical simulations of NMR *T2* distributions at depth X172 m, Well α. An excellent agreement is achieved between field and numerically simulated *T2* distributions. Table 4.3 describes the parameters assumed in the simulations.

Petrophysical Property	Value	Units
Sw_{sh}	1	[Fraction]
Sw_{sd_irr}	0.4	[Fraction]
Shc_{sd}	0.6	[Fraction]
$C_{sh\text{-}lam}$	0.2	[Fraction]
$T2_{bulk\_oil}$	300	[ms]
$T2_{bulk\_wr}$	2000	[ms]

Table 4.3: Parameters assumed in the numerical simulation of NMR *T2* distributions at depth X172 m, Well α. Figure 4.10 shows the results obtained from numerical simulations.

4.3 FIELD CASE NO. 2: WELL β

This field example focuses on the petrophysical interpretation of a low-resistivity, low-contrast zone (LRLC) encountered in Well β. Figure 4.11 describes the well logs acquired in this well. Formation dip derived from Rt-Scanner measurements indicates values lower than 10 degrees. Negligible invasion effects were observed in apparent resistivity curves with different radial lengths of investigation; OBMI measurements and core images were not available for this well.

Figure 4.11, track 8 compares laminar shale concentrations derived with Rt-Scanner measurements and Thomas-Stieber's method. Results agree well along most of the depth intervals, thereby confirming the validity of the tensor resistivity model.

The depth interval X070-X080 m is a low-resistivity, low-contrast zone (LRLC). Shale concentration is approximately 65% and horizontal resistivity is only 1 to 2 ohm-m higher than shale base resistivity. Well logs and core measurements indicate several reasons for such low apparent resistivity values; X-ray diffraction acquired in several wells within the studied reservoir indicates presence of dispersed clay, including illite, smectite, chlorite, and kaolinite, in the formation. Smectite and illite have high cation exchange capacity, ranging between 40 and 150 milliequivalents per 100 grams, which can cause apparent resistivity values to decrease significantly. In addition, Rt-Scanner measurements exhibit high electrical anisotropy, varying between 4 and 7, thereby indicating presence of thinly bedded sand-shale sequences. The high electrical conductivity of laminar shale further reduces apparent resistivity values. Moreover, NMR measurements exhibit bimodal behavior of NMR *T2* distributions with *T2* peaks at times greater than 100 ms. High anisotropy values and *T2* peaks at times greater than 100 ms, suggest the presence of hydrocarbon-bearing, thinly bedded formations.

Figure 4.11, tracks 10 and 11 show shoulder-bed corrected porosity, sand irreducible bulk volume, and sand permeability. Shoulder-bed corrected porosity and permeability agree well with core measurements. Figure 4.11, track 12 describes the reservoir quality of sand units. Along the depth interval X072-X080 m, sand units interbedded with shale layers have good sand reservoir quality, similar to that of clean thick sands.

Figure 4.12, track 8 compares total water saturation estimated with conventional petrophysical analysis and irreducible water saturation. Along the depth interval X072-X080 m, conventional petrophysical analysis yields significant values of mobile water pore volume. However, water saturation estimated with electrical anisotropy analysis yields a closer agreement with irreducible water saturation (Figure 4.12, track 9). Figure 4.12, track 10 compares non-shale water saturation estimated with both conventional petrophysical analysis and electrical anisotropy analysis. An improvement in hydrocarbon reserves is obtained with electrical anisotropy analysis compared to those obtained with conventional petrophysical analysis.

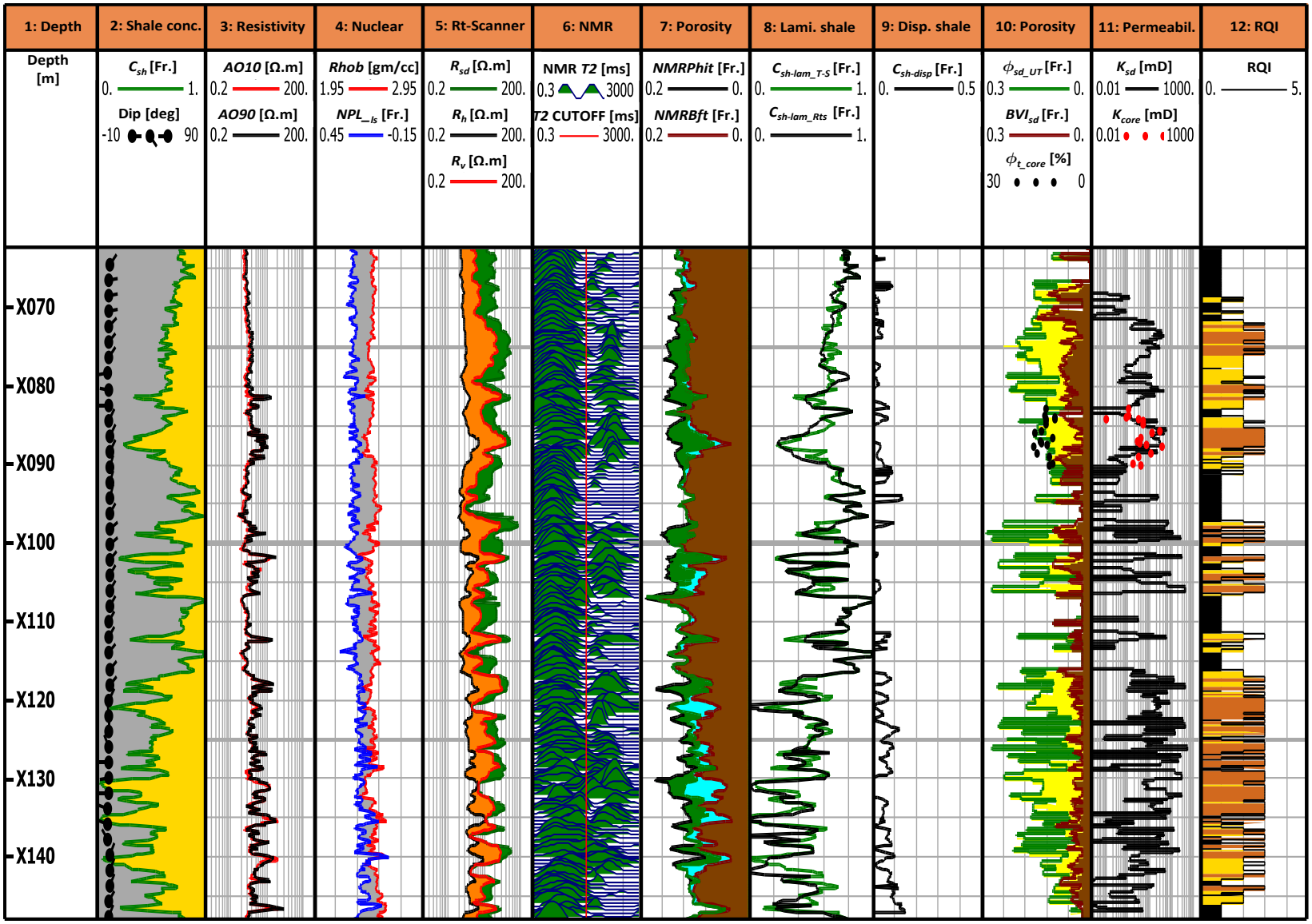
1: Depth
2: Shale conc.
3: Resistivity
4: Nuclear
5: Rt-Scanner
6: NMR
7: Porosity
8: Lami. shale
9: Disp. shale
10: Porosity
11: Permeabil.
12: RQI
Depth [m]
C_{sh} [Fr.]
0. 1.
Dip [deg]
-10 90
AO10 [Ω.m]
0.2 200.
AO90 [Ω.m]
0.2 200.
Rhob [gm/cc]
1.95 2.95
$NPL_{\_ls}$ [Fr.]
0.45 -0.15
R_{sd} [Ω.m]
0.2 200.
R_h [Ω.m]
0.2 200.
R_v [Ω.m]
0.2 200.
NMR T2 [ms]
0.3 3000
T2 CUTOFF [ms]
0.3 3000.
NMRPhit [Fr.]
0.2 0.
NMRBft [Fr.]
0.2 0.
$C_{sh\text{-}lam\_T\text{-}S}$ [Fr.]
0. 1.
$C_{sh\text{-}lam\_Rts}$ [Fr.]
0. 1.
$C_{sh\text{-}disp}$ [Fr.]
0. 0.5
ϕ_{sd_UT} [Fr.]
0.3 0.
BVI_{sd} [Fr.]
0.3 0.
ϕ_{t_core} [%]
30 0
K_{sd} [mD]
0.01 1000.
K_{core} [mD]
0.01 1000
RQI
0. 5.
X070
X080
X090
X100
X110
X120
X130
X140

Figure 4.11: Results obtained from anisotropy analysis in Well β. Track 1: depth. Track 2: volumetric shale concentration and formation dip. Track 3: apparent resistivity curves with different radial lengths of investigation. Track 4: bulk density and neutron (limestone matrix) log. Track 5: sand, horizontal, and vertical resistivity. Track 6: NMR *T2* distributions. Track 7: NMR total porosity and bound fluid. Track 8: volumetric laminar shale concentrations estimated with Rt-Scanner measurements and Thomas-Stieber's method. Track 9: volumetric dispersed shale concentration in the sand layers. Track 10: shoulder-bed corrected sand porosity, sand irreducible bulk volume, and core porosity. Track 11: sand and core permeability. Track 12: sand reservoir quality.

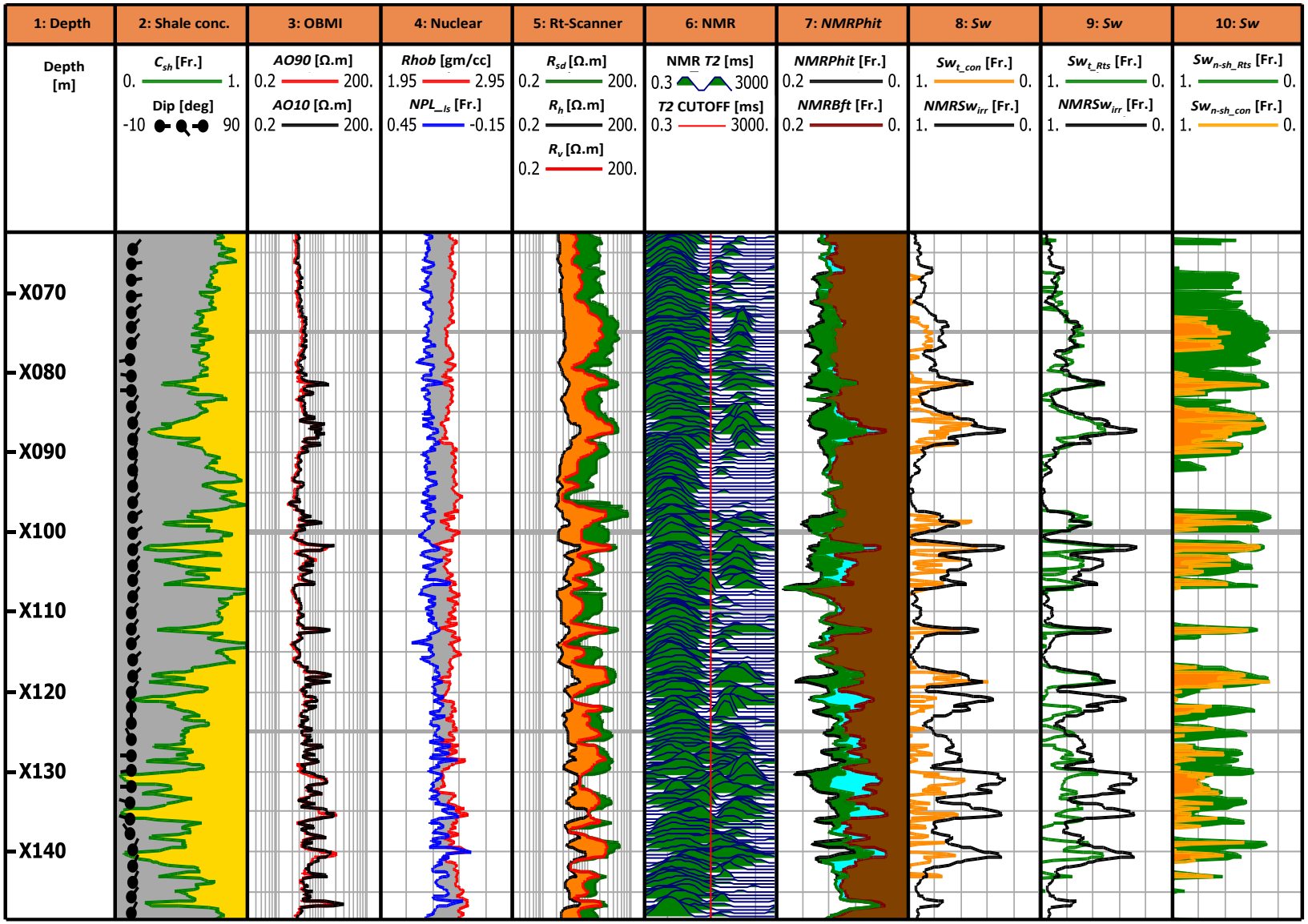
1: Depth
2: Shale conc.
3: OBMI
4: Nuclear
5: Rt-Scanner
6: NMR
7: NMRPhit
8: Sw
9: Sw
10: Sw
Depth [m]
Csh [Fr.] 0. 1.
Dip [deg] -10 90
AO90 [Ω.m] 0.2 200.
AO10 [Ω.m] 0.2 200.
Rhob [gm/cc] 1.95 2.95
NPL_ls [Fr.] 0.45 -0.15
Rsd [Ω.m] 0.2 200.
Rh [Ω.m] 0.2 200.
Rv [Ω.m] 0.2 200.
NMR T2 [ms] 0.3 3000
T2 CUTOFF [ms] 0.3 3000.
NMRPhit [Fr.] 0.2 0.
NMRBft [Fr.] 0.2 0.
Swt_con [Fr.] 1. 0.
NMRSwirr [Fr.] 1. 0.
Swt_Rts [Fr.] 1. 0.
NMRSwirr [Fr.] 1. 0.
Swn-sh_Rts [Fr.] 1. 0.
Swn-sh_con [Fr.] 1. 0.
X070
X080
X090
X100
X110
X120
X130
X140

Figure 4.12: Results obtained from anisotropy analysis in Well β. Track 1: depth. Track 2: volumetric shale concentration and formation dip. Track 3: apparent resistivity curves with different radial lengths of investigation. Track 4: bulk density and neutron (limestone matrix) log. Track 5: sand, horizontal, and vertical resistivity. Track 6: NMR *T2* distributions. Track 7: NMR total porosity and bound fluid. Track 8: total water saturation from conventional petrophysical analysis and irreducible water saturation. Track 9: total water saturation from anisotropy analysis and irreducible water saturation. Track 10: non-shale water saturation from anisotropy analysis and conventional petrophysical analysis.

Figure 4.13 shows results obtained from numerical simulations of NMR *T2* distributions at depth X075 m. Field and numerically simulated NMR *T2* distributions are in good agreement. Table 4.4 summarizes the parameters used in the numerical simulations of NMR *T2* distributions. Numerical simulations indicate absence of mobile water pore volume and relatively large saturation of clay- and capillary-bound water. In addition, NMR numerical simulations indicate that sand units interbedded between shale layers exhibit good reservoir quality and, if produced, will most likely yield hydrocarbon with negligible water efflux. Results obtained from NMR numerical simulations were consistent with those obtained with anisotropy analysis. The *T2* bulk of oil assumed in the simulations was 300 ms, which indicates presence of high-viscosity oil in the formation.

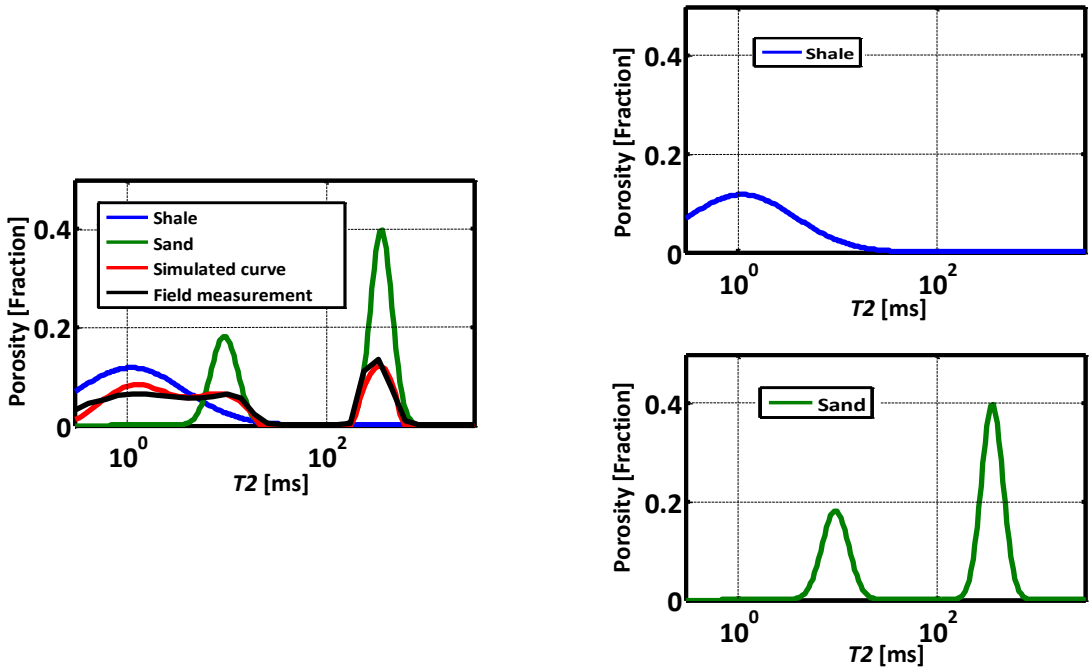

Figure 4.13: Results obtained from numerical simulations of NMR *T2* distributions at depth X075 m, Well β. An excellent agreement is achieved between field and numerically simulated *T2* distributions; NMR numerical simulations indicate good sand reservoir units interbedded between shale layers. Table 4.4 summarizes the parameters assumed in the simulations.

Petrophysical Properties	**Values**	**Units**
Sw_{sh}	1	[Fraction]
Sw_{sd_irr}	0.36	[Fraction]
Shc_{sd}	0.64	[Fraction]
$C_{sh\text{-}lam}$	0.65	[Fraction]
$T2_{bulk\_oil}$	300	[ms]
$T2_{bulk\_wr}$	2000	[ms]

Table 4.4: Parameters assumed in the numerical simulation of NMR *T2* distributions at depth X075 m, Well β. Figure 4.13 shows the corresponding numerical simulations.

4.4 FIELD CASE NO. 3: WELL γ

This section of the reservoir comprises an ideal Bouma sequence (Figure 4.14) with clean thick sands at the bottom and a thinly bedded sand-shale sequence at the top (Figure 4.15). Formation dip derived from Rt-Scanner measurements is lower than 10 degrees. A capillary pressure transition zone is observed with low and high resistivity values at the bottom and at the top, respectively.

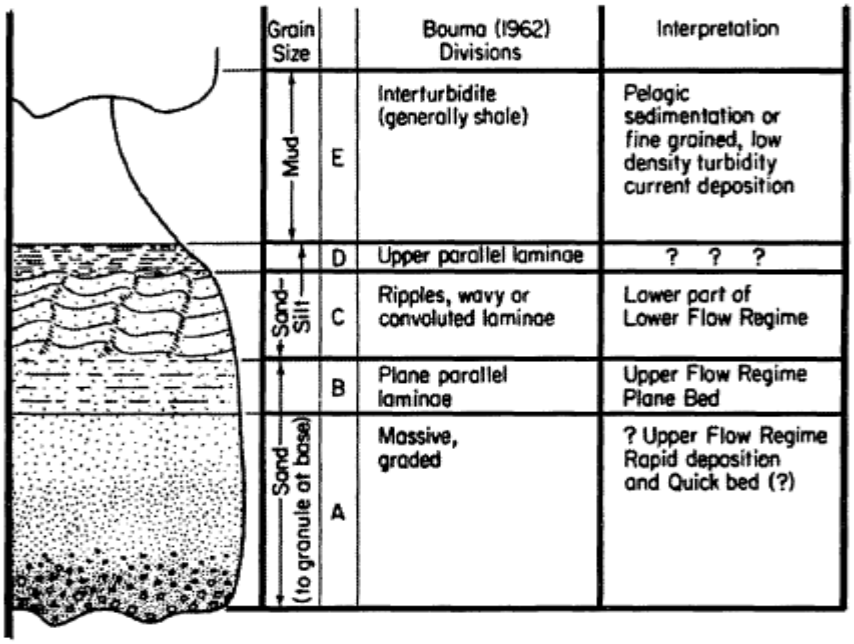

Figure 4.14: Idealized depositional units (Bouma sequence) of a classic turbidite sequence (Mollison et al., 2001).

The Thomas-Stieber crossplot for this section of the reservoir (Figure 4.1, Well γ) indicates that the formation is mainly composed of laminar shale with a limited amount of dispersed shale. OBMI measurements, core laboratory measurements, and core images were not available in this section of the reservoir.

Between the depth intervals X147-X149 m and X150-X152 m (Figure 4.15, track 5), horizontal and vertical resistivities overlap thereby indicating presence of electrically isotropic rock formations. This electrically isotropic behavior of rocks suggests absence of laminar shale and/or high water saturation. Klein et al. (1997) showed that electrical anisotropy could be affected by variations of fluid saturations. They observed lower electrical anisotropy at high values of water saturation.

Along the depth interval X152-X157 m, electrical anisotropy ranges between 1.5 and 2.2 (Figure 4.15, track 5**)**. Along the same depth interval, volumetric laminar shale concentration estimated with the tensor resistivity model varies between 30 and 50%, which is significantly larger than laminar shale concentration obtained with Thomas-Stieber's method (0-5%). This discrepancy between the two calculations of laminar shale concentration suggests that the electrical anisotropic nature of the formation is not due to the presence of laminar shale. We suspect that this electrical anisotropy originates from the presence of graded beds. Such graded beds are common in high-energy flow regimes of T_a facies in an ideal Bouma sequence (Figure 4.14).

Figure 4.16, track 9 compares total water saturation estimated with both conventional petrophysical analysis and electrical anisotropy analysis assuming anisotropic sands. Along the depth interval X152-X158 m, water saturation estimated with anisotropy analysis yields values ranging between 50 and 70%, which are much lower than water saturation obtained with conventional petrophysical analysis (75-100%). Such low values of water saturation calculated with anisotropy analysis are inconsistent with water saturation estimated with capillary pressure. Figure 4.16, track 8 compares water saturation calculated with both conventional petrophysical analysis and electrical anisotropy analysis assuming isotropic sands. Water saturation estimated with anisotropy analysis assuming isotropic sands is in closer agreement with water saturation calculated

with conventional petrophysical analysis. It would be appropriate to compare water saturation calculated with different methods to core laboratory water saturation, if available.

In laminated sands with shale fractions lower than 70%, sand porosity and sand water saturation are similar to porosity and water saturation of thick sands. However, depth intervals with shale fraction greater than 70% exhibit a decrease of sand reservoir quality. This low reservoir quality may be caused by depositions from low-energy flow regimes with fine grain particles and poor sorting.

Along the depth interval X146.5-X156 m, we observe separation of apparent resistivity curves with different radial lengths of investigation, which indicates that well logs are affected by mud-filtrate invasion. It also indicates presence of mobile water pore volume. Additionally, NMR measurements remain sensitive to oil-base mud filtrate due to their relative shallow radial length of investigation. Figure 4.17 shows results obtained with numerical simulations of NMR *T2* distributions at depth X148 m. An excellent agreement was obtained between field and numerically simulated *T2* distributions. Due to oil-base mud-filtrate invasion, NMR simulations exhibit higher values of oil saturation than those obtained from anisotropy analysis. Table 4.5 summarizes the parameters assumed in the numerical simulations.

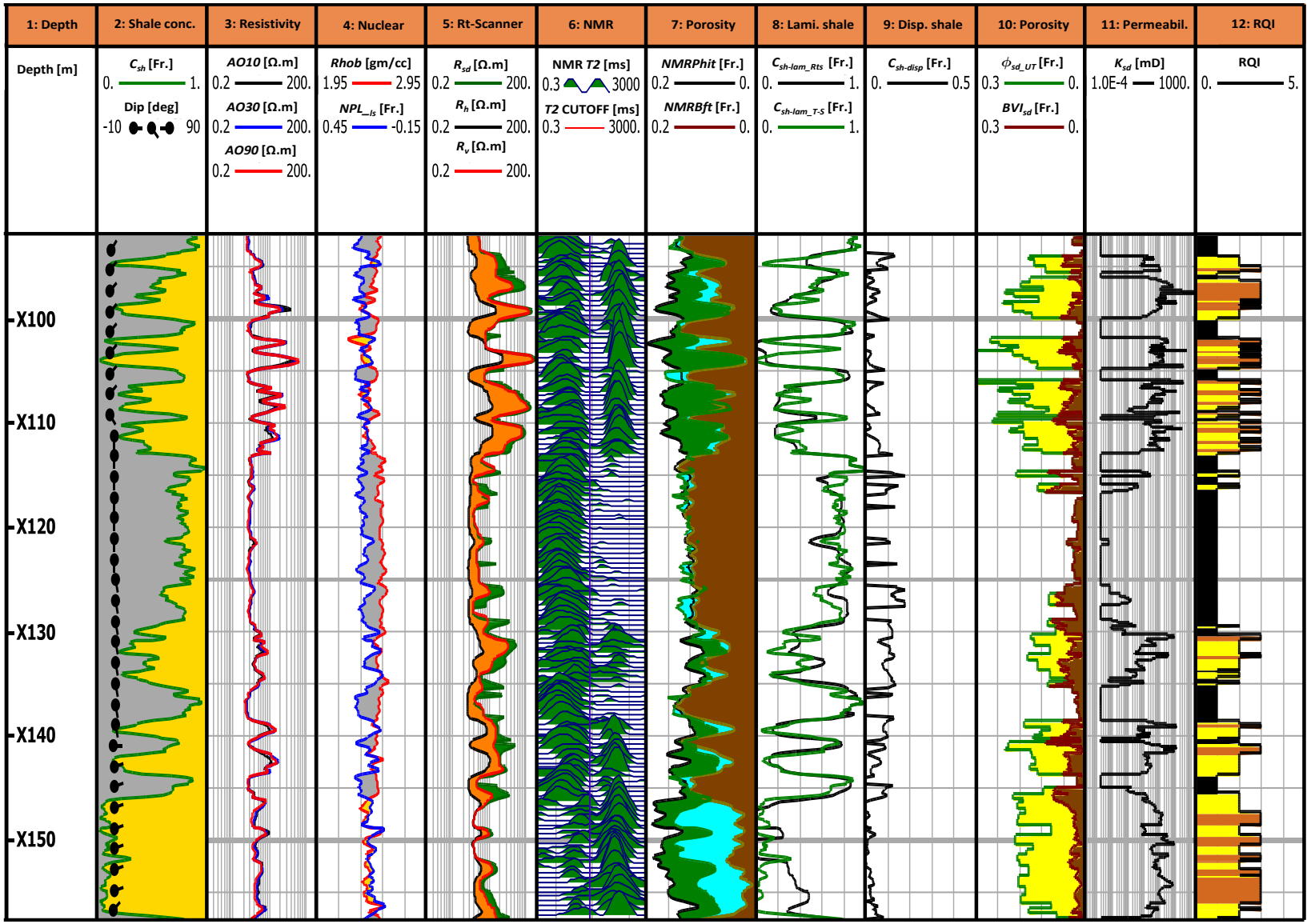
1: Depth
2: Shale conc.
3: Resistivity
4: Nuclear
5: Rt-Scanner
6: NMR
7: Porosity
8: Lami. shale
9: Disp. shale
10: Porosity
11: Permeabil.
12: RQI
Depth [m]
C_{sh} [Fr.]
0. 1.
Dip [deg]
-10 90
AO10 [Ω.m]
0.2 200.
AO30 [Ω.m]
0.2 200.
AO90 [Ω.m]
0.2 200.
Rhob [gm/cc]
1.95 2.95
NPL_{ls} [Fr.]
0.45 -0.15
R_{sd} [Ω.m]
0.2 200.
R_h [Ω.m]
0.2 200.
R_v [Ω.m]
0.2 200.
NMR T2 [ms]
0.3 3000
T2 CUTOFF [ms]
0.3 3000.
NMRPhit [Fr.]
0.2 0.
NMRBft [Fr.]
0.2 0.
$C_{sh\text{-}lam\_Rts}$ [Fr.]
0. 1.
$C_{sh\text{-}lam\_T\text{-}S}$ [Fr.]
0. 1.
$C_{sh\text{-}disp}$ [Fr.]
0. 0.5
ϕ_{sd_UT} [Fr.]
0.3 0.
BVI_{sd} [Fr.]
0.3 0.
K_{sd} [mD]
1.0E-4 1000.
RQI
0. 5.
X100
X110
X120
X130
X140
X150

Figure 4.15: Results obtained from the anisotropy analysis in Well γ. Track 1: depth. Track 2: volumetric shale concentration and formation dip. Track 3: apparent resistivity curves with different radial lengths of investigation. Track 4: bulk density and neutron (limestone matrix) log. Track 5: sand, horizontal, and vertical resistivity. Track 6: NMR *T2* distributions. Track 7: NMR total porosity and bound fluid. Track 8: volumetric laminar shale concentrations estimated with Rt-Scanner measurements and Thomas-Stieber's method. Track 9: volumetric dispersed shale concentration in the sand layers. Track 10: shoulder-bed corrected sand porosity and sand irreducible bulk volume. Track 11: sand permeability. Track 12: sand reservoir quality.

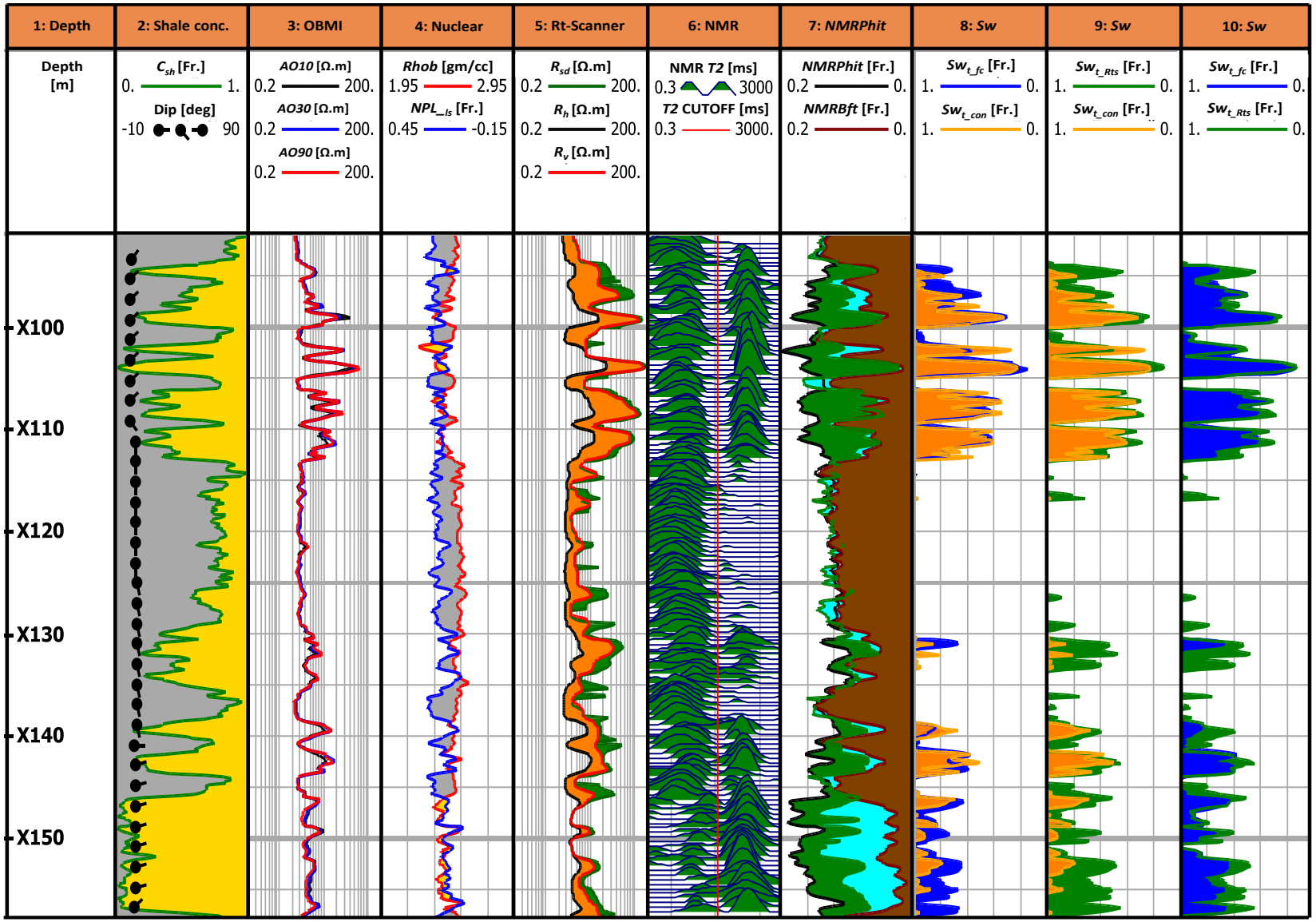
1: Depth
2: Shale conc.
3: OBMI
4: Nuclear
5: Rt-Scanner
6: NMR
7: NMRPhit
8: Sw
9: Sw
10: Sw
Depth [m]
Csh [Fr.] 0. 1.
Dip [deg] -10 90
AO10 [Ω.m] 0.2 200.
AO30 [Ω.m] 0.2 200.
AO90 [Ω.m] 0.2 200.
Rhob [gm/cc] 1.95 2.95
NPL_ls [Fr.] 0.45 -0.15
Rsd [Ω.m] 0.2 200.
Rh [Ω.m] 0.2 200.
Rv [Ω.m] 0.2 200.
NMR T2 [ms] 0.3 3000
T2 CUTOFF [ms] 0.3 3000.
NMRPhit [Fr.] 0.2 0.
NMRBft [Fr.] 0.2 0.
Swt_fc [Fr.] 1. 0.
Swt_con [Fr.] 1. 0.
Swt_Rts [Fr.] 1. 0.
Swt_con [Fr.] 1. 0.
Swt_fc [Fr.] 1. 0.
Swt_Rts [Fr.] 1. 0.
X100
X110
X120
X130
X140
X150

Figure 4.16: Results obtained from the anisotropy analysis in Well γ. Track 1: depth. Track 2: volumetric shale concentration and formation dip. Track 3: apparent resistivity curves with different radial lengths of investigation. Track 4: bulk density and neutron (limestone matrix) log. Track 5: sand, horizontal, and vertical resistivity. Track 6: NMR *T2* distributions. Track 7: NMR total porosity and bound fluid. Track 8: total water saturation estimated with conventional petrophysical analysis and anisotropy analysis assuming isotropic sands. Track 9: total water saturation estimated with conventional petrophysical analysis and anisotropy analysis assuming anisotropic sands. Track 10: total water saturation estimated with anisotropy analysis assuming isotropic and anisotropic sands.

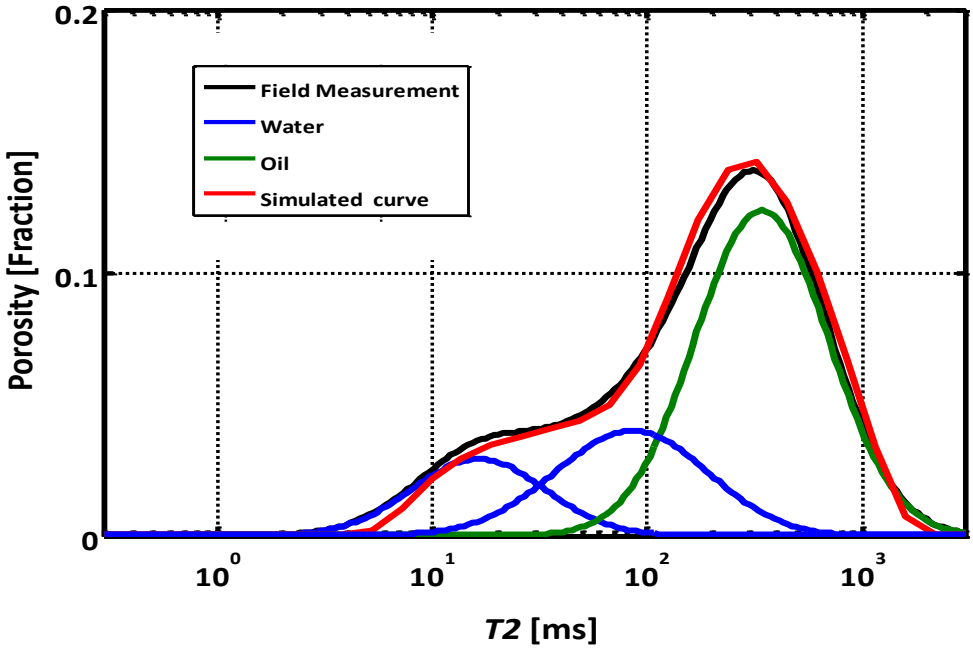

Figure 4.17: Results obtained from numerical simulations of NMR *T2* distribution at depth X148 m, Well γ. An excellent agreement is obtained between field and numerically simulated *T2* distribution. Table 4.5 summarizes the parameters assumed in the numerical simulations.

Petrophysical Property	Value	Units
Sw_{sh}	1	[Fraction]
Sw_t	0.38	[Fraction]
Sw_{sd_irr}	0.15	[Fraction]
Shc_{sd}	0.62	[Fraction]
$C_{sh\text{-}lam}$	0	[Fraction]

Table 4.5: Parameters assumed in the numerical simulation of NMR *T2* distributions at depth X148 m, Well γ. Figure 4.17 shows the corresponding numerical simulation.

4.5 FIELD CASE NO. 4: WELL τ

This section of the well comprises a thinly bedded sand-shale sequence overlying a clean formation (Figure 4.20). The formation is a consolidated calcareous turbidite sequence with porosity values ranging between 5% and 12% and permeability values ranging between 0.001 mD and 1 mD. Sand porosity is lower than shale porosity at the majority of depth intervals. Apparent resistivity curves with different radial lengths of investigation indicate shallow to negligible invasion. Formation dip estimated from Rt-Scanner measurements is lower than 10 degrees. Core photographs, OBMI images, relatively large separation between horizontal and vertical resistivities, and bimodal character of NMR *T2* distributions confirm the presence of thin beds.

Figure 4.21, track 11 shows the mineral concentrations obtained with linear mineral inversion. Results obtained from linear mineral inversion indicate high values of calcite concentration, ranging between 30% and 100%. Petrographical analysis indicates that the formation is highly affected by calcite cementation, thereby causing porosity and permeability to decrease drastically, giving rise to low sand reservoir quality.

Figure 4.20, track 8 compares laminar shale concentration obtained with Thomas-Stieber's method and Rt-Scanner measurements. Below X145 m, at a majority of the depth intervals, laminar shale concentration calculated with Rt-Scanner measurements and Thomas-Stieber's method are in close agreement. Figure 4.18 shows core images acquired along the depth interval X212-X213 m; they indicate absence of laminar shale concentration. Along the same depth interval, laminar shale concentration calculated with Thomas-Stieber's method and Rt-Scanner measurements is lower than 3%.

However, along the depth intervals X119-X125 m and X129–X139 m, laminar shale concentration estimated with Rt-Scanner measurements is lower than that obtained with Thomas-Stieber's method. Along the same depth interval, anisotropy values range

between 1 and 2.5. Such low anisotropy values could be caused by ripples and bioturbated formations observed on core images acquired within the depth interval X122.7-X123.7 m (Figure 4.19).

Dispersed shale concentration in sand units ranges between 0% and 12%, which is consistent with shale concentration estimated with XRD measurements.

Figure 4.20, track 10 shows shoulder-bed corrected sand porosity, sand irreducible water saturation, and core porosity. Shoulder-bed corrected petrophysical properties agree well with core measured properties. Figure 4.20, track 12 describes the corresponding sand reservoir quality. The formation exhibits negligible to poor sand reservoir quality.

Figure 4.21, track 10 describes non-shale water saturation estimated with both conventional and electrical anisotropy analysis. A slight improvement in hydrocarbon reserves calculation was obtained with electrical anisotropy analysis when compared to conventional petrophysical analysis.

Depth interval: X212-X213 m, Well τ

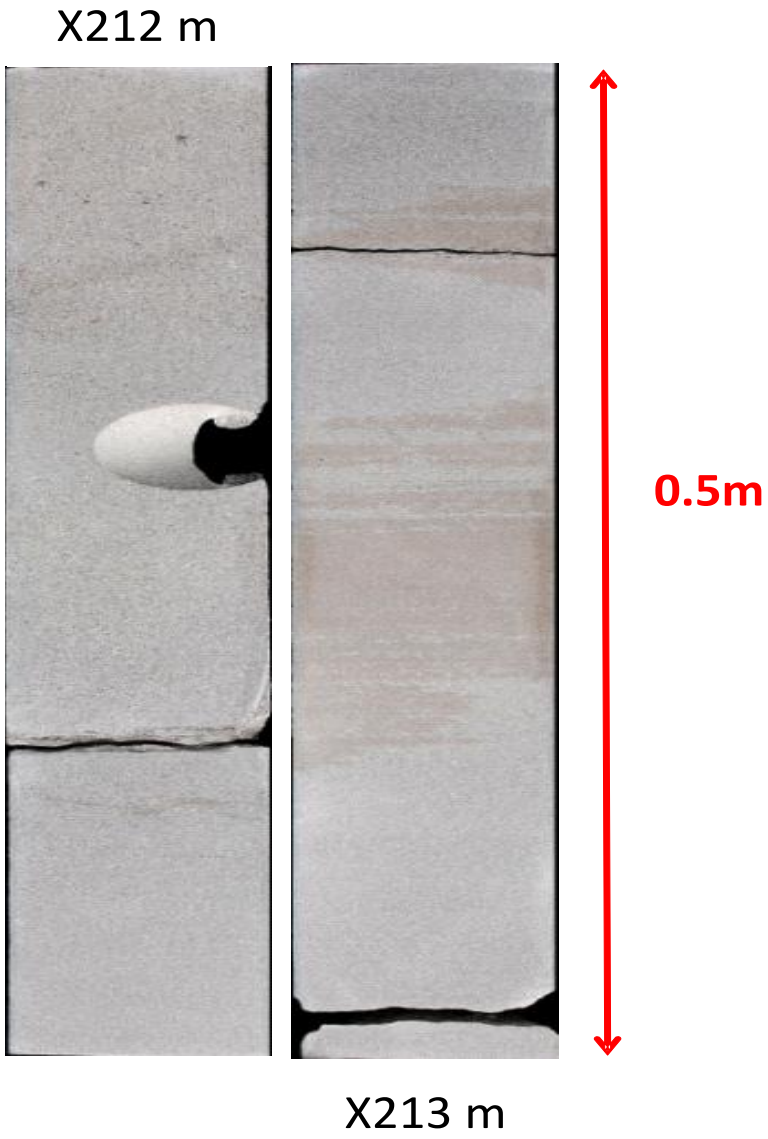

Figure 4.18: Core photographs from the depth interval X212-X213 m, in Well τ, indicating absence of laminar shale concentration.

Depth interval: X122.7-X123.7 m, Well τ

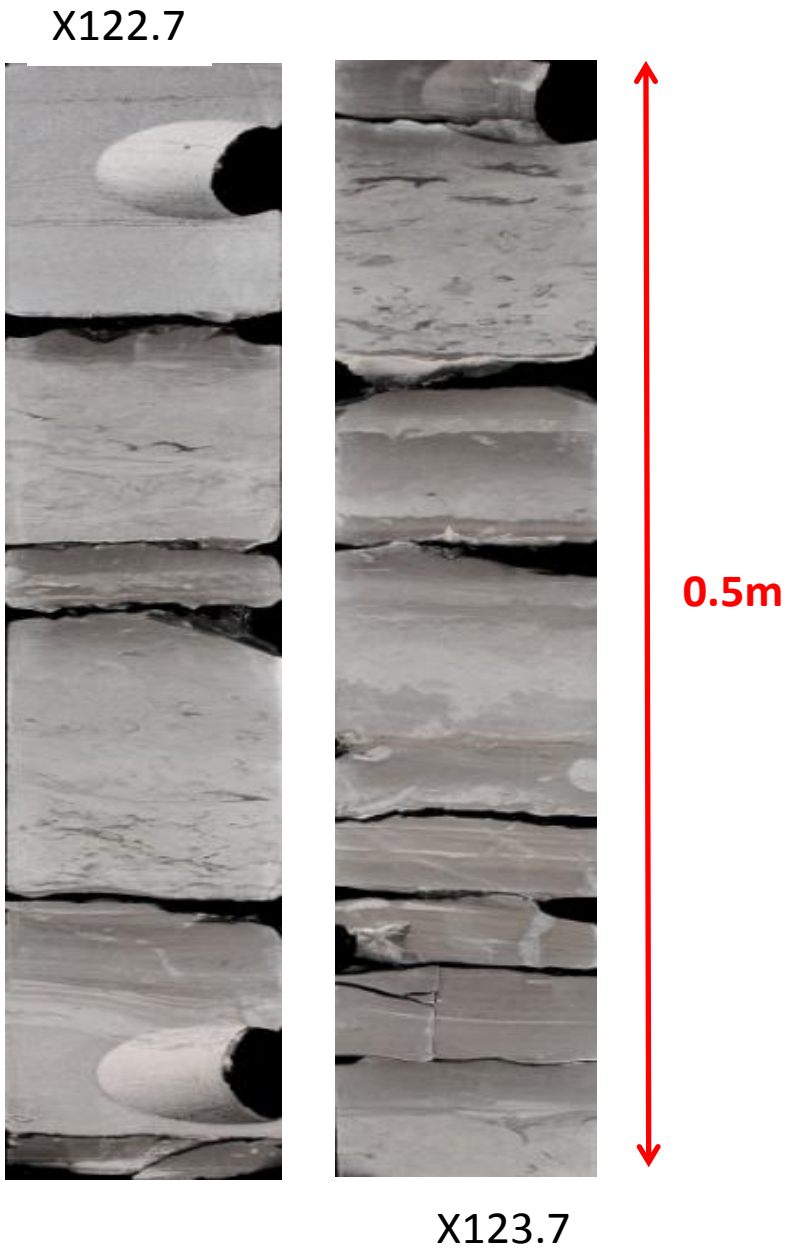

Figure 4.19: Core photographs from the depth interval X122.7-X123.7 m, Well τ, indicating presence of ripples and bioturbated formations.

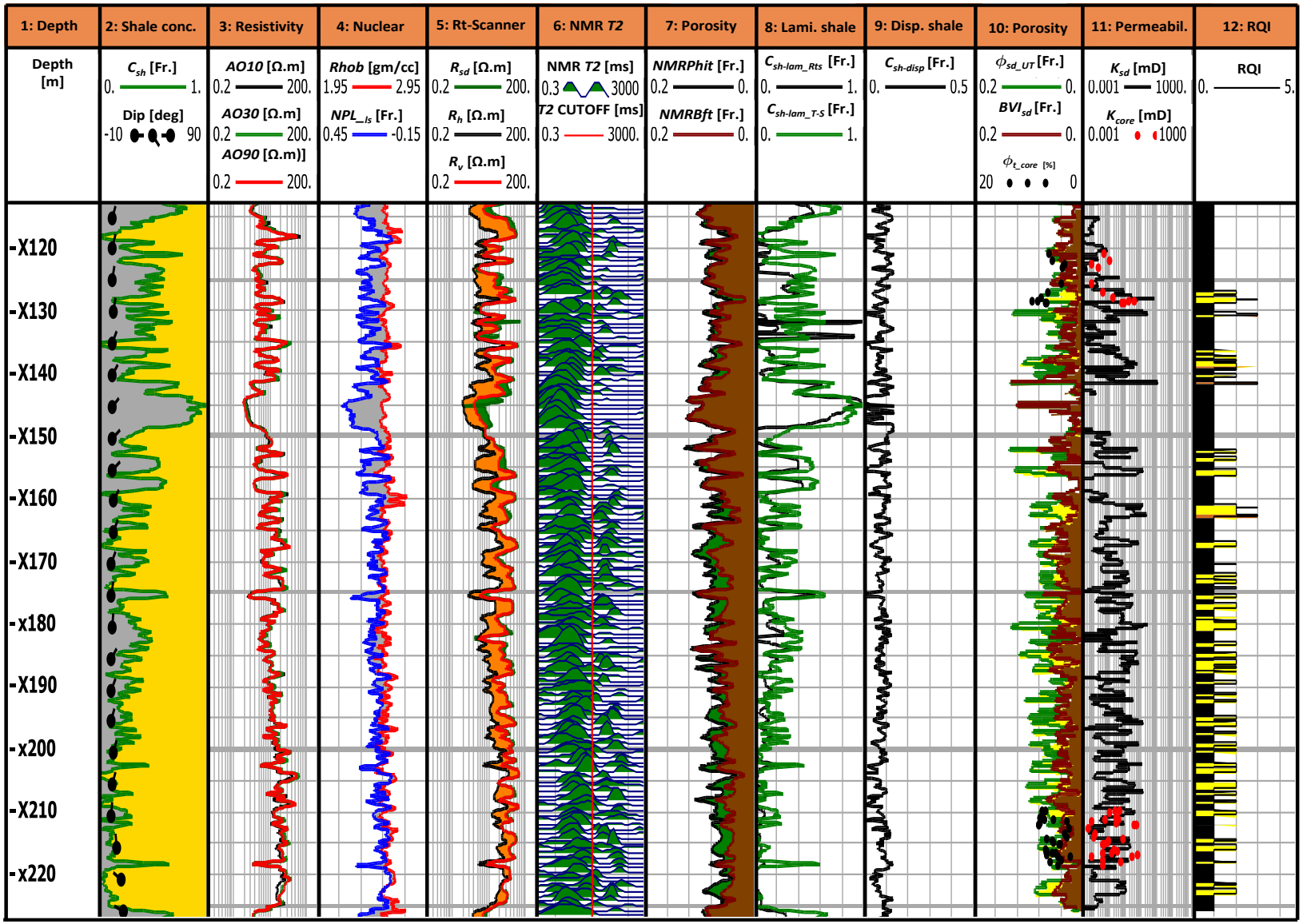
1: Depth
2: Shale conc.
3: Resistivity
4: Nuclear
5: Rt-Scanner
6: NMR T2
7: Porosity
8: Lami. shale
9: Disp. shale
10: Porosity
11: Permeabil.
12: RQI
Depth [m]
Csh [Fr.]
0. 1.
Dip [deg]
-10 90
AO10 [Ω.m]
0.2 200.
AO30 [Ω.m]
0.2 200.
AO90 [Ω.m)]
0.2 200.
Rhob [gm/cc]
1.95 2.95
NPL_ls [Fr.]
0.45 -0.15
Rsd [Ω.m]
0.2 200.
Rh [Ω.m]
0.2 200.
Rv [Ω.m]
0.2 200.
NMR T2 [ms]
0.3 3000
T2 CUTOFF [ms]
0.3 3000.
NMRPhit [Fr.]
0.2 0.
NMRBft [Fr.]
0.2 0.
Csh-lam_Rts [Fr.]
0. 1.
Csh-lam_T-S [Fr.]
0. 1.
Csh-disp [Fr.]
0. 0.5
ϕsd_UT [Fr.]
0.2 0.
BVIsd [Fr.]
0.2 0.
ϕt_core [%]
20 0
Ksd [mD]
0.001 1000.
Kcore [mD]
0.001 1000
RQI
0. 5.
-X120
-X130
-X140
-X150
-X160
-X170
-x180
-X190
-x200
-X210
-x220

Figure 4.20: Results obtained from anisotropy analysis in Well τ. Track 1: depth. Track 2: volumetric shale concentration and formation dip. Track 3: apparent resistivity curves with different radial lengths of investigation. Track 4: bulk density and neutron (limestone matrix) log. Track 5: sand, horizontal, and vertical resistivity. Track 6: NMR *T2* distributions. Track 7: NMR total porosity and bound fluid. Track 8: volumetric laminar shale concentrations estimated with Rt-Scanner measurements and Thomas-Stieber's method. Track 9: volumetric dispersed shale concentration in the sand layers. Track 10: shoulder-bed corrected sand porosity, sand irreducible bulk volume, and core porosity. Track 11: sand and core permeability. Track 12: sand reservoir quality.

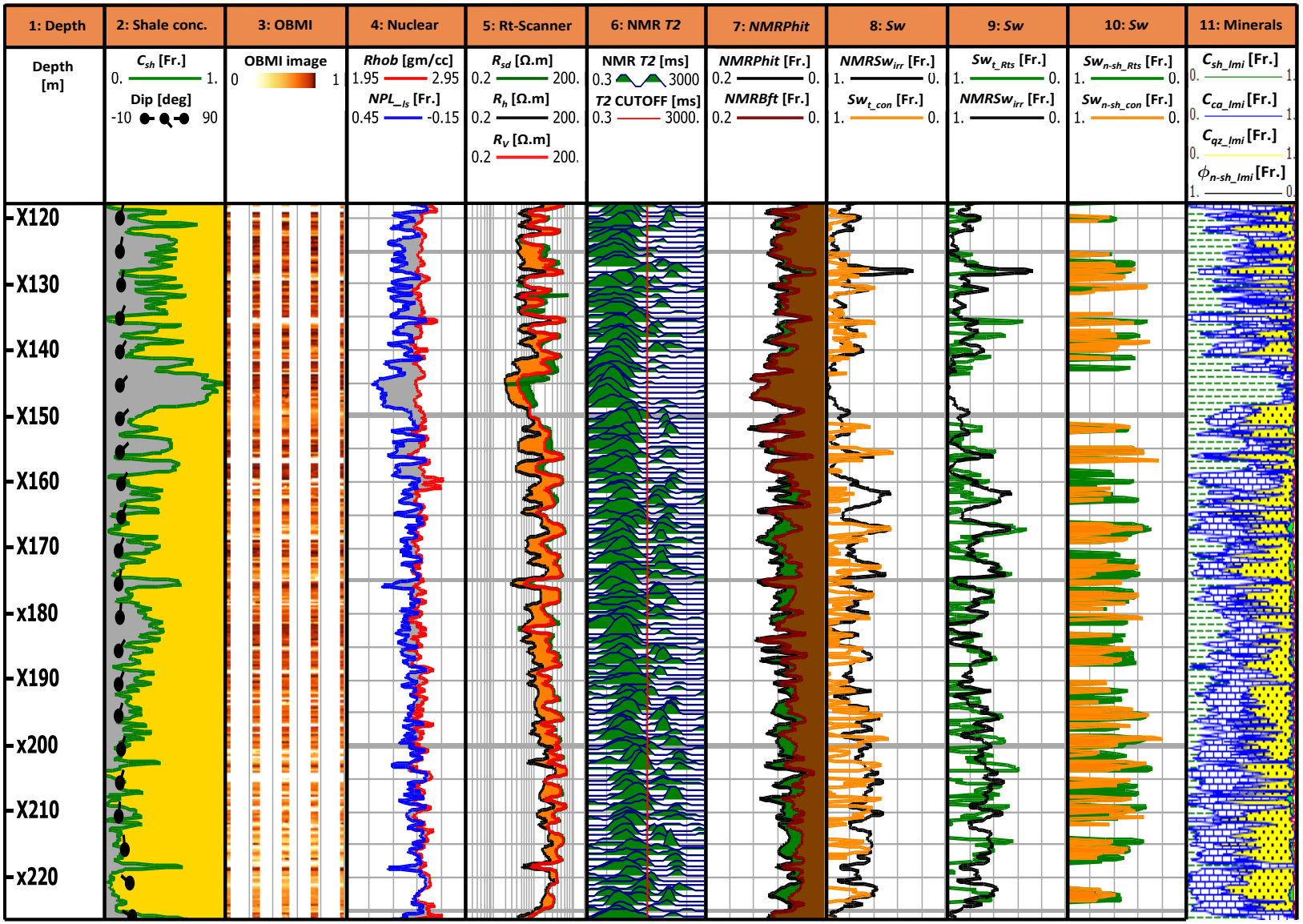
1: Depth
2: Shale conc.
3: OBMI
4: Nuclear
5: Rt-Scanner
6: NMR T2
7: NMRPhit
8: Sw
9: Sw
10: Sw
11: Minerals
Depth [m]
Csh [Fr.]
0. 1.
Dip [deg]
-10 90
OBMI image
0 1
Rhob [gm/cc]
1.95 2.95
NPL_ls [Fr.]
0.45 -0.15
Rsd [Ω.m]
0.2 200.
Rh [Ω.m]
0.2 200.
RV [Ω.m]
0.2 200.
NMR T2 [ms]
0.3 3000
T2 CUTOFF [ms]
0.3 3000.
NMRPhit [Fr.]
0.2 0.
NMRBft [Fr.]
0.2 0.
NMRSwirr [Fr.]
1. 0.
Swt_con [Fr.]
1. 0.
Swt_Rts [Fr.]
1. 0.
NMRSwirr [Fr.]
1. 0.
Swn-sh_Rts [Fr.]
1. 0.
Swn-sh_con [Fr.]
1. 0.
Csh_lmi [Fr.]
0. 1.
Cca_lmi [Fr.]
0. 1.
Cqz_lmi [Fr.]
0. 1.
ϕn-sh_lmi [Fr.]
1. 0.
X120
X130
X140
X150
X160
X170
x180
X190
x200
X210
x220

Figure 4.21: Results obtained from anisotropy analysis in Well τ. Track 1: depth. Track 2: volumetric shale concentration and formation dip. Track 3: OBMI image. Track 4: bulk density and neutron (limestone matrix) log. Track 5: sand, horizontal, and vertical resistivity. Track 6: NMR *T2* distributions. Track 7: NMR total porosity and bound fluid. Track 8: total water saturation from conventional petrophysical analysis and irreducible water saturation. Track 9: total water saturation from anisotropy analysis and irreducible water saturation. Track 10: non-shale water saturation from anisotropy analysis and conventional petrophysical analysis. Track 11: results obtained from linear mineral inversion.

4.6 CALCULATIONS OF HYDROCARBON PORE-THICKNESS

Table 4.6 summarizes hydrocarbon pore-thickness *(HPT)* obtained from conventional petrophysical analysis and anisotropy analysis for all four wells. For *HPT* calculations via conventional petrophysical analysis, we assumed 5% as porosity cut-off, 75% as shale concentration cut-off, and 75% as water saturation cut-off. Even with these relatively liberal cut-offs, conventional petrophysical analysis underestimated *HPT* when compared to anisotropy analysis.

Well	Conventional Petrophysical Analysis, *HPT* (m)	Anisotropy Analysis, *HPT* (m)
α	0.4	0.97
β	0.83	1.68
γ	1.15	1.53
τ	0.91	1.15

Table 4.6: Comparison of hydrocarbon pore-thickness (*HPT*) obtained from conventional and anisotropy analysis in different wells across the reservoir.

4.7 DISCUSSION

We applied the developed method to four field cases of thinly bedded sand-shale sequences. In Well α, we encountered a highly heterogeneous formation that has low-porosity, high-resistivity streaks along a few depth intervals. We applied electrical anisotropy analysis and high-resolution interpretation method to estimate hydrocarbon reserves. Results show that electrical anisotropy analysis overestimates hydrocarbon

reserves in rocks composed of low-porosity, high-resistivity streaks. However, the high-resolution interpretation method yields petrophysically consistent results in such rock formations.

In addition, we encountered a low-resistivity, low-contrast (LRLC) zone in Well β, depth interval X070-X080 m. Conventional well logs fail to detect this hydrocarbon reservoir. However, advanced wireline measurements, such as Rt-Scanner and NMR measurements, facilitate the identification of this low-resistivity, low-contrast zone. Along this depth interval, conventional petrophysical analysis underestimates hydrocarbon reserves compared to results obtained with anisotropy analysis.

The best reservoir quality rocks are observed in Well γ, depth interval X092-X158 m with predominant sand porosity values ranging between 16% and 20%. Formations consist mainly of laminar shale with a limited amount of dispersed shale. In contrast, the worst reservoir rocks are observed in Well τ, depth interval X120-X225 m. In this section of the reservoir, predominant sand porosity values range between 4% and 8%. Formations are substantially affected by calcite cementation thereby reducing the sand reservoir quality.

Chapter 5: Summary and Conclusions

This chapter summarizes the recommended best practices for petrophysical evaluation of thinly bedded formations and reports the salient conclusions stemming from the study.

5.1 Recommended Practices

Figure 5.1 summarizes our recommended best practices for petrophysical evaluation of thinly bedded sand-shale sequences. This workflow enables the estimation of consistent petrophysical properties using conventional well logs, NMR, Rt-Scanner, OBMI, and core measurements.

The first step in the petrophysical evaluation of thinly bedded formation is identification of thin beds. If thin beds are suspected, a logging program should be designed capable of identifying and quantifying thin beds. We recommend slower logging speeds to acquire high-resolution logging data with acceptable quality. In addition, acquisition of advanced wireline measurements, such as NMR, resistivity images, and multi-component induction, should be incorporated because they provide strong evidence of presence of thin beds. Core images should also be acquired because they serve as ground truth to identify and quantify volumetric laminar shale fraction.

In addition, acquisition of core plugs should be designed to obtain a good representation of all rock types present in reservoir. It is important to emphasize that acquiring core plugs from good reservoir beds alone will lead to overly optimistic and unrealistic petrophysical results.

A crucial step in the petrophysical evaluation of thin beds is the depth alignment of well logs and core data. Even a slight mismatch of well logs due to, for instance, varying logging speed, tool stuck and release, etc., can lead to erroneous results.

An estimate of bed thickness can be obtained by detecting bed boundaries from density logs, which exhibit the highest vertical resolution among conventional well logs. In addition, short-space density detector data can be used to diagnose beds with thickness of up to half a foot. Moreover, high vertical resolution logs, such as resistivity images, provide good statistical distribution of bed thickness. Resistivity image logs should be compared to core images to verify that high-resolution resistivity curves respond to beds visible in core images.

For petrophysical evaluation of thinly bedded sand-shale sequences, precise calculation of laminar shale concentration is of prime importance. We recommend estimation of laminar shale concentration from at least two laminar shale indicators. In this study, we calculated laminar shale concentration from Thomas-Stieber's method, Rt-Scanner, and OBMI measurements. Further, we classified rocks into three categories: laminated with isotropic sands, anisotropic sands, and low-porosity, high-resistive streaks. Different interpretation methods were implemented for each rock class. Table 5.1 summarizes the wireline measurements that played a major role in the petrophysical evaluation of each rock class.

Rock types	Recommended measurements
Thick beds, isotropic sands	Conventional well logs
Thick beds, anisotropic sand	Multi-component induction + NMR
Thin beds, isotropic sand	Multi-component induction
High resistive streaks	Resistivity image

Table 5.1: Summary of wireline measurements used in the petrophysical evaluation of rock types encountered in the reservoir.

The following are recommended interpretation methods for each rock class encountered in the reservoir:

(1) Thick beds with isotropic sands: Rocks are composed of thick beds with isotropic sands. Conventional methods (shaly-sand equations, dual-water, Waxman-Smits, etc.) of estimating hydrocarbon reserves yield petrophysically consistent results in this rock class because wireline measurements resolve true bed petrophysical properties.

(2) Thick beds with anisotropic sands: Rocks are composed of thick beds with anisotropic sands. Electrical anisotropy analysis provides consistent results for this rocks class. Tensor resistivity equations are calculated for fine-grain and coarse-grain resistivities, while fine-grain and coarse-grain concentrations are input to the tensor resistivity model. Fine-grain and coarse-grain concentrations are estimated with NMR measurements.

(3) Thin beds and isotropic sands: Conventional shaly-sand equations (dual-water, Waxman-Smits, etc.) underestimate hydrocarbon reserves in thinly bedded formations. However, electrical anisotropy analysis provides petrophysically

consistent results in this rock class. The tensor resistivity model is implemented to calculate laminar shale concentration and sand resistivity, while horizontal and vertical shale resistivities are identified from representative shale interval.

(4) Low-porosity, high resistivity streaks: Low-porosity, high-resistivity streaks can give rise to electrical anisotropy, which can be misinterpreted as thinly bedded sand-shale sequences. This case of electrical anisotropy can cause errors in estimating hydrocarbon reserves through electrical anisotropy analysis. For this rock class, the high-resolution interpretation method yields petrophysically consistent results. Accordingly, high-resolution measurements, such as OBMI, are integrated with the petrophysical interpretation procedure.

Petrophysical properties estimated with the implementation of different methods for each rock class are validated by performing numerical simulations of NMR *T2* distributions. Through NMR simulations, we estimated pore-size distributions, in-situ fluid concentration, and in-situ fluid properties.

Petrophysical and compositional properties, such as shale concentration, laminar shale concentration, shale porosity, porosity, etc., are refined until securing petrophysically consistent properties that honor all the available measurements. Conventional methods tend to underestimate permeability in thinly bedded sand-shale sequences. In this study, we estimated permeability of sand units via Timur-Coates' equation by removing the effects of laminar shale concentration on porosity and bulk irreducible volume. Shoulder-bed corrected porosity and shale concentration logs were used in the calculations.

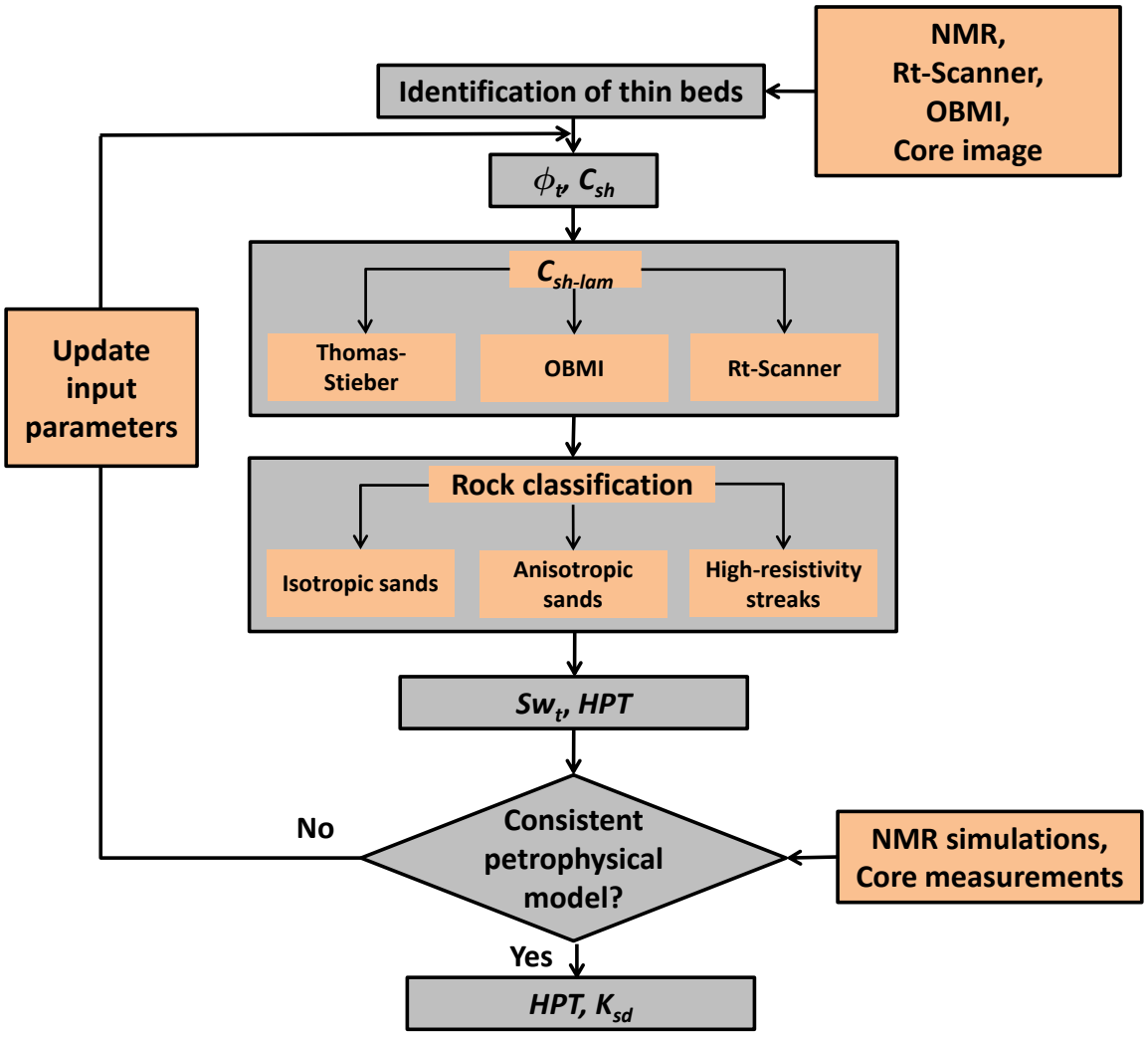

Figure 5.1: Interpretation algorithm describing our recommended best practices for petrophysical evaluation of thinly bedded rock formations.

5.2 SUMMARY AND CONCLUSIONS

Field examples considered in this study indicated that improved and accurate estimates of hydrocarbon reserves can be obtained through the integration of measurements such as conventional well logs, NMR, resistivity images, multi-component induction, etc. On average, results obtained with the new interpretation method yielded a 62% increase in hydrocarbon pore thickness when compared to conventional petrophysical analysis. In addition, permeability estimated with the new method exhibited 16% better agreement with core measurements than calculations performed with conventional well logs.

In the analysis of thinly bedded sand-shale sequences, accurate calculation of laminar shale concentration was of prime importance. Errors in laminar shale concentration propagate to the calculations of hydrocarbon pore-thickness. To reduce these errors, we integrated laminar shale concentration estimated with Thomas-Stieber's method, OBMI, and Rt-Scanner measurements. For calculations of laminar shale concentration from Thomas-Stieber's method, porosity end points, maximum sand porosity, $\phi_{sd\text{-}max}$, shale porosity, ϕ_{sh}, and total shale concentration, C_{sh}, were iteratively refined to obtain consistent results with laminar shale concentration values estimated with Rt-Scanner and OBMI measurements. Subsequently, laminar shale concentration values estimated with Thomas-Stieber's method were used to calculate hydrocarbon reserves.

We also appraised the high-resolution method for petrophysical evaluation of thinly bedded formations. In this method, accurate delineation of bed boundaries was crucial for precise evaluation of hydrocarbon reserves. OBMI measurements cannot resolve bed boundaries when beds are thinner than their intrinsic vertical resolution (1.5 inches). In such cases, petrophysical evaluation with the high-resolution interpretation method remains inaccurate and non-unique. Moreover, in formations with beds thinner

than 3 inches, the petrophysical interpretation model can still be insufficiently constrained. Reducing interpretation uncertainties requires validation of petrophysical properties with additional measurements such as NMR and core data.

Electrical anisotropy measured with multi-component induction tools remains affected by laminar shale, anisotropic sands, low-porosity high resistivity streaks, etc. In order to account for all of these factors in the interpretation, rock classification was conducted by implementing different interpretation methods for each rock class.

We observed that the electrical anisotropy analysis of rocks comprising low-porosity, high resistivity streaks overestimates hydrocarbon reserves. The high-resolution interpretation method provides petrophysically consistent results for these rock formations.

Shales were electrically anisotropic in the studied reservoir; anisotropy values ranged between 1.2 and 2. Neglecting shale anisotropy in the calculations was found to falsely indicate presence of thinly bedded formations, which could further result in overestimation of hydrocarbon reserves.

In addition, we performed numerical simulations of NMR *T2* distributions to validate petrophysical properties determined with the anisotropy analysis. Through NMR numerical simulations, we estimated pore-size distributions, in-situ fluid concentrations, and in-situ fluid properties. In the studied reservoir, NMR numerical simulations indicated presence of highly viscous oil. In addition, NMR porosity was in good agreement with porosity derived from linear mineral inversion.

We quantified sand reservoir quality using Leverett's rock quality index, $\mathrm{RQI} = \sqrt{k/\phi}$. Results indicated that sand units interbedded with shale layers exhibit good reservoir quality, similar to that of clean thick sands. Figure 5.2 describes the distribution of hydrocarbon pore thickness with increasing laminar shale concentration.

In the studied reservoir, approximately 50% of the total hydrocarbon pore volume is located within depth intervals where laminar shale concentration is greater than 30%. For each rock class, we studied thin sections, SEM images, and capillary pressure curves. Results indicated that sand reservoir quality increases with an increase in both grain size and interconnected porosity, and decreases with an increase in both calcite and authigenic clay cementation.

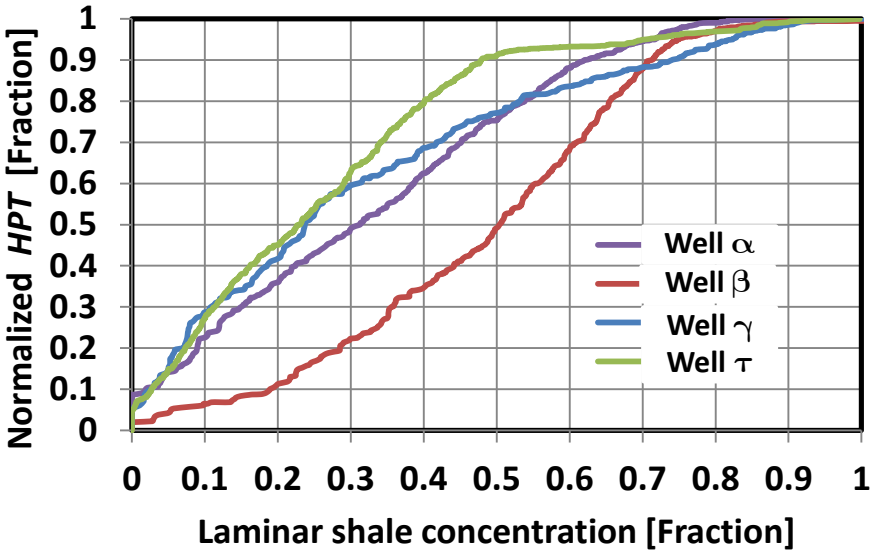

Figure 5.2: Distribution of hydrocarbon pore-thickness (*HPT*) with increasing laminar shale concentration in the four wells considered in this thesis.

5.3 LIMITATIONS

Rt-Scanner measurements exhibit relatively low vertical resolution (5 ft) compared to the vertical resolution of other wireline measurements, such as gamma-ray (2 ft), density (1 ft), neutron (2 ft), etc. We speculate that some errors in hydrocarbon reserves estimate were due to differences in the vertical resolution of the various wireline

measurements involved in the interpretation. Several sources of uncertainty in the estimation of petrophysical properties can be reduced by correcting wireline measurements for shoulder-bed effects. However, at the time of this study numerical simulators of Rt-Scanner measurements were not available, which prevented us from taking into account the corresponding shoulder-bed effects in the petrophysical interpretation.

Appendix A: Thomas-Stieber's Method

This appendix describes the assumptions made and equations used to estimate laminar shale concentration, dispersed shale concentration, and sand porosity with Thomas-Stieber's (T-S) method. In the study, the T-S model was restricted to laminar and dispersed shale due to absence of structural shale.

The Thomas-Stieber model is based on the volumetric mixing of laminar, dispersed, and structural shale that governs the values of total porosity and total shale concentration of a rock. Thomas-Stieber crossplots can be constructed using core or well log data. The Thomas-Stieber diagram should be constructed for short depth interval in order to prevent intermixing of formations from different depositional sequences (Torres-Verdín, 2012)

A.1 Laminated Shale

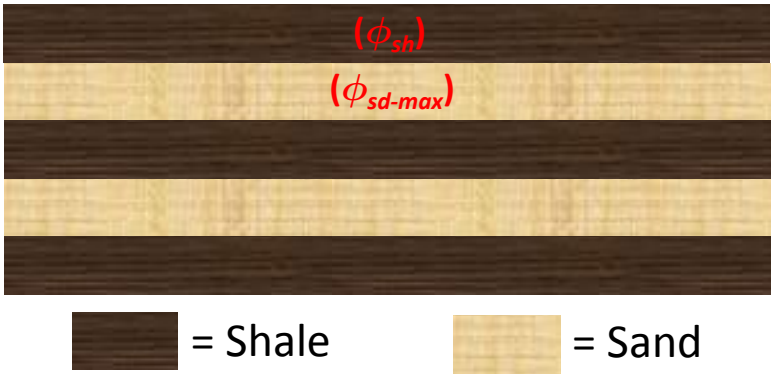

Figure A.1: Description of laminated shaly-sand model. This model comprises an alternating sequence of pure sand and pure shale layers. Shale is not present in the pore space of sand layers.

In this case, we assume that the rock formation is composed of alternating layers of pure sand and pure shale. Shale is not present in the pore space of sand layers. Total porosity and total shale concentration values of these rock formations lie along the locus of laminar shale (Figure A.3). Increasing laminar shale concentration decreases the net-to-gross (*N/G*) ratio but has no effect on the sand portion of the rock. In such systems, total volumetric concentration of shale, C_{sh}, is equal to volumetric laminar shale concentration, $C_{sh\text{-}lam}$. Total porosity on the other hand is the volumetric average of the porosity end points, maximum sand porosity, $\phi_{sd\text{-}max}$, and shale porosity, ϕ_{sh}, i.e.

$$\phi_t = (1 - C_{sh-lam})\phi_{sd-max} + C_{sh-lam}\,\phi_{sh}, \tag{A.1}$$

where ϕ_t is total porosity, $C_{sh\text{-}lam}$ is volumetric laminar shale concentration, $\phi_{sd\text{-}max}$ is maximum sand porosity, and ϕ_{sh} is shale porosity.

A.2 DISPERSED SHALE

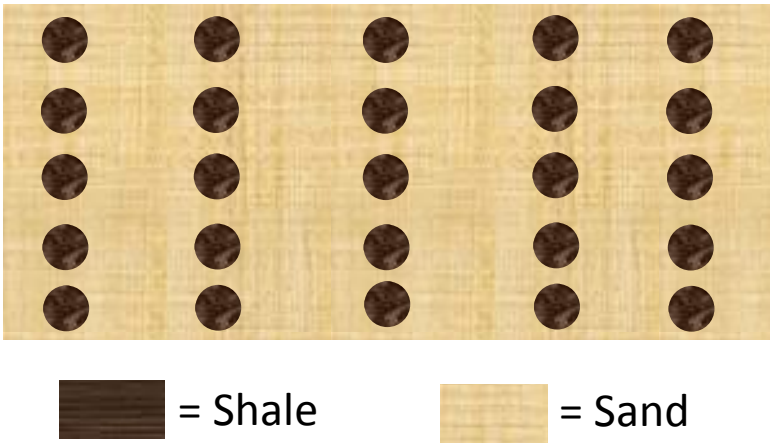

Figure A.2: Description of dispersed shaly-sand model. In this system, shale is present only in the pore space of the rock.

This case assumes that shale is present only in the pore space of the rock. Presence of shale in the pore space of sand affects rock quality. In such systems, total porosity and total shale concentration lie along the dispersed shale line (Figure A.3). The equation used to estimate total porosity in such cases is

$$\phi_t = \phi_{sd-max} - C_{sh} + C_{sh}\phi_{sh}, \tag{A.2}$$

where ϕ_t is total porosity, C_{sh} is total volumetric shale concentration, $\phi_{sd\text{-}max}$ is maximum sand porosity, and ϕ_{sh} is shale porosity.

In such systems, the maximum amount of shale concentration is limited to maximum sand porosity. When shale concentration equals maximum sand porosity, total porosity converges to $\phi_{sd\text{-}max}$ ϕ_{sh}.

Substitution of C_{sh} by $\phi_{sd\text{-}max}$ in equation (A.2) gives

$$\phi_t = \phi_{sd-max} - C_{sh} + C_{sh}\phi_{sh},$$

$$\phi_t = \phi_{sd-max} - \phi_{sd-max} + \phi_{sd-max}\phi_{sh},$$

$$\phi_t = \phi_{sd-max}\phi_{sh}.$$

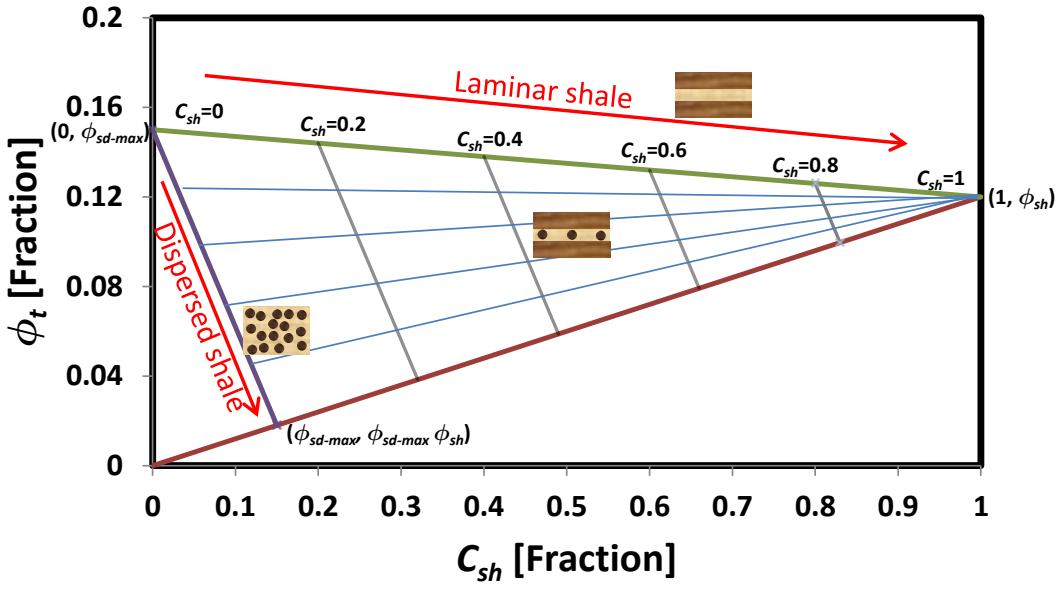

Figure A.3: Graphical representation of the Thomas-Stieber model including the loci of laminar and dispersed shale concentrations.

A.3 MIXED FORMATION

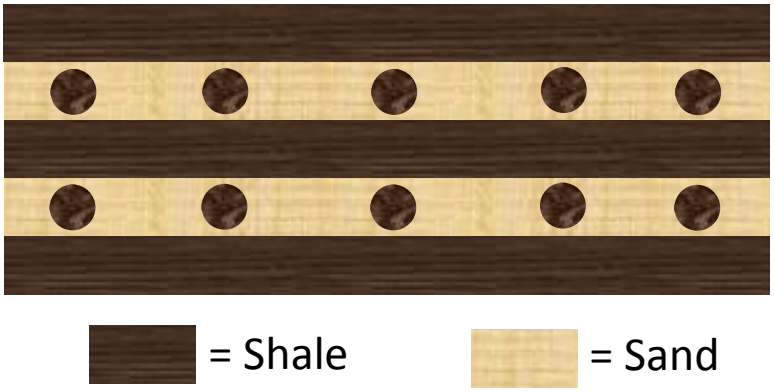

Figure A.4: Description of laminated and dispersed shale model. Shale is present in layers as well as in the pore space of sand units.

In this case, we assume that shale is present in layers as well as in the pore space of sand units. Laminar shale concentration is calculated with Thomas-Stieber's method using the equation

$$C_{sh-lam} = \frac{\phi_t - \phi_{sd-max} + C_{sh}(1-\phi_{sh})}{(1-\phi_{sd-max})}, \tag{A.3}$$

where ϕ_t is total porosity, $C_{sh\text{-}lam}$ is volumetric laminar shale concentration, $\phi_{sd\text{-}max}$ is maximum sand porosity, C_{sh} is total volumetric shale concentration, and ϕ_{sh} is shale porosity.

It is worth emphasizing that equation (A.3) converges to equation (A.1), when the formation is composed of laminar shale only. In such cases, total volumetric shale concentration, C_{sh}, equals volumetric laminar shale concentration, $C_{sh\text{-}lam}$.
Substitution of $C_{sh\text{-}lam}$ by C_{sh} in equation (A.3) yields

$$C_{sh-lam} = \frac{\phi_t - \phi_{sd-max} + C_{sh}(1-\phi_{sh})}{(1-\phi_{sd-max})},$$

$$C_{sh} = \frac{\phi_t - \phi_{sd-max} + C_{sh}(1-\phi_{sh})}{(1-\phi_{sd-max})},$$

$$C_{sh}(1-\phi_{sd-max}) = \phi_t - \phi_{sd-max} + C_{sh}(1-\phi_{sh}),$$

$$C_{sh} - C_{sh}\phi_{sd-max} = \phi_t - \phi_{sd-max} + C_{sh} - C_{sh}\phi_{sh},$$

and

$$\phi_t = \phi_{sd-max}(1-C_{sh}) + C_{sh}\phi_{sh}.$$

Similarly, in the case with dispersed shale only, equation (A.3) converges to equation (A.2). In such cases, the amount of laminar shale concentration equals zero.

Substitution of $C_{sh\text{-}lam}$ with zero in equation (A.3) yields

$$C_{sh-lam} = \frac{\phi_t - \phi_{sd-max} + C_{sh}(1-\phi_{sh})}{(1-\phi_{sd-max})},$$

$$0 = \frac{\phi_t - \phi_{sd-max} + C_{sh}(1-\phi_{sh})}{(1-\phi_{sd-max})},$$

and

$$\phi_t = \phi_{sd-max} - C_{sh} + C_{sh}\phi_{sh}.$$

When the formation comprises both laminar and dispersed shale, the volumetric dispersed shale concentration in the rock is calculated by subtracting total volumetric shale concentration from volumetric laminar shale concentration. The equation used is

$$C_{shd} = C_{sh} - C_{sh-lam}, \tag{A.4}$$

where C_{shd} is dispersed shale concentration, C_{sh} is total volumetric shale concentration, and $C_{sh\text{-}lam}$ is volumetric laminar shale concentration.

Dispersed shale concentration in a sand unit is then calculated by normalizing the total dispersed shale concentration in the rock with the sand fraction. The equation used is

$$C_{sh-disp} = \frac{C_{sh} - C_{sh-lam}}{1-C_{sh-lam}}, \tag{A.5}$$

where $C_{sh\text{-}lam}$ is volumetric laminar shale concentration, $C_{sh\text{-}disp}$ is volumetric dispersed shale concentration in sand units, and C_{sh} is total volumetric shale concentration.

Sand porosity in such systems is calculated with the equation

$$\phi_{sd} = \frac{\phi_t - C_{sh-lam}\phi_{sh}}{(1 - C_{sh-lam})}, \tag{A.6}$$

where ϕ_t is total porosity, ϕ_{sd} is sand porosity, $C_{sh\text{-}lam}$ is volumetric laminar shale concentration, and ϕ_{sh} is shale porosity. Figure A.5 shows the loci of sand porosity, identified with blue lines.

Non-shale porosity in sand units is calculated with the equation

$$\phi_{sd-nsh} = \phi_{sd} - C_{sh-disp}\phi_{sh}, \tag{A.7}$$

where $\phi_{sd\text{-}nsh}$ is non-shale porosity in the sand unit, ϕ_{sd} is sand porosity, $C_{sh\text{-}disp}$ is volumetric dispersed shale concentration in the sand unit, and ϕ_{sh} is shale porosity.

Non-shale porosity of the total volume of the rock is given by the equation

$$\phi_{n-sh} = \phi_t - C_{sh}\phi_{sh}, \tag{A.8}$$

where $\phi_{n\text{-}sh}$ is non-shale porosity, ϕ_t is total porosity, C_{sh} is volumetric shale concentration, and ϕ_{sh} is shale porosity. Figure A.5 shows the loci of non-shale porosity of the rock, identified with red lines.

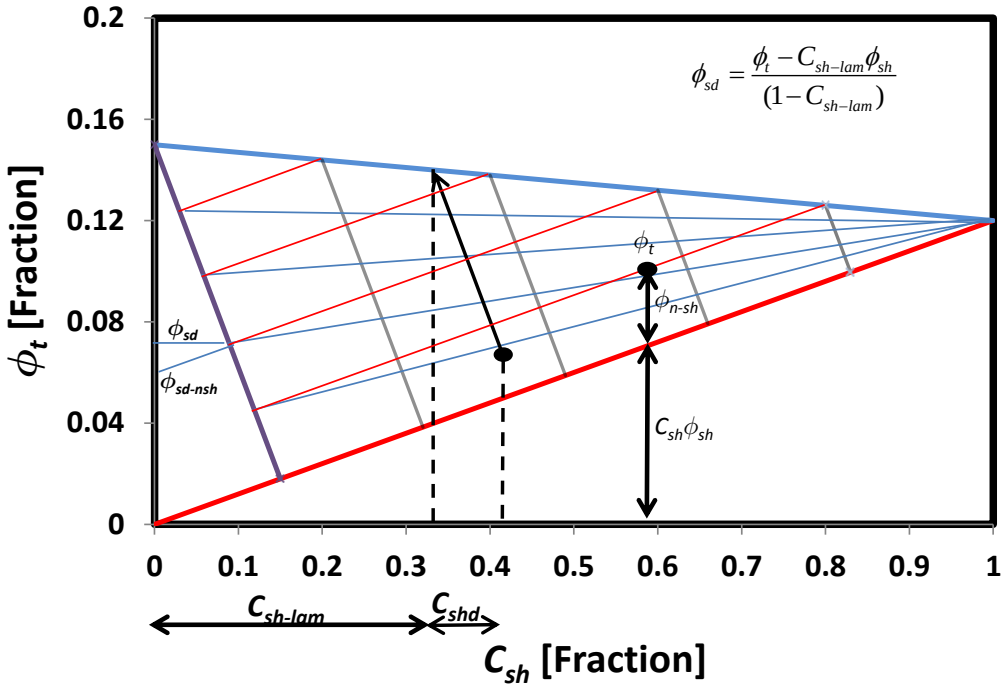

Figure A.5: Thomas-Stieber cross-plot describing the graphical representation of laminar shale concentration, dispersed shale concentration, and sand porosity calculations.

Nomenclature

ϕ_i	:	Partial porosity associated with each bin of the NMR *T2* waveform, [Fraction]
$\phi_{n\text{-}sh}$	:	Non-shale porosity, [Fraction]
$\phi_{n\text{-}sh\_lmi}$	:	Total porosity estimated with linear mineral inversion, [Fraction]
σ_{sd}	:	Sand electrical conductivity, [mho/m]
ϕ_{sd}	:	Sand porosity, [Fraction]
ϕ_{sd_UT}	:	Shoulder-bed corrected sand porosity, [Fraction]
$\phi_{sd\text{-}max}$	:	Maximum sand porosity, [Fraction]
$\phi_{sd\text{-}nsh}$	:	Non-shale porosity of a sand layer, [Fraction]
σ_{sh}	:	Shale electrical conductivity, [mho/m]
ϕ_{sh}	:	Shale porosity, [Fraction]
σ_t	:	Total electrical conductivity, [mho/m]
ϕ_t	:	Total porosity, [Fraction]
ϕ_{t_core}	:	Core porosity, [Fraction]
ϕ_{t_lmi}	:	Total porosity estimated with linear mineral inversion, [Fraction]
ϕ_{t_NMR}	:	Total porosity estimated with NMR measurements, [Fraction]
ϕ_{t_UT}	:	Shoulder-bed corrected total porosity, [Fraction]
a	:	Archie's Winsauer factor, [-]
A	:	Timur-Coates' constant, [mD]
AO10	:	Induction apparent resistivity with one foot vertical resolution and ten inches depth of investigation, [Ohm-m]
AO30	:	Induction apparent resistivity with one foot vertical resolution and thirty inches depth of investigation, [Ohm-m]

$AO90$: Induction apparent resistivity with one foot vertical resolution and ninety inches depth of investigation, [Ohm-m]

B : Timur-Coates' porosity constant, [-]

$BVFF_{sd}$: Free bulk volume in the sand layer, [Fraction]

BVI_{sd} : Irreducible bulk volume in the sand layer, [Fraction]

BVI_{sh} : Irreducible bulk volume in the shale layer, [Fraction]

BVI_t : Total irreducible bulk volume, [Fraction]

C : Timur-Coates' irreducible-water-saturation constant, [-]

C_{ca_lmi} : Calcite volumetric concentration obtained with linear mineral inversion, [Fraction]

C_{cg} : Volumetric concentration of coarse grain, [Fraction]

C_{fg} : Volumetric concentration of fine grain, [Fraction]

C_{qz_lmi} : Quartz volumetric concentration obtained with linear mineral inversion, [Fraction]

C_{sh} : Total volumetric concentration of shale, [Fraction]

C_{sh_core} : Shale concentration estimated with XRD measurements, [Fraction]

C_{sh_lmi} : Volumetric shale concentration obtained with linear mineral inversion, [Fraction]

C_{sh_UT} : Shoulder-bed corrected concentration of shale, [Fraction]

C_{shd} : Total dispersed shale concentration in the rock, [Fraction]

$C_{sh\text{-}disp}$: Dispersed shale concentration in the sand layer, [Fraction]

$C_{sh\text{-}gr}$: Shale concentration estimated with gamma ray, [Fraction]

$C_{sh\text{-}lam}$: Laminar shale concentration, [Fraction]

$C_{sh\text{-}lam\_co}$: Laminar shale concentration from core images, [Fraction]

$C_{sh\text{-}lam\_OBMI}$: Laminar shale concentration from OBMI measurements, [Fraction]

$C_{sh\text{-}lam\_Rts}$: Laminar shale concentration from Rt-Scanner measurements, [Fraction]

$C_{sh\text{-}lam\_T\text{-}S}$: Laminar shale concentration from Thomas-Stieber's method, [Fraction]

$C_{sh\text{-}lam\_UT}$: Shoulder-bed corrected laminar shale concentration, [Fraction]

$C_{sh\text{-}n\_d}$: Shale concentration estimated with neutron-density logs, [Fraction]

D : Effective fluid diffusivity coefficient, [cm^2/s]

GR : Total gamma-ray measurement, [GAPI]

GR_{sd} : Gamma-ray activity in clean sand, [GAPI]

GR_{sh} : Gamma-ray activity in pure shale, [GAPI]

GR_{sim} : Numerically simulated gamma ray, [GAPI]

HPT : Hydrocarbon pore thickness, [m]

K_{core} : Core permeability, [mD]

K_h : Horizontal rock permeability, [mD]

K_{sd} : Sand permeability, [mD]

K_{sh} : Shale permeability, [mD]

K_v : Vertical rock permeability, [mD]

m : Archie's porosity exponent, [-]

n : Archie's saturation exponent, [-]

N/G : Net-to-gross ratio, [Fraction]

$NMRBft$: Bound fluid from NMR measurements, [Fraction]

$NMRPhit$: Total porosity from NMR measurements, [Fraction]

$NMRSw_{irr}$: Irreducible water saturation from NMR measurements, [Fraction]

NPL_ls : Neutron porosity in limestone porosity units, [Fraction]

$NPL\_{ls\text{-}sim}$	:	Numerically simulated neutron porosity in limestone porosity units, [Fraction]
P_c	:	Capillary pressure, [Psi]
R_{35}	:	Pore-throat radius at 35% non-wetting phase saturation, [-]
R_{cg}	:	Electrical resistivity of coarse grain, [Ohm-m]
R_{fg}	:	Electrical resistivity of fine grain, [Ohm-m]
R_h	:	Electrical resistivity parallel to bedding plane, [Ohm-m]
Rhob	:	Bulk density, [gm/cc]
$Rhob_{sim}$	:	Numerically simulated bulk density, [gm/cc]
RO90	:	Numerically simulated induction apparent resistivity with one foot vertical resolution and 90 inches depth of investigation, [Ohm-m]
R_{sd}	:	Sand electrical resistivity, [Ohm-m]
R_{sh}	:	Shale electrical resistivity, [Ohm-m]
R_{shh}	:	Horizontal shale resistivity, [Ohm-m]
R_{shv}	:	Vertical shale resistivity, [Ohm-m]
R_{st}	:	Electrical resistivity of low-porosity, high-resistivity streak, [Ohm-m]
R_t	:	True bed resistivity, [Ohm-m]
R_v	:	Electrical resistivity perpendicular to bedding plane, [Ohm-m]
R_w	:	Electrical resistivity of connate water, [Ohm-m]
R_{wb}	:	Bound-water resistivity, [Ohm-m]
R_{xo}	:	Averaged OBMI resistivity curve, [Ohm-m]
Shc_{sd}	:	Hydrocarbon saturation in sand unit, [Fraction]
So	:	Oil saturation, [Fraction]
Sw_b	:	Bound-water saturation, [Fraction]
Sw_f	:	Mobile water saturation, [Fraction]

Sw_{fc} : Total water saturation estimated with electrical anisotropy analysis assuming anisotropic sands, [Fraction]

Sw_{irr} : Total irreducible water saturation, [Fraction]

$Sw_{n\text{-}sh\_con}$: Non-shale water saturation calculated with conventional petrophysical analysis, [Fraction]

$Sw_{n\text{-}sh\_Rts}$: Non-shale water saturation calculated with anisotropy analysis, [Fraction]

Sw_{sd} : Total water saturation in the sand unit, [Fraction]

Sw_{sd_irr} : Irreducible water saturation in the sand unit, [Fraction]

Sw_{sd_Rts} : Sand water saturation calculated with anisotropy analysis, [Fraction]

Sw_{sh} : Shale water saturation, [Fraction]

Sw_{t} : Total water saturation, [Fraction]

Sw_{t_con} : Total water saturation calculated with conventional analysis, [Fraction]

Sw_{t_Rts} : Total water saturation calculated with electrical anisotropy analysis, [Fraction]

Sw_{t_UT} : Shoulder-bed corrected total water saturation, [Fraction]

Sw_{t_UTav} : Shoulder-bed corrected averaged total water saturation, [Fraction]

$T1$: Longitudinal relaxation time, [ms]

$T2$: Transverse relaxation time, [ms]

$T2_{b}$: Transverse bulk relaxation time, [ms]

$T2_{bulk\_gas}$: Transverse bulk relaxation time for gas, [ms]

$T2_{bulk\_oil}$: Transverse bulk relaxation time for oil, [ms]

$T2_{bulk\_wr}$: Transverse bulk relaxation time for water, [ms]

Te : Inter-echo spacing, [ms]

ρ_{ca} : Transverse surface relaxivity of calcite, [μm/s]

ρ_{cl} : Transverse surface relaxivity of clay, [μm/s]

ρ_{qz} : Transverse surface relaxivity of quartz, [μm/s]

ψ : Time decay sequence, [Fraction]

ψ_{av} : Time decay sequence of total bulk volume of the rock, [Fraction]

ψ_{sd} : Time decay sequence for sand layer, [Fraction]

ψ_{sh} : Time decay sequence for shale layer, [Fraction]

Acronyms

AIT	:	Schlumberger Array-Induction Tool
CEC	:	Cation Exchange Capacity
CSF	:	Common Stratigraphic Framework
GAPI	:	American Petroleum Institute Gamma-Ray Units
HI	:	Hydrogen Index
NMR	:	Nuclear Magnetic Resonance
OBM	:	Oil-Base Mud
OBMI	:	Oil-Base Micro Imager
PEF	:	Photo Electric Factor
PPM	:	Parts Per Million equivalent sodium chloride
PU	:	Porosity Unit
RQI	:	Rock Quality Index
RT	:	Rock Type
SEM	:	Scanning Electron Microscope
UTAPWeLS	:	University of Texas at Austin's Petrophysical and Well Log Simulator
XRD	:	X-Ray Diffraction

References

Amaefule, J. O., Altunbay, M., Tiab, D., Kersey, D. G., and Keelan, D. K., 1993, Enhanced reservoir description: Using core and log data to identify hydraulic (flow) unit and predict permeability in uncored intervals/wells, *SPE Annual Technical Conference and Exhibition*, Houston, Texas, USA, October 3-6, Paper SPE 26436.

Bastia, R., Tyagi, A., Saxena, K., Klimentos, T., Altman, R., Alderman, S., and Bahuguna, S., 2007, Evaluation of low-resistivity-pay deepwater turbidite using constrained thin-bed petrophysical analysis, *SPE Annual Technical Conference and Exhibition,* Anaheim, California, USA, November 11-14, Paper SPE 110752.

Cheatwood, C. J., and Guzman, A. E., 2002, Comparison of reservoir properties and development history: Spraberry trend field, West Texas and Chicontepec field, Mexico, *SPE Annual Technical Conference and Exhibition,* Villahermosa, Mexico, February10-12, Paper SPE 74407.

Clavaud, J., Nelson, R., Guru, K. U., and Wang, H., 2005, Field examples of enhanced hydrocarbon estimation in thinly laminated formation with a triaxial array induction tool: a laminated sand-shale analysis with anisotropic shale, *SPWLA 46th Annual Logging Symposium*, New Orleans, Louisiana, USA, June 26-29.

Coates, G. R., Miller, M., Gillen, M., and Henderson, C., 1991, The MRIL in Conoco 33-1: an investigation of new magnetic resonance imaging log, *SPWLA 32nd Annual Logging Symposium,* Midland, Texas, USA, June 16-29.

Estrada, E., Vielma, M., Morales, J., Estrada, J., Tineo, F., and Gomez, G., 2010, Turbidite Chicontepec formation, Channel Chicontepec, Mexico: A diagenetic and petrophysical study to optimize the completions in Corralillo area, *SPE Latin American and Caribbean Petroleum Engineering Conference*, Lima, Peru, December 1-3, Paper SPE 139374.

Fanini, O. N., Kriegshäuser, B. F., Mollison, R. A., Schöen, J. H., and Yu, L., 2001, Enhanced low-resistivity pay, reservoir exploration and delineation with the latest multicomponent induction technology integrated with NMR, nuclear, and borehole image measurements, *Offshore Technology Conference,* Houston, Texas, USA, April 30-May 3.

Hagiwara, T., 1997, "Macroscopic anisotropy" approach to analysis of thinly laminated sand/shale sequences: sensitivity analysis of sand resistivity estimate and environmental corrections, *SPE Annual Technical Conference and Exhibition*, San Antonio, Texas, USA, October 5-8, Paper SPE 38669.

Herrick, D. C., and Kennedy, W. D., 1996, Electrical properties of rocks: effects of secondary porosity, laminations, and thin beds, *SPWLA 37th Annual Logging Symposium,* June 16-19.

Klein, J. D., Martin, P. R., and Allen, D. F., 1995, The petrophysics of electrically anisotropic reservoirs, *SPWLA 36th Annual Logging Symposium*, June 26-29.

Klein, J. D., Martin, P. R., and Allen, D. F., 1997, The petrophysics of electrically anisotropic reservoirs, *The Log Analyst*, May-June, 1997.

Leverett, M. C., 1941, Capillary behavior in porous solids, *Transactions of the AIME*, 142, pp. 159-172.

Méndez de León, J., and Sanguinetti, M., 2006, Flow unit determination through lithofacies identification and its relationship with petrophysical and diagentic properties in early Eocene reservoirs, Chicontepec basin, Mexico, *SPWLA 47th Annual Logging Symposium*, Veracruz, Veracruz, Mexico, June 4-7.

Minh, C. C., and Sundararaman, P., 2011, Nuclear-magnetic resonance petrophysics in thin sand/shale laminations, *SPE Annual Technical Conference and Exhibition*, San Antonio, Texas, USA, Sep 24-27, Paper SPE 102435.

Minh, C. C., Clavaud, J. B., Sundararaman, P., Froment, S., Caroli, E., Billon, O., Davis, G., and Fairbairn, R., 2007, Graphical analysis of laminated and sand-shale formations in the presence of anisotropic shales, *SPWLA 48th Annual Logging Symposium*, Austin, Texas, USA, June 3-6.

Mollison, R. A., Fanini, O. N., Kriegshäuser, B. F., Yu, L., Popta, J., and Ugueto, G., 2001, Impact of multicomponent induction technology on a deepwater turbidite sand hydrocarbon saturation evaluation, *SPWLA 42nd Annual Logging Symposium*, Canton, Ohio, USA, October 17-19.

Ostroff, G. M., Shorey, D. S., and Georgi, D. T., 1999, Integration of NMR and conventional log data for improved petrophysical evaluation of shaly sands, *SPWLA 40th Annual Logging Symposium*, May 30-June 3.

Passey, Q. R., Dahlberg, K. E., Sullivan, K. B., Yin, H., Brackett, R. A., Xiao, Y. H., and Guzmán-Garcia, A. G., 2006, Petrophysical evaluation of hydrocarbon pore-thickness in thinly bedded clastic reservoirs: *AAPG Archie Series*, no.1. Tulsa.

Pittman, E. D., 1992, Relationship of porosity and permeability to various parameters derived from mercury injection-capillary pressure curves for sandstone, *AAPG Bulletin*, v. 76, no. 2, pp. 191-198.

Poupon, A., Loy, M. E., and Tixier, M. P., 1954, A contribution to electrical log interpretation in shaly sands, *Journal of Petroleum Technology*, v. 6, no. 6, pp. 27-34.

Rabinovich, M., Gonfalini, M., Rocque, T., Corley, B., Georgi, D., Tabarovsky, L., and Epov, M., 2007, Multi component induction logging: 10 years after, *SPWLA 48th Annual Logging Symposium*, Austin, Texas, USA, June 3-6.

Sánchez-Ramirez, J. A., Torres-Verdín, C., Wolf, D., Wang, G. L., Mendoza, A., Liu, Z., and Schell, G., 2009, Field examples of the combined petrophysical inversion of

gamma-ray, density, and resistivity logs acquired in thinly bedded clastic rock formations, *SPWLA 50th Annual Logging Symposium*, The Woodlands, Texas, USA, June 21-24.

Schöen, J. H., Mollison, R. A., and Georgi, D. T., 1999, Macroscopic electrical anisotropy of laminated reservoirs: a tensor resistivity saturation model, *SPE Annual Technical Conference*, Houston, Texas, USA, Oct 3-6, Paper SPE 56509.

Shray, F., and Borbas, T., 2001, Evaluation of the laminated formations using nuclear magnetic resonance and resistivity anisotropic measurements, *SPE Eastern Regional Meeting*, Canton, Ohio, USA, Oct 17-19, Paper SPE 72370.

Thomas, E. C., and Stieber, S. J., 1975, The distribution of shale in sandstone and its effects upon porosity, *SPWLA 16th Annual Logging Symposium*, June 4-7.

Timur, A., 1969, Pulsed nuclear magnetic resonance studies of porosity, movable fluid, and permeability of sandstones, *Journal of Petroleum Technology*, v. 21, no. 6, pp. 775-786.

Torres-Verdín, C., 2012, Integrated geological-petrophysical interpretation of well logs, The University of Texas at Austin, January.

Voss, B., Torres-Verdín, C., Gandhi, A., Alabi, G., and Lemkecher, M., 2009, Common Stratigraphic Framework to simulate well logs and to cross-validate static and dynamic petrophysical interpretations, *SPWLA 50th Annual Logging Symposium*, The Woodlands, Texas, USA, June 21-24.